Using organ-on-chip related approaches for immune cell migration research

by

Xiaoou Ren

A thesis submitted to the Faculty of Graduate Studies of

The University of Manitoba

in partial fulfilment of the requirements of the degree of

Doctor of Philosophy

Department of Biosystems Engineering

The University of Manitoba

Winnipeg, Manitoba, Canada

Publication list

This thesis is a grouped manuscript style, and the majority part of this thesis is written based on the following peer-reviewed journal publications.

Journal Publications

1. **Xiaoou Ren**, Anthony E. Getschman, Samuel Hwang, Brian F. Volkman, Thomas Klonisch, David Levin, Min Zhao, Susy Santos, Song Liu, Jasmine Cheng, and Francis Lin. "*Investigations on T cell transmigration in a human skin-on-chip (SoC) model*." ***Lab on a Chip*** **(IF: 6.774)**, **2021**. DOI: 10.1039/d0lc01194k.

2. **Xiaoou Ren**, Abdulaziz Alamri, Jolly Hipolito, Francis Lin, and Sam K.P. Kung. "*Applications of microfluidic devices in advancing NK-cell migration studies*." ***Methods in Enzymology*** **(IF: 1.862)**, **2020**; 631:357-370. DOI: 10.1016/bs.mie.2019.05.052.

3. **Xiaoou Ren**, Jiandong Wu, David Levin, Susy Santos, Ricardo Lobato de Faria, Michael Zhang, and Francis Lin. "*Sputum from chronic obstructive pulmonary disease patients inhibits T cell migration in a microfluidic device*." ***Annals of the New York Academy of Sciences*** **(IF: 5.167)**, **2019**; 1445(1):52-61. DOI: 10.1111/nyas.14029.

4. **Xiaoou Ren**, David Levin, and Francis Lin. "*Cell migration research based on organ-on-chip related approaches*." ***Micromachines*** **(IF: 2.523)**, **2017**; 8(11):324. DOI: 10.3390/mi8110324. **Featured as the cover image**.

Abstract

Immune cell migration plays an essential role in immune surveillance and homeostasis maintenance. Misguided migratory responses of immune cells contribute to various pathological issues. Understanding the mechanisms of immune cell migration is crucial and its investigation requires a suitable approach. Although various methods for cell migration study have been established, most of them lacking configuration of the complex microenvironment *in vitro*, which makes the development of a suitable approach of vital importance. Organ-on-chip (OoC) approach can provide a better platform due to its ability to simulate the key features of certain tissues or organs. In this thesis, we developed different OoC related approaches to study disease-oriented immune cell migration. Specifically, we employed clinical samples in microfluidic device to simulate the microenvironment of chronic obstructive pulmonary disease (COPD), and demonstrated the usage of this approach to quantitatively investigate the complex migratory responses of T cells in COPD. Our results showed an inhibitory effect of the COPD sputum on T cell motility and chemotaxis, which may suggest a possible stopping mechanism to facilitate T cell accumulation in the airway in COPD. We also mimicked the tumor microenvironment in vitro using primary murine natural killer (NK) cells and mouse tumor cell line (i.e., 4T1) in our microfluidic device, and demonstrated it as a proof-of-principle approach to study directional NK cell migration and NK-cancer cell interactions in real-time. Furthermore, we developed a mimicked skin-on-chip (SoC) model that configured the key features of human skin and relevant chemical fields during cutaneous inflammation, and demonstrated its feasibility as a versatile tool for investigating T cell migration and screening potential drugs for targeting chemotactic signaling. Collectively, studies in this thesis bridge organ-specific applications with disease-oriented immune cell migration, and advance our knowledge on the complex roles of immune cell migration in specific disease conditions (i.e., COPD, cancer, skin inflammation), which provide a new conceptual and technological direction for immune cell migration research and contribute to the related research communities.

Acknowledgements

I would like to sincerely thank my supervisor, Dr. Francis Lin, for providing me the great opportunity to join in his wonderful research team. I still remember the first time I met him in the lab, and I was strongly impressed by his great passions on scientific research. I am thankful for his kindness, patience, encouragement, and guidance, especially at the very beginning of my PhD program as I didn't have any background in microfluidics. Dr. Lin is full of new ideas, and always willing to discuss with me whenever I have questions. I learned not only research skills, but also critical thinking of the project under his mentorship.

I also would like to deeply thank my co-supervisor, Dr. David Levin, for his precious advice, guidance, and support during my PhD program. Dr. Levin is optimistic and full of passions on science. He is always supportive in project discussion and manuscript revision during my study.

To my other advisory committees, Dr. Sam Kung and Dr. Song Liu, thank you for all of your valuable advice during my PhD study. I also appreciate the chance you provided me to work with your lab members, and published the joint publications. Great thanks to all the other collaborators during my PhD study for their contribution on reagents, materials and research discussion.

Many thanks to Dr. Jiandong Wu, for teaching me all the relevant lab techniques at the beginning of my study. All the discussions with Jiandong help me a lot. Thank Jolly Hipolito for his great job in maintaining the lab during the first two years of my study. Thank Ziba Rovei Miab, for ordering all the lab reagents and supplies for us. To all the other team members who have ever worked with me in the Immunotrafficking Lab, your great support is appreciated.

Thanks to the Nano-Systems Fabrication Laboratory (NSFL) at the University of Manitoba, for providing the training and facility for device fabrication. I also want to thank the Seven Oaks General Hospital and Victoria General Hospital in Winnipeg for managing clinical samples during my study. Great thanks to the financial support by the Discovery Grant from the Natural Sciences and Engineering Research Council of Canada (NSERC) to Dr. Francis Lin, and the Graduate Enhancement of Tri-Council Stipends (GETS) program at the University

of Manitoba to me. Many thanks to the priceless support from Department of Biosystems Engineering and Department of Physics and Astronomy during my PhD study.

Finally, I want to give my deeply thank and love to my parents and wife. Thank you for the confidence in me even during the hardest time. Thank my parents for their unlimited love, and the support to all my decisions. Thank my wife for the lovely accompanying with me every day. I hope this thesis dedicated as a gift to all the family members and friends who care about me.

Table of contents

List of tables

List of figures

List of abbreviations

2D	two dimensional
3D	three dimensional
ACC	adenoid cystic carcinoma
aHPBTs	activated human peripheral blood T cells
APC	antigen presenting cell
BBB	blood-brain barrier
BM	bone marrow
BME	basement membrane extract
BoC	brain-on-chip
CAF-µTP	cancer-activated fibroblast microtissues
CCL	C-C motif ligand
CCR	C-C motif chemokine receptor
Cdc42	cell division cycle 42
CNS	central nervous system
COPD	chronic obstructive pulmonary disease
CX3CR	C-X3-C motif chemokine receptor
CXCL	C-X-C motif ligand
CXCR	C-X-C motif chemokine receptor
DC	dendritic cell
DIC	differential interference contrast
DRG	dorsal root ganglion
DTT	dithiothreitol
EC	endothelial cell
ECM	extracellular matrices
FB	Fibroblast
FBS	fetal bovine serum
FGF-2	fibroblast growth factor 2
fMLP	*N*-formyl-methionyl-leucyl-phenylalanine
FN	Fibronectin
GPCRs	G protein-coupled receptors
hBMECs	human brain microvascular endothelial cells

HCC	hepatocellular carcinoma
HEV	high endothelial venule
hNPC	human fetal neural progenitor cell
hNSC	human neural stem cell
HSCs	hematopoietic stem cells
HUVEC	human umbilical vein endothelial cell
ICAM-1	intercellular adhesion molecule 1
iDC	immature DC
IL-2	interleukin-2
IL-7	interleukin-7
IL-8	interleukin-8
IL-15	interleukin-15
LFA-1	lymphocyte function-associated antigen 1
LN	lymph node
LPS	Lipopolysaccharide
LTB4	leukotriene B4
mDC	mature DC
MGE	medial ganglionic eminence
NF-µTP	normal fibroblast microtissues
NK	natural killer
OoC	organ-on-chip
NPC	neural progenitor cell
PBMCs	peripheral blood mononuclear cells
PBS	phosphate buffer saline
PDMS	polydimethylsiloxane
pMHC	peptide-major histocompatibility complex
PNI	perineural invasion
Rac1	Rac family small GTPase 1
RhoA	Ras homolog family member A
Rho GTPases	Ras homologous guanosine triphosphate enzymes
SDF-1α	stromal cell-derived factor-1 alpha
SLTs	secondary lymphoid tissues
SoC	skin-on-chip

TCR	T cell receptor
TCZ	T cell zone
TEI	transendothelial invasion
TEM	transendothelial migration
TNF-α	tumor necrosis factor alpha
TVM	transvascular migration
µTP	microtissues
µVNs	microvascular networks

Permission of using published materials

- **Figure 1.1D** is adapted from reference "*Lab on a Chip* **2012**, *12*, 3861-3865" with permission from the Royal Society of Chemistry.
- **Figure 1.2A** is adapted from reference "*Proceedings of the National Academy of Sciences* **2012**, *109*, 13515-13520" with permission from the National Academy of Sciences.
- **Figure 1.2B** is adapted from reference **"***Lab on a Chip* **2015**, *15*, 3222-3231" with permission from the Royal Society of Chemistry.
- **Figure 1.2C** is adapted from reference "*Advanced healthcare materials* **2016**, *5*, 3074-3084" with permission from John Wiley and Sons.
- **Figure 1.2D** is adapted from reference "*Integrative Biology* **2016**, *8*, 359-367" with permission from the Royal Society of Chemistry.
- **Figure 1.3A** is adapted from reference "*PloS one* **2015**, *10*, e0126523" with permission from PLOS.
- **Figure 1.3B** is reproduced from reference "*Proceedings of the National Academy of Sciences of the United States of America* **2014**, *111*, 5813-5818" with permission from the National Academy of Sciences.
- **Figure 1.4A** is adapted from reference "*Lab on a Chip* **2012**, *12*, 3861-3865" with permission from the Royal Society of Chemistry.
- **Figure 1.4B** is adapted from reference "*Lab on a chip* **2012**, *12*, 2837-2842" with permission from the Royal Society of Chemistry.
- **Figure 1.4C** is adapted from reference "*Nature protocols* **2017**, *12*, 865" with permission from Nature Publishing Group.
- **Figure 1.5A** is adapted from reference "*Lab on a Chip* **2016**, *16*, 3728-3740" with permission from the Royal Society of Chemistry.

- **Figure 1.5B** is adapted from reference "*RSC Advances* **2013**, *3*, 16002-16010" with permission from the Royal Society of Chemistry.
- **Figure 1.5C** is adapted from reference "*Proceedings of the National Academy of Sciences of the United States of America* **2011**, *108*, 5614-5619" with permission from the National Academy of Sciences.
- **Figure 1.5D** is adapted from reference "*PloS one* **2011**, *6*, e18183" with permission from PLOS.
- **Figure 1.6A** is adapted from reference "*Lab on a Chip* **2016**, *16*, 4152-4162" with permission from the Royal Society of Chemistry.
- **Figure 1.6B** is adapted from reference "*Journal of neuroscience methods* **2015**, *0*, 80-84" with permission from Elsevier.
- **Figure 1.6C** is adapted from reference "*Scientific Reports* **2016**, *6*, 36670" with permission from Nature Publishing Group.
- **Chapter 1** with the exception of **section 1.1 and 1.2** is reproduced from my publication "**Xiaoou Ren**, David Levin, and Francis Lin. *Cell migration research based on organ-on-chip-related approaches*. ***Micromachines* (IF: 2.523)**, **2017**; 8(11):324." Open Access. Permission request is not needed.
- **Chapter 2** is reproduced from my publication "**Xiaoou Ren**, Jiandong Wu, David Levin, Susy Santos, Ricardo Lobato de Faria, Michael Zhang, and Francis Lin. *Sputum from chronic obstructive pulmonary disease patients inhibits T cell migration in a microfluidic device*. ***Annals of the New York Academy of Sciences* (IF: 5.167)**, **2019**; 1445(1):52-61." with permission from John Wiley and Sons.
- **Chapter 3** is reproduced from my publication "**Xiaoou Ren**, Abdulaziz Alamri, Jolly Hipolito, Francis Lin, and Sam K.P. Kung. *Applications of microfluidic devices in advancing NK-cell migration studies*. ***Methods in Enzymology* (IF: 1.862)**, **2020**; 631:357-370." with permission from Elsevier.

- **Chapter 4** is reproduced from my publication "**Xiaoou Ren**, Anthony E. Getschman, Samuel Hwang, Brian F. Volkman, Thomas Klonisch, David Levin, Min Zhao, Susy Santos, Song Liu, Jasmine Cheng, and Francis Lin. *Investigations on T cell transmigration in a human skin-on-chip (SoC) model*. ***Lab on a Chip*** **(IF: 6.774)**, **2021**. DOI: 10.1039/d0lc01194k. Permission request is not needed according to the reusing policy of Royal Society of Chemistry.

- **6.4 General limitations of OoC approach to overcome in the future** is written based on my publication "**Xiaoou Ren**, David Levin, Francis Lin. *Cell migration research based on organ-on-chip-related approaches*. ***Micromachines*** **(IF: 2.523)**, **2017**; 8(11):324." Open Access. Permission request is not needed.

Chapter 1: Literature review

It's worth pointing out that the majority part of this chapter except **section 1.1 and 1.2**, is written based on my publication: "**Xiaoou Ren**, David Levin, and Francis Lin. *Cell migration research based on organ-on-chip-related approaches*. ***Micromachines*** **(IF: 2.523)**, **2017**; 8(11):324."

Chapter 1 provides literature review on cell migration, chemotaxis, immune cell development and trafficking, and the importance of immune cell migration for homeostasis. It also includes different methods for cell migration study in this chapter, among them, organ-on-chip (OoC) approach provides a better platform due to its ability of mimicking the microenvironment of a physiological organ based on microfluidic chip. Indeed, different types of OoC related approaches for cell migration studies have been rapidly developed, thus, this chapter also comprehensively introduces these studies.

1.1 Overview of cell migration and chemotaxis

1.1.1 Cell migration

Cell migration is a broad definition that refers to the movement of cells from one location to another. The physical structure of cells is supported and organized by dynamic functions of the cytoskeleton. Dynamic remodeling of this structure enables cell movements in diverse biological contexts, such as cell-cell migratory interaction, wound healing and transmigration across tissue barriers [1]. Briefly, cell migration can be classified into two different types according to the microenvironment wherein the migration happens, including cell migration on a two dimensional (2D) substrate or through a three dimensional (3D) tissue barrier [2-5]. For example, the process of a single cell migrating over a 2D substrate can be dissected into multiple steps, including protrusion, adhesion, contraction, rear detachment, and recycling of all the steps [2,3]. The migration process of cells such as T cells through a 3D endothelium barrier that is also called transmigration, can be divided into multiple steps, including tethering, rolling, activation, firm adhesion, and then transmigration [4,5]. Depending on the activation state, T cell transmigration can be either achieved by going across the endothelial cell body

through transcellular route, or squeezing across the junction between two endothelial cells via the paracellular route [4].

1.1.2 Chemotaxis

Directional cell migration to soluble concentrated chemical gradient is chemotaxis [6]. Recognition of specific chemical cues such as chemoattractants, typically involves coordinated regulation by the tissue-specific adhesion molecules and chemoattractants that interact with their counter-receptors on the migrating cells, followed by further processing relevant downstream signaling pathways [7-9]. For example, T cells can continuously scan the local microenvironment in an inherent manner for recognizing specific antigens expressed on the cell surface of antigen-presenting cells (APCs) [4]. Upon physical contact with APCs, the motility of T cells tunes from a go behavior to a pausing phase for activating some dominant receptors, such as chemokine receptors, T cell receptor (TCR) and integrins (e.g., lymphocyte function-associated antigen 1 (LFA-1)), resulting in cytoskeleton remodeling of T cells for migration [4]. Briefly, triggering these receptors leads to the activation of the Ras homologous guanosine triphosphate enzymes (Rho GTPases), including Rac family small GTPase 1 (Rac1), Ras homolog family member A (RhoA), and cell division cycle 42 (Cdc42). Cdc42 and Rac1 can activate actin related protein 2/3 (Arp2/3) complex via Wiskott-Aldrich syndrome protein (WASP) and WASP-family verprolin homologous protein (WAVE) complexes, respectively. Arp2/3 complex mediates actin polymerization at the leading edge to form branched actin network, and make cell move forward. RhoA plays a dual role by promoting actin filament elongation via diaphanous-related formin 1 (mDia1) at the leading edge and facilitating myosin contraction at the rear edge by activating Rho kinase (ROCK), resulting in the directional migration of T cells. [4].

1.2 Immune cell trafficking in tissues

1.2.1 Overview of immune cell development

Immune cell trafficking plays a crucial role for the distribution, development and maturation of lymphocyte progenitors and immature immune cells in the proper tissues or

organs. This process is mediated by cooperated functions of the locally released adhesion molecules or chemoattractants with their corresponding homing receptors expressed on the surface of target immune cells [10].

Neutrophils belong to the innate immune system, can rapidly response to inflammatory activities that occur in the human body [11]. Neutrophils are produced from bone marrow (BM) in a large number at immature stage. The maturation and migration of neutrophils is regulated by C-X-C motif chemokine receptor 4 (CXCR4) / SDF-1α axis. Specifically, the retention of immature neutrophils in the BM is mediated by high expression of SDF-1α secreted from BM stromal cells. Upon maturation, the expression of SDF-1α by BM stromal cells is down-regulated, which enables the migration of neutrophils from bone marrow to peripheral blood circulation to direct their immune surveillance [12].

Dendritic cells (DCs) are derived from BM progenitors, and these cells are extensively accepted as the most competent APCs [35]. The unique ability of DCs ensures the capture of foreign antigens to induce innate immune response, and transfers the information to the SLTs to initiate the adaptive immune response. Immature DCs normally reside in the peripheral tissues and express multiple chemokine receptors, including C-C motif chemokine receptor 1 (CCR1), CCR2, CCR5, CCR6, CXCR3 and CXCR4, to direct their migration to the inflammatory sites through corresponding signaling pathways. Upon stimulation of specific chemokines, cytokines, or foreign antigens, immature DCs become mature and migrate to SLTs through upregulated CCR7-CCL19/21 axis for triggering DC-T cell interaction [13,14].

Natural killer (NK) cells belong to the innate immunity are derived from BM hematopoietic stem cells (HSCs). Although the percentage of NK cells in lymphocytes is low (1-10%), the cytotoxic killing of NK cells towards abnormal cells (e.g., cancer and virus-infected cells) is crucial for the innate system. NK cells can express various chemokine receptors, such as CCR2, CCR5, CCR7, CXCR1, CXCR3, CXCR4, CXCR6, and C-X3-C motif chemokine receptor 1 (CX3CR1), and these receptors mediate the development and distribution of NK cells in the body. For example, immature NK cells normally localize in bone marrow and lymph nodes (LNs), wherein NK cells highly express CXCR4 and CCR7, respectively, for their local retention. While mature NK cells predominate in the blood, liver,

spleen, and lung, which highly express CXCR1 and CX3CR1. Although NK cells can directly response to abnormal cues, the interaction of NK cells with activated DCs is suggested to help fully activate NK cell function, which is similar to DC-T cell interaction [15,16].

B cells belong to the adaptive immunity are professional APCs that derived from HSCs originated from BM [17,18]. During the early stage of B lymphopoiesis, SDF-1α plays a great role in localizing pre-proB cells within the bone marrow microenvironment. Pre-proB cells become more mature when interact with BM stromal cells that highly express interleukin-7 (IL-7), and this interaction facilitates the exit of immature B cells from BM [18]. The migration of immature B cells to the SLTs is regulated by high endothelial venules (HEVs) through CCR7-CCL19/21 axis. Continuous expression of C-X-C motif chemokine ligand 13 (CXCL13) by stromal cells in the LN follicles mediates B cells to the sites and forms B cell zone [19]. B cell receptors are activated upon specific antigen stimulation that trigger the relevant downstream signaling pathways, and then immature B cells become mature to play their immune surveillance and leave the SLTs [17].

T cells belong to adaptive immunity that originated from BM HSCs [18,19]. HSCs are retained in BM due to their direct interaction with BM stromal cells. Specifically, the high concentration of SDF-1α secreted by BM stromal cells mediates the retention of HSCs in BM to form niches. Stem cell factor is another important cytokine that released in BM, coordinating with the downregulation of SDF-1α to facilitate the migration of HSCs from BM to the bloodstream [20]. Migrating HSCs to the thymus from bloodstream is mediated by upregulation of CCR9-CCL25 axis, followed by its downregulation upon HSCs entering thymus, to promote the differentiation and proliferation of thymocytes [18,20]. Thymocytes become naïve T cells that egress from thymus and migrate to the SLTs through upregulation of CCR7-CCL19/21 axis [19,20]. Naïve T cells migrate randomly for scanning antigens in the T cell zone, and become activated upon their physical contact with APCs [19,21]. Activated T cells residue in the SLTs for proliferation and expansion, while non-activated T cells immediately egress from SLTs to the surrounding tissues [22].

1.2.2 Immune cell migration for homeostasis and related pathogenesis

Finely controlled immune cell migration in human body not only facilitates development and distribution of different immune cells, but also ensures specific immune response for homeostasis. Immune cell trafficking in different tissues is regulated by specific environmental cues (e.g., chemoattractants) and their corresponding receptors expressed by immune cells. These relevant chemokine receptors are also called G protein-coupled receptors (GPCRs). In contrast to the direct and rapid response of innate immunity to inflammatory cues, adaptive immunity are less responsive to these cues. Upon activation by cell-cell interaction such as DC-T cell interaction in the SLTs, adaptive immune cells are fully fired up for the immune surveillance [23].

On the other hand, misguided immune cell migration can cause multiple pathological problems. For example, neutrophils are the most abundant immune cells that migrate to the inflammatory sites fighting for bacteria or fungus, while the cytotoxic mediators released by activated neutrophils also can damage tissues [23]. Similarly, although T cell migration is important for adaptive immune defense, the cytolytic activities and proinflammatory mediator secretions can cause tissue injury [24]. Detailed studies showed that chronic obstructive pulmonary disease (COPD) is correlated with abnormal immune cell trafficking, and the accumulations of different immune cells in the airway facilitate the disease development [25-32]. In addition, other inflammatory diseases such as myocardial infarction, stroke, atherosclerosis, multiple sclerosis, rheumatoid arthritis, psoriasis, Crohn disease, type I diabetes, allograft rejection, hepatitis, lupus, asthma, and atopic dermatitis, have been demonstrated that associated with misguided immune cell trafficking [23].

1.3 Different approaches for cell migration studies

1.3.1 *In-vivo* animal models

Cell migration research requires the ability to configure and control complex cellular microenvironments. *In-vivo* animal models, such as homing assays or intravital imaging methods, directly provide the tissue microenvironment (**Figure 1.1A-B**), and those approaches

have been widely used for cell trafficking studies. However, those approaches are expensive, involve complicated procedures and require sacrificing animals [33]. Reduction and/or replacement of animal-based research is a high priority for both the research community and the public [34]. In addition, cell migration environments are poorly defined in animal experiments and observation of cell migration *in vivo* is greatly limited by the current state-of-the-art imaging capability. Ultimately, the applicability of results generated by animal studies for human healthcare applications is limited by significant variations between humans and experimental animals [35,36].

1.3.2 Traditional *in-vitro* assays

Traditional *in-vitro* cell migration assays, such as transwell assays [37] and other real-time visualization chambers, are another broadly used research approach to study cell migration (**Figure 1.1C**). Compared with animal studies, *in-vitro* cell migration assays are more cost-effective, easier to operate, and can directly test human cells. Nevertheless, although cell migration conditions are better defined in these assays, they are lacking the ability to precisely control the cell migration environment in space and time, and the conditions configured in these assays are over-simplified compared with the *in-vivo* situation.

1.3.3 Microfluidic devices

Microfluidic devices were rapidly developed over the last two decades and these devices have been increasingly used for cell migration research (**Figure 1.1C**) [38,39]. Microfluidic devices offer significant advantages in device miniaturization, precise configuration and flexible manipulation of cellular microenvironments such as stable chemical gradient generation, low reagent consumption, real-time observation of cell migration at the single-cell level and high-throughput experimentation [40-43]. On the other hand, the majority of the current microfluidic cell migration devices are only capable of producing much-simplified chemical fields and extracellular matrices (ECM) compared with tissue environments. Many of these devices focus on single cell types and ECM conditions, and thus do not capture the complex properties of tissues and organs *in vivo*. Additionally, although cell migration has high disease relevance and microfluidic devices have the potential to enable disease-oriented cell

migration studies, very few microfluidic cell migration studies to date have involved testing clinical samples from patients to investigate the disease mechanism or for diagnostic assessment [6,44].

1.3.4 Organ-on-chip (OoC) approaches

Therefore, there has been a growing trend to develop new microfluidic devices to better reconstitute the complex *in-vivo* microenvironment at the tissue or organ level, which is commonly referred to as "organ-on-chip" (**Figure 1.1D**) [45-47]. Generally speaking, the construction of OoC systems is based on microfluidic cell-culture devices, which simulate the key activities and responses of certain tissues or organs. This approach integrates microfluidics technology with tissue engineering, permitting investigation of organ-specific physiological mechanisms and diseases. For example, some studies successfully established "liver-on-chip" and "kidney-on-chip" systems for studying hepatic or renal functions, respectively [48-50]. Similarly, a recent study constructed a biomimetic "skin-on-a-chip" model for drug toxicity testing and disease study [51]. Thus, OoC offers a novel and advanced research approach for cell migration study.

1.4 Different types of organ-on-chip (OoC) for cell migration studies

Indeed, in this direction, we observed growing development of cell migration studies involving OoC related approaches. In this section, these studies are broadly defined that meet one or more of the following criteria: 1) cell migration and interaction studies that involve reconstituting the physiological structures of specific organs using multi-cell co-culture in 3D microfluidic models; 2) cell migration studies in microfluidic devices that configure complex chemical fields relevant to target organs; and 3) cell migration studies that test clinical cell or/and tissue samples for diagnostic assessment of organ-specific diseases. Under these selection criteria, the rest of this section is organized to review organ-specific cell migration studies using OoC related approaches including "tumor-on-chip", "lung-on-chip", "vessel-on-chip", "LN-on-chip", and "brain-on-chip" (**Table 1.1**).

Figure 1. 1 A schematic illustration of different cell migration research approaches to study this important and complicated process in humans.

(**A**) Schematic presentation of human body and transendothelial migration of immune cells. (**B**) Schematic presentation of *in-vivo* animal models. (**C**) Schematic presentation of *in-vitro* cell migration assays. (**D**) An example of the OoC approach. BM: basement membrane; EC: endothelial cell; ECM: extracellular matrices. **Figure 1.1D** is adapted from reference [52] with permission from the Royal Society of Chemistry.

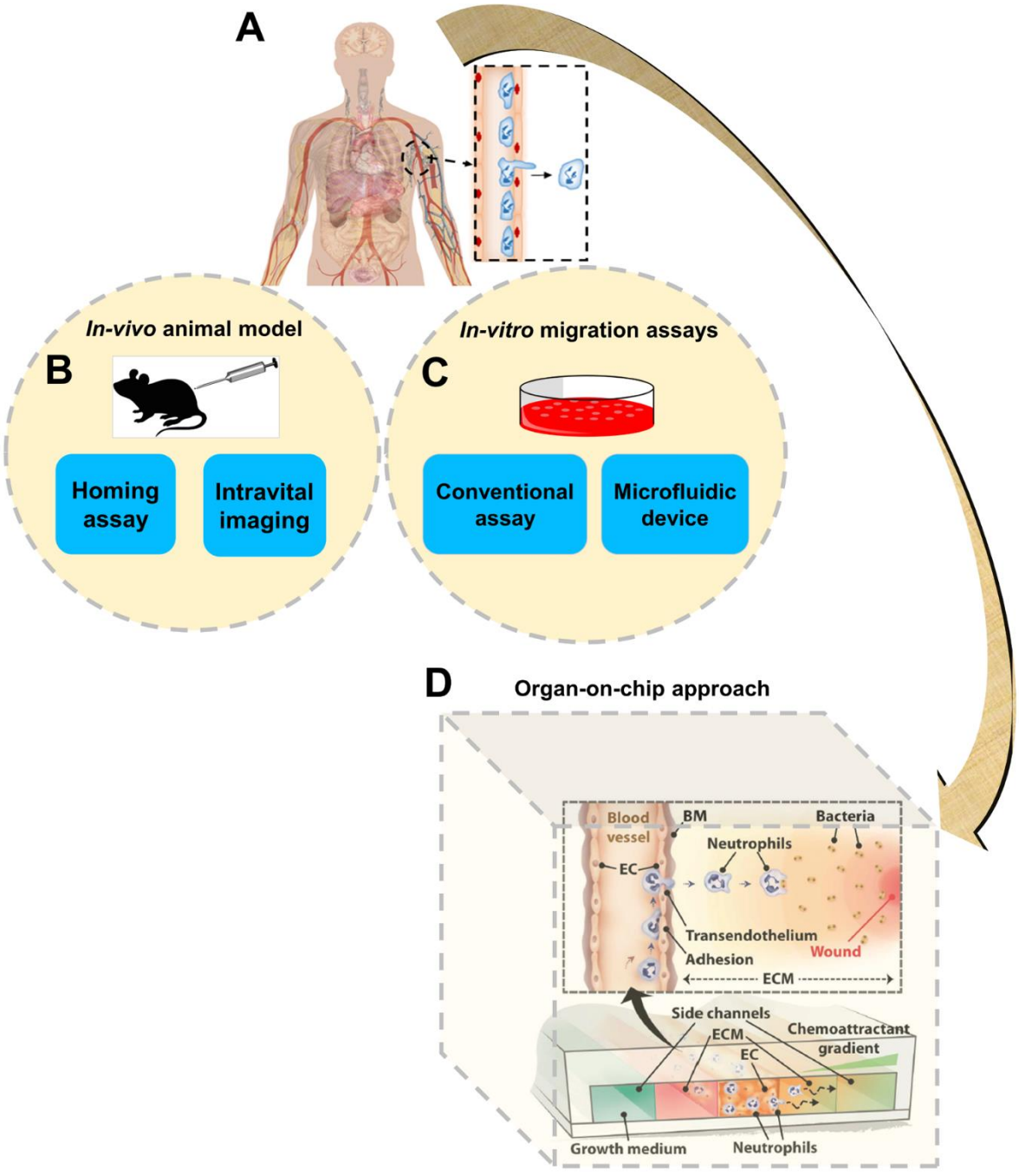

Table 1. 1 Summary of cell migration studies using organ-on-chip-related approaches.

Organ Type	Comments	Ref.
Tumor-on-chip	Investigating endothelial barrier function during tumor cell intravasation;	[53]
	Investigating immune surveillance of natural killer (NK) cells for tumors;	[54]
	Investigating ECM activation during tumor progression;	[55]
	Investigating the interactions between neurons and cancer cells during tumor perineural invasion.	[56]
Lung-on-chip	Investigating bacteria or inflammatory cytokine induced cell migration;	[57]
	Investigating neutrophil chemotaxis with clinical samples for diagnosis of chronic obstructive pulmonary disease (COPD);	[6]
	Rapid analysis of neutrophil chemotaxis;	[58]
	Investigating neutrophil chemotaxis with clinical samples for asthma detection.	[44]
Vessel-on-chip	Investigating neutrophil transendothelial migration (TEM) during inflammatory process;	[52]
	Investigating tumor transendothelial invasion (TEI);	[59]
	Investigating tumor cell extravasation;	[60]
	Investigating angiogenesis.	[61]
Lymph node-on-chip	Investigating the interaction between T cells and dendritic cells (DCs);	[62]
	Evaluating DC chemotaxis and DC–T cell interaction;	[63]
	Investigating differential chemotaxis of DCs to CCL21 and CCL19;	[64]
	Studying the guidance of CCR7 ligands for T cell migration in Lymph Nodes (LNs);	[21]
	Investigating differential chemotaxis of DCs through CCR7 and CXCR4 signaling.	[14]
Brain-on-chip	Investigating neuronal differentiation and chemotaxis;	[65]
	Investigating neuronal migration;	[66]
	Investigating human neural stem cell (hNSC) neurogenesis;	[67]
	Investigating brain tumor metastasis.	[68]

1.4.1 Tumor-on-chip

Cancer cell migration is a critical process during cancer progression and metastasis. During metastasis, tumor cells migrate from their initial locations to distant organs, leading to new tumor formation [69-71]. Cell-cell interaction and chemotaxis are two important biological processes that are involved in tumor metastasis [72,73]. However, the mechanism of tumor metastasis is far from being well-understood, in part hindered by the limitations of current cell migration research methods in controlling the complex physiological tumor microenvironments [74]. OoC offers a promising new approach to tumor cell migration studies. Here we highlight some examples in this direction (**Figure 1.2**; **Table 1.1**).

As one example, Kamm and coworkers developed a three-dimensional (3D) microfluidic model for investigating endothelial barrier function during tumor cell intravasation (**Figure 1.2A**) [53]. The device consists of two side microchannels for seeding of the tumor and endothelial cells (ECs), respectively, and these two channels were connected via a middle channel that was filled with 3D hydrogel. An endothelial monolayer was formed at all the 3D ECM-endothelial interface regions and enabled the observation of transmigrating tumor cells across the vascular lumen in real time. By using this tumor-on-chip approach, the 3D physiological tumor-vascular interface was reconstituted *in vitro*. These results demonstrated that cellular interaction with macrophages or stimulation with tumor necrosis factor alpha (TNF-α) increased endothelial permeability, resulting in endothelial barrier impairment and a higher tumor cell intravasation rate. In another recent study, this device was used to study anti-tumor efficacy of engineered TCR-T cells [75]. This system enabled the observation and analysis of specific T cell immune surveillance, including T cell directional migration to tumors and their subsequent tumor-killing function on the chip.

As another example, Wiklund and coworkers established an ultrasonics-based 3D microdevice for studying immune surveillance of NK cells for specific tumors (**Figure 1.2B**) [54]. Briefly, this device was comprised of a multi-well microplate and a ring-shaped ultrasonic transducer. The microplate was made of a silicon wafer with arrayed (10 × 10) wells in the center, which was bonded onto a glass slide. This multi-well microplate was surrounded by a

polydimethylsiloxane (PDMS) frame bonded to the top layer, providing a pool for cell medium injection. A cover slip was placed onto the PDMS frame in order to minimize evaporation. The ultrasonic transducer consisted of a ring-shaped piezoceramic plate and an open central hole for visualization under a microscope. By using controlled ultrasonic waves produced by the transducer under well-regulated environmental conditions, biomimetic 3D tumors composed of human hepatocellular carcinoma (HCC) HepG2 cells were achieved simultaneously in each well of the microplate. This approach enabled the observation of NK cell migration and the interactions between NK cells with 3D solid tumors. In addition, the number of NK cells required for preventing tumor growth in the first day, or destroying a tumor in the following days, was determined using this system.

In another study, Imparato and coworkers developed a breast-cancer-on-chip model to investigate ECM activation during tumor progression (**Figure 1.2C**) [55]. This model consisted of two main components: (1) a syringe pump for continuous medium perfusion and metabolic waste removal at controlled flow rate; and (2) a microfluidic chip for mimicking the breast tumor microenvironment. Briefly, the chip had one main chamber and three connected channels. The main chamber was divided into a big stromal compartment and a small tumor compartment, respectively. Both compartments were loaded with 3D microtissues (μTP). Normal fibroblast microtissues (NF-μTP) or cancer-activated fibroblast microtissues (CAF-μTP) were injected into the stromal compartment, while malignant epithelial breast cancer cell microtissues (MCF7-μTP) were injected into the tumor compartment. Based on this tumor-on-chip approach, a 3D engineered tumor microenvironment was established. This system enabled monitoring and analysis of tumor–stromal interactions and tumor-ECM communications during tumor invasion toward the adjacent stromal compartment in real time. These results demonstrated that 3D fibroblast μTP can promote tumor cell invasion resulting from increased secretion of paracrine molecules in a 3D environment compared to a 2D environment.

Finally, Jiang and coworkers developed a tumor-on-chip model to investigate the interactions between neurons and cancer cells during tumor perineural invasion (PNI) (**Figure 1.2D**) [56]. The microfluidic chip consisted of two cell-culture channels that were interconnected by parallel arrayed microgrooves, bonded onto a culture dish. The left channel

and the right channel were used for loading neurons and cancer cells, respectively. Primary hippocampal and cortical neurons from embryonic Sprague-Dawley (SD) rats and dorsal root ganglion (DRG) neurons from postnatal SD rats were used in the study. These neurons were mixed and cultured in the device. In addition, three different human cancer cell lines, including a prostate cancer cell line (PC-3), a pancreatic cancer cell line (Panc-1) and a breast cancer cell line (MCF-7), were selected according to their different levels of tumor PNI [76]. Co-culture of these physiologically relevant cells in the microfluidic chip mimicked the pathological microenvironment during cancer PNI. These results demonstrated that neurites facilitated cancer cell attachment and induced their directional migration. Moreover, cancer cells with high PNI levels (PC-3 and Panc-1) exhibited stronger migratory behavior along neurites than cancer cells with low PNI levels (MCF-7). Thus, interruption of neurites and blockade of the neuron-cancer interaction has the potential to inhibit cancer cell migration.

Figure 1. 2 Examples of tumor-on-chip cell migration study.

(**A**) The 3D microfluidic model for investigating endothelial barrier function during tumor cell intravasation. The left panel shows the microfluidic device (green: endothelial cell channel; red: tumor channel; dark gray: 3D ECM channel; black arrow: Y junction); the upper-right panel shows a representative phase-contrast image of tumor cell (red) invasion through 3D ECM region (dark gray) to the endothelium (green); the bottom-right panel shows a 3D confocal image of the selective area in the white-dashed square (red: tumor cells; green: endothelium). (**B**) The ultrasonics-based 3D microdevice for studying immune surveillance of NK cells for specific tumors. The left panel illustrates the main components of the microfluidic system; the right panel shows some representative experimental images of NK-tumor interaction at different time points (orange: NK cells; green: solid tumors). (**C**) The breast-cancer-on-chip model to investigate ECM activation during tumor progression. The figure shows the microfluidic system and magnified view of the chip (green: stromal microtissues; red: tumor microtissues; blue arrow: fluid flow direction; white arrow: 3D microtissue injection direction). (**D**) The tumor-on-chip model to investigate the interactions between neurons and cancer cells during tumor PNI. The upper panel illustrates the microfluidic device; the bottom panel shows a representative image of tumor cell (red) migration behavior along the contacted neurites at different time points. **Figure 1.2A** is adapted from reference [53] with permission from the National Academy of Sciences; **Figure 1.2B** is adapted from reference [54] with permission from the Royal Society of Chemistry; **Figure 1.2C** is adapted from reference [55] with permission from John Wiley and Sons; **Figure 1.2D** is adapted from reference [56] with permission from the Royal Society of Chemistry.

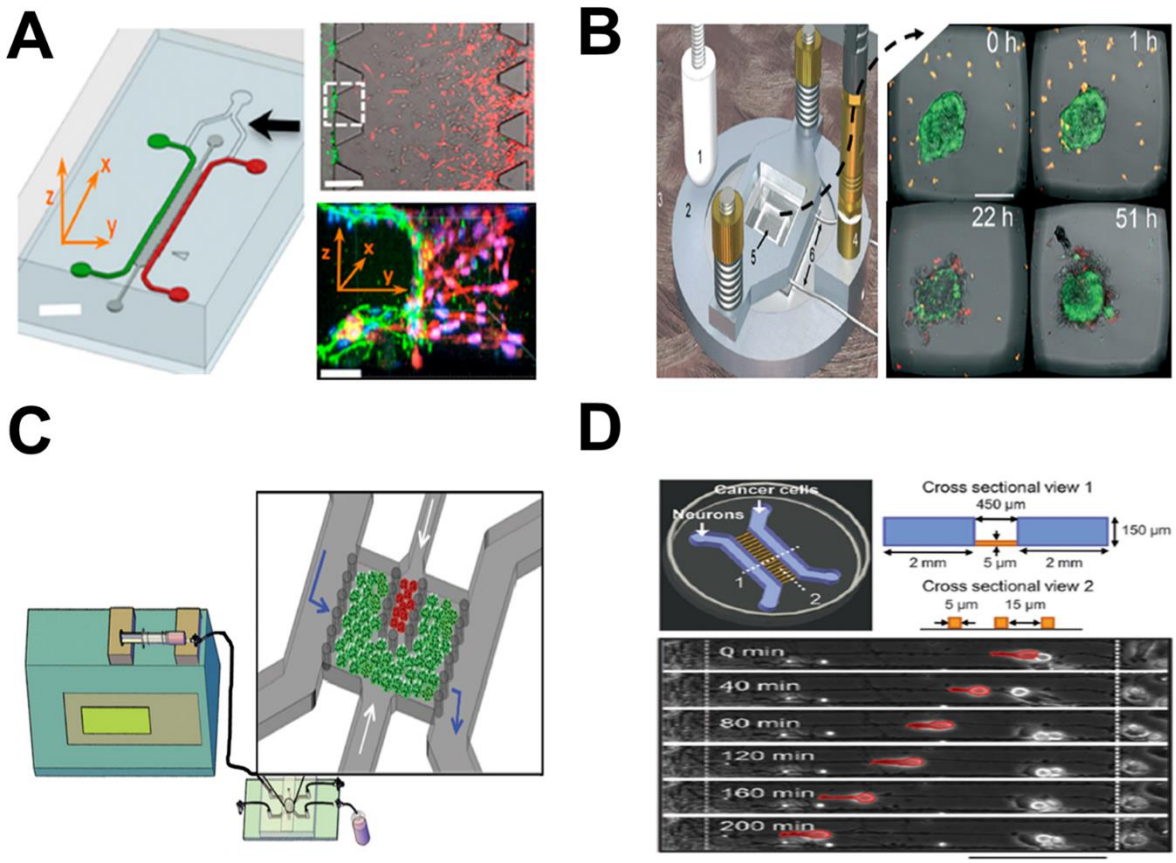
A
B
C
D
0 h
1 h
22 h
51 h
Cancer cells
Neurons
Cross sectional view 1
450 µm
150 µm
2 mm
5 µm
2 mm
Cross sectional view 2
5 µm
15 µm
0 min
40 min
80 min
120 min
160 min
200 min

1.4.2 Lung-on-chip

Neutrophils are the largest population among white blood cells, and their migration plays important roles in the human immune system [77]. Disordered neutrophil migration and recruitment can result in pulmonary inflammation and associated lung diseases, such as asthma and chronic obstructive pulmonary disease (COPD) [78,79]. OoC technologies provide a useful approach to study cell migration in the mimicked lung microenvironment. In addition, testing cell migration using clinical samples from patients with lung diseases offers useful cell functional diagnostic assays. Here we review some examples of OoC cell migration studies related to either mimicking the lung microenvironment or pulmonary disease diagnosis (**Figure 1.3**; **Table 1.1**).

Ingber and coworkers engineered a biomimetic lung-on-chip microsystem, which replicated the alveolar–capillary structures of human lung, for investigating bacteria or inflammatory cytokine-induced cell migration. The microfluidic device consisted of two side chambers, and one main channel with two compartments separated by a porous ECM-coated PDMS membrane [57]. The upper compartment was an air-filled channel, which was used for seeding lung alveolar epithelial cells. The lower compartment was a microvascular channel, which was used for lining lung microvascular ECs. The mimicked human breathing activities were achieved by applying mechanical strain rhythmically from the side chambers. The integration of rhythmical mechanical stretching in the side chambers, cyclic air–liquid interflow within the membrane and regulated fluid flow in the microvascular channel enabled the patterning of epithelial cells and ECs onto the membrane for differentiation. This "breathing" lung-on-chip model enabled the investigation of lung-specific immune response to bacteria- or cytokine-induced inflammatory processes. In order to mimic pulmonary inflammation, TNF-α and Escherichia coli (*E. coli)* bacteria were injected into the alveolar epithelial cell layer, which rapidly activated ECs and increased the surface expression of intercellular adhesion molecule 1 (ICAM-1) in the microvascular channel. The results showed that this effect induced neutrophil recruitment to ECs, and stimulated their directional transmigration across the tissue barrier for immune surveillance. This system demonstrated a low-cost on-chip model for cell

migration study and provided an alternative option to animal models for drug delivery and toxicity research.

Instead of mimicking the lung microenvironment, other studies focused on testing immune cell migration using clinical samples from patients with specific lung diseases for potential diagnostic applications. COPD is a type of lung disease associated with breathing difficulty, which is caused by narrowed airways [80]. A previous study had demonstrated the correlation between COPD and neutrophil chemotactic infiltration to the airways [81]. Thus, neutrophil chemotaxis has the potential to characterize and diagnose COPD. In this direction, Lin and coworkers developed a microfluidic device to study neutrophil chemotaxis to the supernatant gradient of sputum samples from healthy donors and COPD patients (**Figure 1.3A**) [6]. The results showed stronger neutrophil chemotaxis to the sputum of COPD patients than the sputum of healthy donors. In addition, the results confirmed the important chemical factors in COPD sputum for inducing neutrophil chemotaxis. More recently, the same group further developed an all-on-chip method for rapid analysis of neutrophil chemotaxis [58]. The novel device had a unique cell-docking structure that enabled cell alignment on one side of the gradient channel, permitting accurate and rapid chemotaxis readout without time-lapse cell tracking. In addition, neutrophils were directly isolated from a drop of blood using the on-chip magnetic separation method. In this study, a rapid and integrated neutrophil isolation and chemotaxis test to a known recombinant chemoattractant or clinical sputum from COPD patients was achieved in 25 min. These developments demonstrated the potential of a microfluidic-based cell migration test method for diagnosing inflammatory lung disease. As another example in a similar direction, Beebe and coworkers developed a microfluidic method to investigate chemotaxis of neutrophils from asthma patients for diagnostic application (**Figure 1.3B**) [44]. The device consisted of a lid part as the chemoattractant source, and a base part as the neutrophil capture sink. When the lid was placed onto the base, the chemoattractant diffused into a gradient in the microchannel to induce neutrophil chemotaxis. The results showed lower chemotaxis velocity of neutrophils in the samples from asthmatic patients compared to non-asthmatic patients, suggesting neutrophil chemotaxis can be potentially used for asthma diagnosis.

Figure 1. 3 Examples of lung-on-chip cell migration study.

(**A**) Microfluidics-based approach for investigating neutrophil chemotaxis with clinical samples for rapid diagnosis of COPD. The upper-left panel illustrates the microfluidic device; the upper-right panel shows a representative cell image in the device; the bottom-left panel shows cell migration test data using the microfluidic device (C.I.: chemotactic index); the bottom-right panel shows cell tracks from a representative experiment. (**B**) Microfluidics-based approach for investigating neutrophil chemotaxis with clinical samples for asthma detection. The upper panel illustrates rapid on-chip neutrophil isolation from blood; the bottom panel illustrates the microfluidic method for neutrophil chemotaxis test. fMLP: *N*-formyl-methionyl-leucyl-phenylalanine. **Figure 1.3A** is adapted from reference [6] with permission from PLOS; **Figure 1.3B** is reproduced from reference [44] with permission from the National Academy of Sciences.

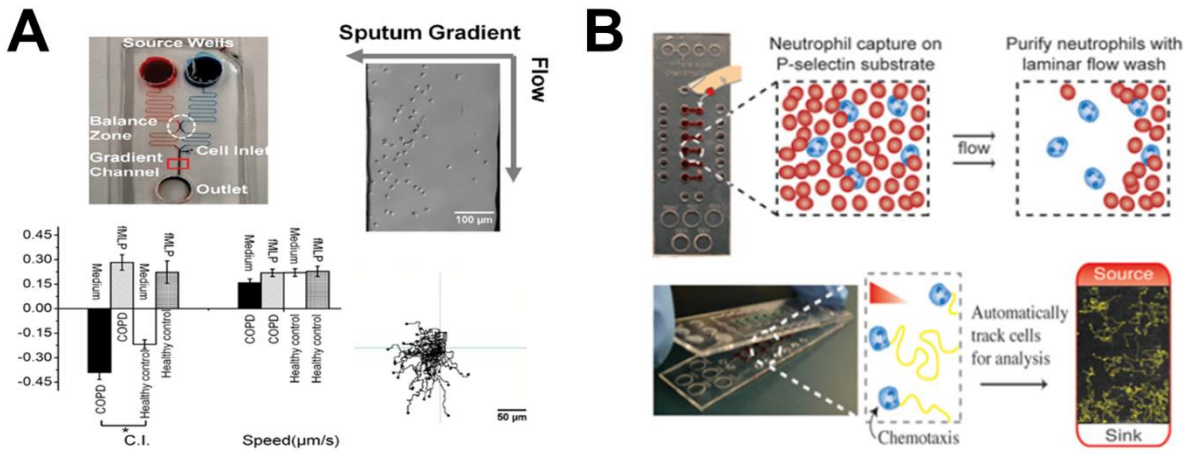

1.4.3 Vessel-on-chip

Leukocyte transendothelial migration (TEM) from blood vessels to inflammatory sites is a critical process for human immune responses. This migration process is mediated by both physical and chemical cues through complex interactions between leukocytes and ECs [82,83]. Similarly, the transendothelial invasion (TEI) of cancer cells through blood vessels to target tissues (i.e., tumor extravasation) is an important process during tumor metastasis [74,84]. These relevant research topics require more advanced microfluidic systems to configure the complex *in-vivo*-like vascular microenvironment for investigating different cell types involved in transvascular migration (TVM) during various pathological processes. Here we describe some examples of vessel-on-chip for TVM and angiogenesis studies (**Figure 1.4**; **Table 1.1**)

Chung and coworkers developed a vessel-on-chip model for investigating neutrophil TEM during inflammatory processes (**Figure 1.4A**) [52]. The microfluidic device consisted of five connected channels, including two side channels, two ECM channels and one EC channel. The ECM layer and EC monolayer patterning were achieved by collagen injection and EC seeding within the ECM channels and EC channel, respectively. The EC channel was loaded with neutrophils, and side channels were injected with growth medium and chemoattractants, reconstituting *in-vivo* TEM under multiple inflammatory stimulations. Different concentrations of *N*-formyl-methionyl-leucyl- phenylalanine (fMLP) and interleukin-8 (IL-8) were tested for inducing neutrophil chemotaxis. In addition, the number and migration behavior (e.g., distance and velocity) of neutrophils that transmigrated through both the EC monolayer and ECM layer were measured. These results showed that fMLP gradients more strongly attracted neutrophils than IL-8 gradients, and that neutrophil-EC interactions were indispensable to neutrophil TEM during the inflammation process. Despite its utility in the cell migration study, this system can be used as a potential disease model for drug screening as well.

In another study, Qin and coworkers developed a biomimetic blood-vessel-on-chip model for investigating tumor TEI (**Figure 1.4B**) [59]. The model reconstituted the primary features of physiological blood vessels, including vessel lumen, endothelium and perivascular chemokine-containing ECM. The main channel connected with medium inlet and outlet and

was filled with cancer cells and culture medium, serving as the lumen of blood vessels. The side channels connected to the main channel and matrix inlet and were filled with cultrex basement membrane extract (BME) and chemokines, mimicking the perivascular ECM. In addition, human umbilical vein endothelial cells (HUVECs) were seeded onto the BME surface to mimic endothelium. Based on this model, salivary gland adenoid cystic carcinoma (ACC) cell TEI was recorded and analyzed in real time under a well-controlled physiological microenvironment. The results demonstrated ACC TEI was induced by a C-X-C Motif Chemokine Ligand 12 (CXCL12) gradient, resulting in irreversible impairment of endothelial integrity. However, AMD 3100, an efficient CXCR4 antagonist, was able to inhibit this invasive process, but not inhibit the adhesion of ACC to the endothelium. This vessel-on-chip approach showed its feasibility for vasculature modeling and its potential for tumor TEI investigation.

As another example, Kamm and coworkers established a microvasculature-on-chip model for investigating tumor cell extravasation (**Figure 1.4C**) [60]. Briefly, the microfluidic device consisted of three hydrogel lumens, separated by medium channels in between, allowing chemical factor delivery and exchange. HUVECs–hydrogel and fibroblasts (FBs)-hydrogel mixtures were loaded into the middle and side hydrogel regions, respectively. The boundary between each hydrogel lumen and medium channel was made of an array of microposts that allow cell-hydrogel mixture expansion and paracrine interactions of HUVECs and FBs, simultaneously. After microvascular network (μVN) formation, tumor cells were injected through the HUVEC gel region for real-time observation. This vessel-on-chip model enabled multiple on-chip cell culture, mimicking of human vasculature reconstitution, and single cell tracking, allowing investigation of tumor TEM and micrometastases formation.

Besides these TVM-oriented studies, Neumann and coworkers developed a microvessel-on-chip model for investigating angiogenesis [61]. The device was made of two bonded PDMS stamps, embedded with two microfibers in between. The two parallel microchannels were interconnected by a main chamber. The chamber was injected by the mixture of collagen gel and human vascular pericytes. After gel formation, the microfibers were removed, and the top microchannel was perfused with growth factors, while HUVECs were introduced into the

bottom microchannel. This model reconstituted the 3D features of *in-vivo* vasculature, including tubular vessel structure, multiple cell co-culture, mimicked ECM substrate and controlled chemical microenvironment. Based on this vessel-on-chip model, the angiogenesis process was studied by observing directional migration of pericytes toward the growth factor gradient. This approach provided a new method for organotypic vasculature establishment, which facilitated studying cell migration related vascular functions.

Figure 1. 4 Examples of vessel-on-chip cell migration study.

(**A**) The vessel-on-chip model for investigating neutrophil TEM during the inflammatory process. The left panel shows the schematic presentation of neutrophil TEM under inflammatory conditions; the upper-right panel shows the dimensions of the microfluidic device; the bottom-right panel shows the schematic presentation of neutrophil TEM (side view). (**B**) The vessel-on-chip model for investigating tumor TEI. The upper-left panel shows the schematic presentation of tumor TEI; the bottom-left panel shows representative experimental images of tumor cells (red) during TEI; the upper-right panel shows the microfluidic device; the bottom-right panel shows representative experimental images of the selective area. (**C**) The vessel-on-chip model for investigating tumor cell extravasation. The left panel shows the microfluidic device and the detailed information of the selective area; the middle panel shows the magnified view of the selective area (green: microvascular network; red: tumor cells); the right panel shows representative experimental images of one transmigrating tumor cell in the white dashed box. PDMS: polydimethylsiloxane. **Figure 1.4A** is adapted from reference [52] with permission from the Royal Society of Chemistry; **Figure 1.4B** is adapted from reference [59] with permission from the Royal Society of Chemistry; **Figure 1.4C** is adapted from reference [60] with permission from Nature Publishing Group.

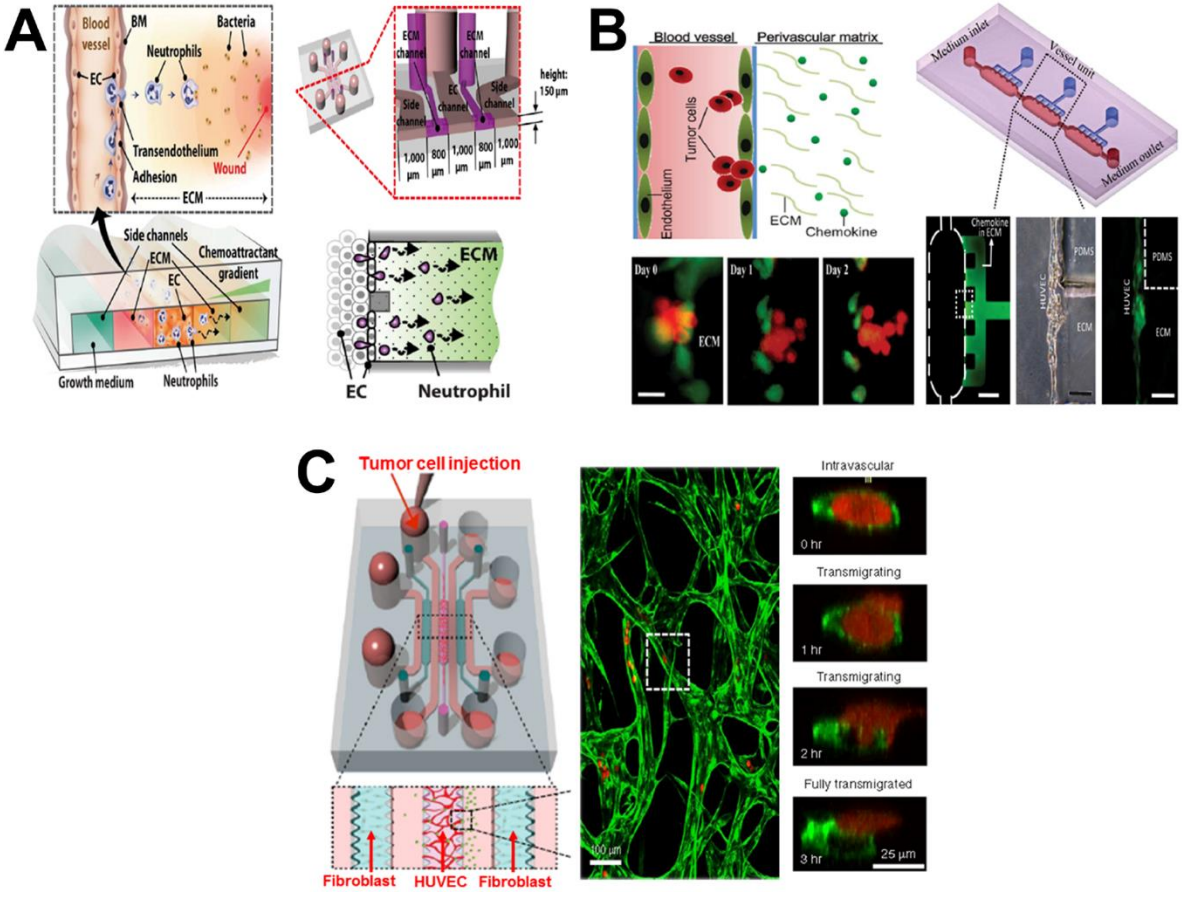
A
Blood vessel
BM
Bacteria
Neutrophils
EC
Transendothelium
Adhesion
Wound
ECM
Side channels
Chemoattractant gradient
Growth medium
Neutrophils
ECM channel
Side channel
height: 150 μm
1,000 μm
800 μm
EC
Neutrophil
B
Blood vessel
Perivascular matrix
Tumor cells
Endothelium
ECM
Chemokine
Medium inlet
Vessel unit
Medium outlet
Day 0
Day 1
Day 2
Chemokine in ECM
HUVEC
PDMS
C
Tumor cell injection
Fibroblast
HUVEC
Fibroblast
100 μm
Intravascular
0 hr
Transmigrating
1 hr
2 hr
Fully transmigrated
3 hr
25 μm

1.4.4 Lymph Node (LN)-on-chip

Dendritic cells (DCs) are the most-potent antigen-presenting cells (APCs) in the immune system [85]. Generally, DCs reside in the peripheral tissues without activation and upon antigen activation they migrate to LNs through lymphatic vessels. In LNs, DCs and T cells interact to enable the secondary immune response [86-88]. Both DCs and T cells express the C-C chemokine receptor CCR7, and C-X-C chemokine receptor CXCR4 [89,90]. However, how these receptors and their specific ligands interact to regulate the migration of DCs and T cells and DC-T cell communication within LNs is not well understood. An *in-vitro* model that faithfully mimics the LN microenvironment will greatly facilitate understanding DC and T cell migration and their interactions in LNs. In this direction, both 2D and 3D microfluidic models have been developed for immune cell migration studies in LNs (**Figure 1.5**; **Table 1.1**).

For example, a mimetic LN-on-chip flow device was developed for investigating the interaction between T cells and DCs (**Figure 1.5A**) [62]. The device was made of PDMS with one main flow channel connected with two inlets and two outlets, and bonded onto a glass slide. Within the channel, the biomimetic LN tissue was generated by adding different layers: (1) an adsorbed fibronectin (FN) layer; (2) an APC monolayer (which consisted of a DC monolayer and a lipopolysaccharide (LPS) and peptide-major histocompatibility complex (pMHC) layer mimicking chemokine-induced immune response); and (3) a T cell layer. T cells were injected continuously with well-controlled shear stress into the main channel using syringe pumps. At low flow speed (6 μm/min), antigen-specific T cells migrated to the APC monolayer independently, regardless of the flow direction. Moreover, under this low shear condition, stable accumulation of antigen-specific T cells on DCs was observed. Compared to CD8+ T cells, CD4+ T cells showed longer and stronger interactions (attachment and detachment) with APCs under varying shear stress conditions. In addition, a much more stable DC-T cell interaction was found in the presence of specific antigen than unspecific antigen. This LN-on-chip model allowed the investigation of the pMHC-T cell receptor (TCR) bonding mechanism under controlled mechanical force.

In another example, Yarmush and coworkers developed a microfluidic device for evaluating DC chemotaxis and DC-T cell interaction (**Figure 1.5B**) [63]. Briefly, the device was made up of two PDMS layers, including the top layer for chemotaxis compartment and the bottom layer for T cell chamber. By recording DC chemotaxis to CCL19 gradient in the chemotaxis compartment, migration behavior of DCs was measured. The DC-promoted T cell activation was evaluated by calculating the calcium level of T cells in the T cell chamber. Based on this LN-on-chip model, mature DCs (mDCs) were shown to cause stronger T cell activation than immature DCs (iDCs). In addition, these results demonstrated the overall T cell activation was mediated by the level of DC migration. This approach allowed systematic investigation of complex immune responses between specific immune cells, such as DC migration and maturation and T cell activation.

In another study, Swartz and coworkers established a 3D agarose-based microfluidic device for investigating differential chemotaxis of DCs to CCR7 ligands CCL21 and CCL19 (**Figure 1.5C**) [64]. The device consisted of three main parallel microchannels, including one central channel and two side channels. The central channel was seeded with cell-matrix mixture, while the two side channels were injected with chemokines or buffers, which generated a chemokine gradient in the central channel through agarose. This approach enabled the recapitulation of physiological microenvironment *in vitro* with specific chemokine gradients, advancing the knowledge of DC homing within LNs. The results showed similar DC migration to both CCL21 and CCL19 gradients at concentrations less than 60 nM. Moreover, DC chemotaxis was enhanced with increasing concentrations of a single gradient of CCL21 or CCL19 with higher migration in CCL21 gradients. In addition, DCs showed stronger migration toward the CCL21 gradient in the presence of a competing CCL19 gradient configured in the opposite direction.

Similarly, Lin and coworkers used a microfluidic device to configure simple or complex co-existing chemical fields for studying the guidance of CCR7 ligands during T cell migration in LNs (**Figure 1.5D**) [21]. The “Y”-shaped flow device consisted of two inlets with external perfusion to generate a stable gradient in the main channel. Based on this device, they quantitatively tested the migratory behavior of activated human peripheral blood T cells (aHPBTs) in single CCL19 or CCL21 gradients, and different combinatorial CCL19/CCL21

gradients at physiological doses. The results showed that aHPBTs migrate to the CCL21 gradient alone, but not the CCL19 gradient at the physiological dose. Interestingly, aHPBTs showed repulsive migration from the CCL19 gradient at a low dose with a uniform background of high-dose CCL21, which mimicked the gradient condition at the periphery of the T cell zone (TCZ) in LN. This repulsive migration suggested the role of CCL19 in mediating T cell egress from LNs. Collectively, this model presented an interesting combinatorial guiding mechanism for T cell migration in LNs by CCR7 ligands.

Hammer and coworkers also attempted to reconstitute the complex chemical microenvironment in LNs based on a network-shaped microfluidic flow device for investigating differential DC chemotaxis through CCR7 and CXCR4 signaling [14]. Using this device, well-controlled single and/or competing chemokine gradients were established, which mimicked the complex chemotactic environment in LN tissues. This study showed that CCL19, CCL21 and CXCL12 can potently induce directional DC migration. However, in competing chemokine gradients, CCL19 attracted DCs more effectively than CCL21 or CXCL12, contradicting the results in the 3D microfluidic device, which suggested the different migration and gradient sensing mechanisms in 2D and 3D environments.

Figure 1. 5 Examples of LN-on-chip cell migration study.

(**A**) The LN-on-chip flow device for investigating the interaction between T cells and DCs. The upper-left and upper-right panels show the real microfluidic device and its schematic illustration, respectively; the bottom-left panel shows one representative 3D confocal image of the interaction between T cells (red) and DC monolayer (green); the bottom-right panel shows the schematic illustration of the microchannel in side view. (**B**) The LN-on-chip model for evaluating DC chemotaxis and DC–T cell interaction. The upper panel shows the microfluidic device; the bottom panel shows representative data of CCL19 gradient-induced mature DC (mDC) migration. (**C**) The 3D agarose-based microfluidic device for investigating differential chemotaxis of DCs to CCL21 and CCL19. The upper panel shows the schematic illustration of microfluidic device (side view) (S1&S2: chemokine/buffer loading channels; C: cell–gel mixture injection channel); the bottom panel shows representative data of the average velocity (Vx) of DCs in the competing gradients (dark columns: 1.5 mg/mL collagen plus 10% Matrigel; white columns: collagen alone). (**D**) The LN-on-chip model for studying the guidance of CCR7 ligands for T cell migration in LNs. The upper-left panel illustrates the microfluidic device and the method for data analysis; the bottom-left shows a mimicked LN model with complex chemokine gradients; the right panel shows the proposed combinatorial guiding mechanism for T cell trafficking in LN. **Figure 1.5A** is adapted from reference [62] with permission from the Royal Society of Chemistry; **Figure 1.5B** is adapted from reference [63] with permission from the Royal Society of Chemistry; **Figure 1.5C** is adapted from reference [64] with permission from the National Academy of Sciences; **Figure 1.5D** is adapted from reference [21] with permission from PLOS.

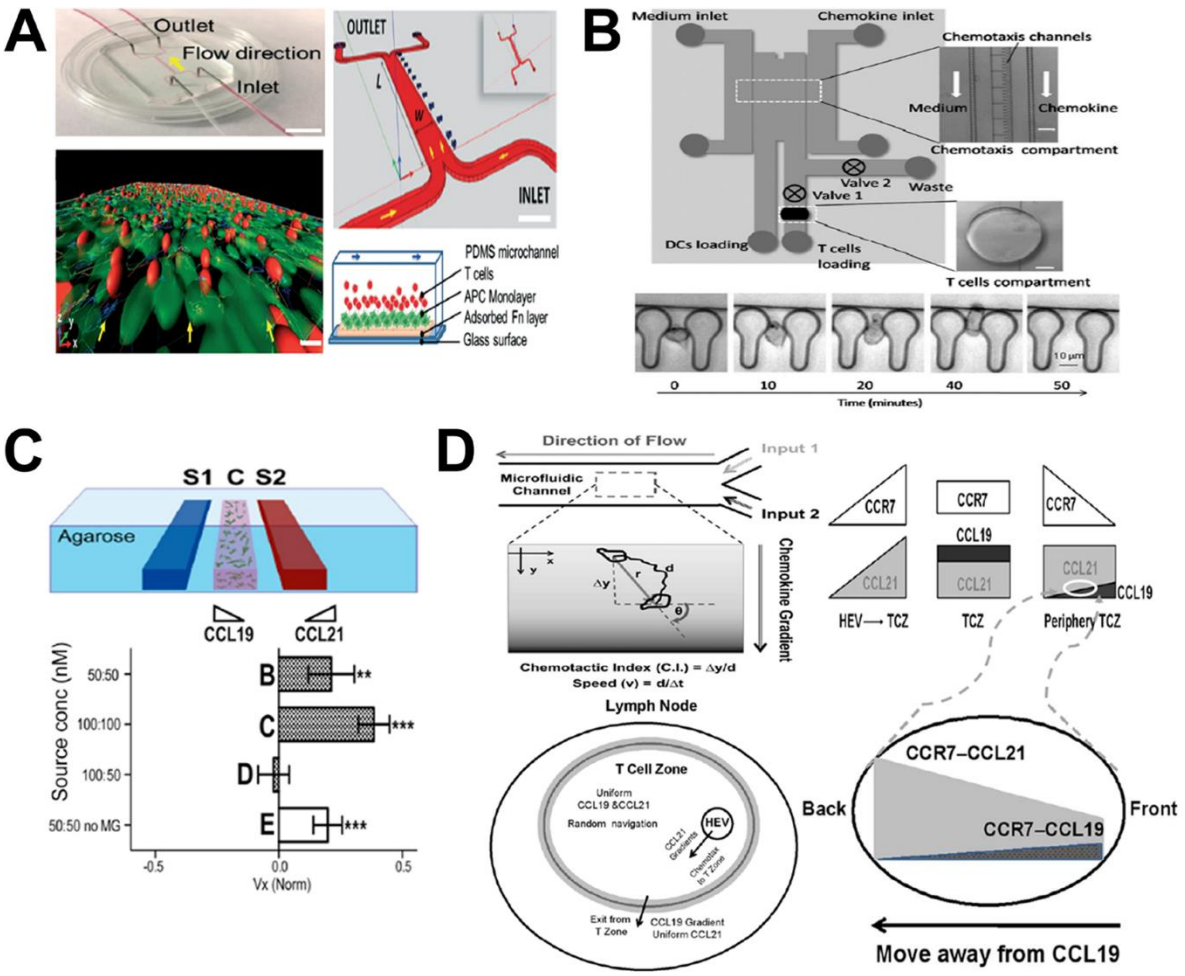
A
Outlet
Flow direction
Inlet
OUTLET
INLET
PDMS microchannel
T cells
APC Monolayer
Adsorbed Fn layer
Glass surface
B
Medium inlet
Chemokine inlet
Chemotaxis channels
Medium
Chemokine
Chemotaxis compartment
Valve 2
Valve 1
Waste
DCs loading
T cells loading
T cells compartment
10 μm
0
10
20
40
50
Time (minutes)
C
S1 C S2
Agarose
CCL19
CCL21
Source conc (nM)
50:50
100:100
100:50
50:50 no MG
B
C
D
E
**
***
***
-0.5
0.0
0.5
Vx (Norm)
D
Direction of Flow
Input 1
Microfluidic Channel
Input 2
Chemokine Gradient
Chemotactic Index (C.I.) = Δy/d
Speed (v) = d/Δt
CCR7
CCL21
HEV→ TCZ
CCR7
CCL19
CCL21
TCZ
CCR7
CCL21
CCL19
Periphery TCZ
Lymph Node
T Cell Zone
Uniform CCL19 &CCL21
Random navigation
HEV
CCL21 Gradient
Chemotaxis to T Zone
Exit from T Zone
CCL19 Gradient Uniform CCL21
CCR7–CCL21
CCR7–CCL19
Back
Front
Move away from CCL19

1.4.5 Brain-on-chip

Neural cell migration is an essential process during early embryonic brain development and for the central nervous system (CNS). Neural cell migration is regulated by various chemotactic factors such as inflammatory chemokine CXCL12 [91]. Furthermore, under pathological conditions such as ischemia or tumor growth, CXCL12 can regulate directional migration of neural progenitor cells (NPCs) towards the damaged tissues [92,93]. Therefore, it is important to better understand NPC migration guided by chemical cues in brain tissues, and OoC offers valuable experimental tools for such studies. Here we review some representative studies in this direction (**Figure 1.6**; **Table 1.1**).

A recent study generated a biomimetic brain-on-chip model for investigating neuronal differentiation and chemotaxis (**Figure 1.6A**) [65]. The device consisted of three PDMS layers. The top compartment was used to culture human brain microvascular endothelial cells (hBMECs) for modeling the blood vessels. The bottom compartment was used to culture glial cells and neuronal clusters for reconstituting the brain parenchyma. The top vascular and the bottom brain layers were separated by an intermediate porous membrane layer, which allowed the interactions of cells from both sides, mimicking the function of the blood–brain barrier (BBB). Using this approach, the differentiation of pluripotent human NTera2 clone D1 (hNT2) cells into mature neuronal and glial cells was achieved. Integration of this neuronal–glial environment with hBMECs enabled the reconstitution of CNS microenvironment *in vitro*. In addition, tissue-guided chemotaxis of human fetal neural progenitor cells (hNPCs) to different chemokine gradients, including CXCL12 and SLIT2, was also investigated. The results revealed enhanced hNPC chemotaxis in the "brain layer", indicating the migration of hNPCs *in vivo* is dependent on the signals in the surrounding CNS tissues.

As another example, Nery and coworkers developed a microfluidic-based method for investigating neuronal migration in embryonic brain explants (**Figure 1.6B**) [66]. Briefly, the microfluidic device was made of PDMS, which consisted of two compartments interconnected by multiple capillary microchannels. The compartments and microchannels were injected with gel matrix, mimicking the complex tissue microenvironment *in vivo*. One mouse medial

ganglionic eminence (MGE) explant and one cortical explant were cultured in the two compartments, respectively. Using this brain-on-chip model, individual neuron migration away from the MGE explant to the cortical explant through the capillary microchannels was observed, which demonstrated the long-distance migration of newborn neurons of embryonic MGE to the neocortex for brain development. In addition, this approach allowed observation of the distribution of cellular organelles within migratory neurons in real time, which enabled research to study neuronal migration and its related neurologic diseases.

In another study, Keenan and coworkers established a microfluidic-based method to investigate human neural stem cell (hNSC) neurogenesis [67]. Briefly, the PDMS microfluidic device consisted of two zygomorphic microchannels interconnected by three rectangular and three triangular gradient regions. All the gradient regions were selectively filled with hNSC suspension/Matrigel mixture to mimic the 3D brain ECM environment. The rectangular and triangular gradient regions were responsible for establishing linear and exponential gradients of fibroblast growth factor 2 (FGF-2), respectively. The results of this study demonstrated that the exponential FGF-2 gradient regulated the distribution of hNSCs, and correlated with hNSC neurogenesis, which promotes the development of the cerebral cortex.

In contrast to the above studies that focused on neuronal differentiation and migration, Qin and coworkers developed a mimetic organotypic microfluidic system that reproduced the principal structural, functional and mechanical features of the BBB *in vivo*, in order to investigate brain tumor metastasis (**Figure 1.6C**) [68]. The microfluidic device was made of PDMS, which consisted of 16 independent functional units interconnected by a microchannel network with a shared outlet. Each unit had four individual BBB regions, including one vascular channel for introducing fluidic flow; one gas valve for flow regulation; and four gel channels for loading ECM collagen or astrocytes. This approach reconstituted the key features and functionalities of BBB, including complex cellular interactions, diverse vascular cues, multiple barrier generation, cellular migration and 3D ECM establishment. Furthermore, it enabled real-time observation and analysis of BBB responses during brain tumor metastasis in a high-throughput manner. By using this brain-on-chip model, brain metastasis of human lung, breast and melanoma cells in the BBB microenvironment was investigated. The results

demonstrated that the interactions between cancer cells and astrocytes has the potential to promote invasion of malignant tumors to the brain and vascular compartments.

Figure 1. 6 Examples of brain-on-chip cell migration study.

(**A**) The brain-on-chip model for investigating neuronal differentiation and chemotaxis. The image shows the detailed information of the microfluidic system. (**B**) The brain-on-chip model for investigating neuronal migration. The upper-left & middle panels show the mouse embryonic brain explants (Cx: cortex; MGE: medial ganglionic eminence); the upper-right panel shows schematic presentation of the microfluidic device; the bottom panel shows representative experimental images of the selective areas. (**C**) The brain-on-chip model for investigating brain tumor metastasis. The image shows the schematic illustration of blood-brain barrier (BBB) and the microfluidic system with magnified views of selective regions. BMECs: brain microvascular endothelial cells. **Figure 1.6A** is adapted from reference [65] with permission from the Royal Society of Chemistry; **Figure 1.6B** is adapted from reference [66] with permission from Elsevier; **Figure 1.6C** is adapted from reference [68] with permission from Nature Publishing Group.

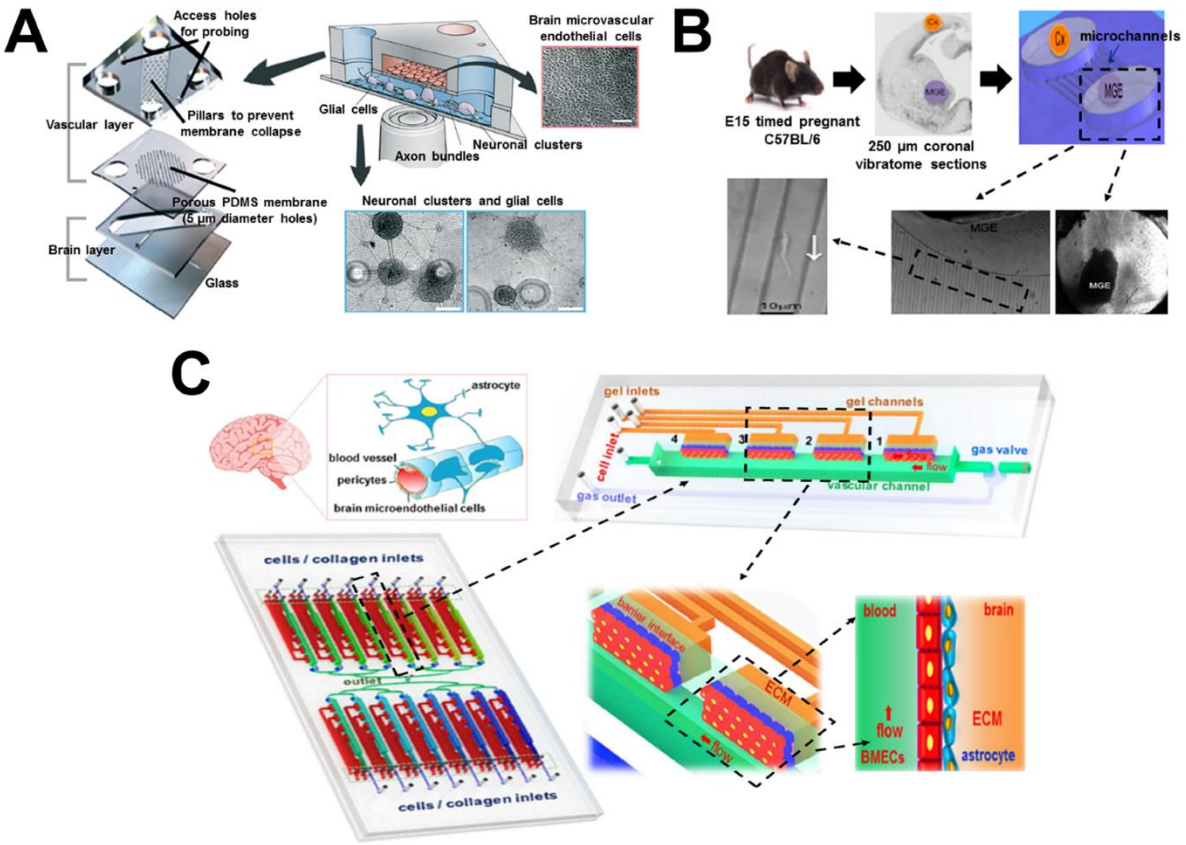

1.5 Motivation, rationale and outline of the thesis

1.5.1 Motivation

The migratory responses of immune cells play an important role in immune defense and maintaining homeostasis [94]. Misguidance on the normal immune cell migration leads to various pathological problems [23-32]. Understanding the mechanisms of immune cell migration is crucial and its investigation requires the development of a suitable research platform. Currently, various research tools (e.g., *in-vivo* animal models, traditional *in-vitro* assays, microfluidic devices, and OoC approach) have been applied for such purpose. Among them, OoC approach is a better research tool due to its ability to efficiently integrate interdisciplinary technologies such as cell biology, engineering, biomaterial technology, and microfluidics [95]. This approach offers a superior system that mimics the complex *in-vivo* microenvironment at the organ level to investigate the relevant immune cell migration. Although immune cell migration is important for homeostasis with high relevance to various diseases and OoC approach has the potential to undertake the mechanistic investigations, very few studies to date have applied OoC approach for disease-oriented immune cell migration. Therefore, our **overarching hypothesis** is that organ-on-chip development offers an advanced research approach to quantitatively evaluate the migratory response of immune cells under specific pathological conditions thereby advancing our understanding of the underlying biological mechanisms and enabling relevant biomedical applications.

1.5.2 Rationale

Developing a suitable OoC approach that configures the key features and responses of target organ for relevant immune cell migration is difficult, which requires the efficient coordination of solid background knowledge with technical skills. Thus, learning relevant literatures and technical skills was the major task in the beginning of my PhD study. Upon the publication of my first review paper (i.e., ***Cell migration research based on organ-on-chip related approaches***), I obtained enough knowledge and research skills of using microfluidic

approach for cell migration studies. From the time on, I started using these knowledge and skills to further investigate various disease-oriented immune cell migration.

As the collaborations between our lab and the local hospitals (i.e., the Seven Oaks General Hospital and the Victoria General Hospital) had been established, clinical samples including blood and sputum from both healthy subjects and COPD patients can be provided. I took this opportunity and perform the study in Chapter 2 first by using a triple docking device (D^3-Chip), to investigate T cell migration and chemotaxis in response to COPD sputum and the complex involvement of T cell migration in COPD. Although the device (i.e., D^3-Chip) applied in this study does not replicate the key physical structures of airway, at least this approach allows us to test the clinical cell and tissue samples in a mimicked microenvironment relevant to COPD.

The D^3-Chip was also applied to perform a collaborative study with Dr. Sam Kung (Department of Immunology, University of Manitoba) in Chapter 3, which aimed to further extend its usage from investigating the migratory responses of human immune cells (e.g., T cells and neutrophils) to a broader range of studies that include the migration of other cell types and cell-cell interactions. For such purpose, the primary murine NK cells, 4T1 cells, culture medium and the conditioned supernatants were applied in the device, and this study demonstrated the feasibility of using such approach to study directed NK-cell migration and NK-4T1 tumor cell interactions in a simulated tumor microenvironment. On the other hand, the limitations of approach complexity especially the absence of key physical structures of the target organs still exist in these studies, which needs further improvement. Thus, the devices applied in Chapter 2 and Chapter 3 can at best been called OoC related approaches.

Precise configuration of cellular components and guiding signals in space and time is one of the most important building block for the establishment of organ-specific features and the relevant microenvironment. Indeed, I tried different methods in this direction, including: 1) using 3D printing to make the device mold; 2) using micro-scaled fishing line, and 3) using UV-crosslinkable hydrogel in the D^3-Chip and other devices, to define the compartments of cellular components (e.g., ECM and cells) and chemical gradients. Unfortunately, none of them provided promising results in the end. Finally, I developed a novel microfluidic device with a

compact design of micropillars in the main compartment, and this device enabled the precise establishment of ECM, multi-cell co-culture, and relevant chemical gradients. Based on this device, a mimicked skin-on-chip (SoC) model was created that resembled key features of the human skin (i.e., epithelial, dermal, and endothelial components) and the relevant inflammatory chemical cues (i.e., single or co-existing chemical gradients). This SoC approach allowed us to quantitatively investigate the transendothelial and transepithelial migration of T cells in a mimicked skin inflammatory microenvironment and test chemotactic drug candidates.

1.5.3 Outline of the thesis

This thesis is mainly consist of six chapters, and each one has its independent structure and logic. Chapter 1 provides detailed background information of cell migration, chemotaxis, immune cell development and its importance for homeostasis and related pathogenesis. This chapter also includes and compares different methods (i.e., *in-vivo* animal models, traditional *in-vitro* assays, microfluidic devices, and OoC approaches) for cell migration, followed by detailed introduction of different cell migration studies based on various OoC related approaches. The last section of this chapter clarifies the motivation and outline of the thesis.

Chapters 2-4 include three research publications aim to use OoC related approaches to investigate immune cell migration. Specifically, Chapter 2 introduces a microfluidics-based airway-on-chip related approach, which simulates the airway microenvironment of COPD patient using clinical samples (i.e., blood and sputum). This approach allows us to quantitatively assess the effect of COPD sputum on T migration and chemotaxis under a mimicked microenvironment and provides important information on the complex involvement of T cell migration in COPD.

Chapter 3 introduces a microfluidics-based tumor-on-chip related approach. As a proof-of-principle study, it demonstrates the usage of such an approach for studying directed NK cell migration (e.g., migrated cell number and migration path) and NK-cancer cell interactions (e.g., the number and contact time of NK cells interacting with a cancer cell, and the change in cancer cell morphology at the end of the NK-cell interaction) in a mimicked tumor microenvironment in real-time.

Chapter 4 introduces a novel SoC model that reconstitutes cutaneous microenvironment *in vitro*, including key features of the human skin (i.e., epithelial, dermal, and endothelial components originated from human cell lines and extracellular matrix) and generation of dynamic single or co-existing chemical gradients of relevant chemokines during skin inflammation. This approach allows us to characterize the migratory responses of T cells at a single cell level in a mimicked cutaneous inflammatory microenvironment, and provide new insight for developing innovative immunotherapeutics such as screening potential chemotactic drugs.

Chapter 5 provides the conclusion on the key results, novelty of the system, and significance of the study. Chapter 6 describes the future directions of all the studies included in this thesis. Appendix includes some supplemental information of Chapter 4.

Chapter 2: Sputum from chronic obstructive pulmonary disease patients inhibits T cell migration in a microfluidic device

This chapter is written based on my publication: "**Xiaoou Ren**, Jiandong Wu, David Levin, Susy Santos, Ricardo Lobato de Faria, Michael Zhang, and Francis Lin. *Sputum from chronic obstructive pulmonary disease patients inhibits T cell migration in a microfluidic device*. ***Annals of the New York Academy of Sciences*** **(IF: 5.167)**, **2019**; 1445(1):52-61."

The study in this chapter was completed in the middle of my PhD study based on the collaboration between our lab and the local hospitals (i.e., the Seven Oaks General Hospital and the Victoria General Hospital). Specifically, we applied clinical samples in a triple docking device (D^3-Chip) to simulate the airway microenvironment of chronic obstructive pulmonary disease (COPD), and demonstrated the inhibitory effect of COPD sputum on the basal motility and chemotaxis of T cells through quantitative analysis. I performed all the experiments and data analysis, and I wrote the first draft and participated in all the revisions until its final publication.

2.1 Overview

COPD is a common lung disease characterized by the narrowed airways, resulting in serious breathing difficulty. Previous studies have demonstrated that inflammatory infiltration of leukocytes in the airway is associated with the pathogenesis of COPD. In the present study, we employed a microfluidic approach to assess the effect of COPD sputum on activated human peripheral blood T cell migration and chemotaxis under well-controlled gradient conditions. Our results showed considerable basal migration of T cells derived from peripheral blood of COPD patients and healthy controls in the medium control groups. By contrast, the migration of T cells from COPD patients and healthy controls was significantly inhibited in the presence of a gradient of sputum supernatant from COPD patients. Furthermore, chemotaxis of T cells from COPD patients or healthy subjects toward a SDF-1α gradient was clearly inhibited by sputum samples from the COPD patients. The inhibition effect revealed by the microfluidic

cell migration experiments provides new information about the complex involvement of T cell trafficking in COPD.

2.2 Introduction

COPD is a common lung disease with the characteristics of expiratory airflow limitation, which is correlated with abnormal intrapulmonary inflammatory responses of leukocytes in the airway [25-28]. Previous studies showed the involvement of the innate immune system in COPD, particularly infiltration of activated macrophages and neutrophils to the airway, is important for disease development [29-31]. In addition, adaptive immune responses are also involved in the pathophysiology of COPD [30,32]. As such, T cells are involved in cytolytic activities and secrete proinflammatory mediators, which recruit and activate other immune cells, resulting in tissue injury in COPD [24].

Previous studies have consistently suggested that inflammatory infiltration of T cells to the airway mediates pathogenesis of COPD [32,96,97]. Thus, understanding the mechanisms underlying the migration and trafficking of relevant immune cell types in COPD is required to elucidate the roles these cells played in COPD and to develop new diagnostic or therapeutic applications. Indeed, neutrophil migration and chemotaxis in response to airway-derived products in COPD has been extensively studied [6,81,98,99]. Neutrophil chemotaxis to supernatants of sputum from COPD patients was clearly demonstrated using cell migration assays *in vitro* [6,98,99]. Furthermore, key chemoattractants, including interleukin-8 (IL-8) and leukotriene B4 (LTB4), in the COPD sputum have been identified as mediating neutrophil chemotaxis [6,81,98,99].

Using a microfluidic device, we previously evaluated human blood neutrophil migration in response to COPD patients' sputum samples under well-defined gradient conditions [6]. Our results demonstrated greater neutrophil chemotaxis to the sputum supernatant from COPD patients than the sputum supernatant from healthy subjects, and it was correlated with the standard COPD diagnostic data (i.e., spirometry). These studies suggested the potential of neutrophil chemotaxis as a diagnostic biomarker for COPD. By contrast, to the best of our knowledge, studies of *in vitro* T cell migration in COPD are very limited. A previous study

showed increased migration of total peripheral blood mononuclear cells (PBMCs) from COPD patients in chemokine gradients but not of isolated lymphocytes [100].

To fill this gap, the present study was designed to evaluate the effect of the sputum supernatant from COPD patients on human blood T cell migration and chemotaxis. Different from our previous neutrophil migration study, we applied a new microfluidic device (i.e., D^3-Chip) [101] as the experimental platform. Initial cell alignment enabled by the docking structure of the D^3-Chip allowed more accurate cell migration and chemotaxis measurement. Based on the neutrophil migration results [6,81,98,99], our **working hypothesis** was that COPD sputum also attracts T cell migration, thereby supporting chemotaxis as a working mechanism for T cell infiltration into the airway in COPD. On the other hand, COPD sputum can trap inhaled particulate matters, pathogens, and toxins [26,102], and T cell migration can be particularly sensitive to various toxins. Relevantly, our previous study showed *Clostridium difficile* toxins A and B decreased the motility of human blood T cells, and toxin A further decreased T cell chemotaxis [103]. In addition, the current literature suggested that T cell chemotaxis to chemokine gradients in COPD requires cooperation with other blood leukocytes, such as monocytes [100], and T cell transendothelial migration can be inhibited by neutrophil-released elastase, which is of relevance to COPD [104]. Thus, our **alternative hypothesis** is that COPD sputum will not induce or affect migration and chemotaxis of purified T cells due to lack of interactions with other blood leukocytes or that COPD sputum will reduce or inhibit T cell migration due to negative regulators in the sputum, such as toxins and elastase.

2.3 Materials and methods

2.3.1 Collection of COPD patient samples

Ethics approval was granted by the Joint-Faculty Research Ethics Board at the University of Manitoba for obtaining sputum and blood samples from COPD patients. The consent form was provided to the participants by the recruiting staff employed at the Seven Oaks General Hospital (Winnipeg, Manitoba, Canada) following the procedures approved by the ethics board. All participants reviewed the consent form in detail and discussed any concerns or questions with the recruiting staff before they provided their consent signatures in the form. Sputum and

peripheral blood samples were both collected from each consented COPD patient (based on spirometry and physician diagnosis) at Seven Oaks General Hospital.

2.3.2 Collection of healthy control samples

Ethics approval was granted by the Joint-Faculty Research Ethics Board at the University of Manitoba for obtaining blood samples from healthy human donors. The consent form was provided to the participants by the recruiting staff employed at the Victoria General Hospital (Winnipeg, Manitoba, Canada) following the procedures approved by the ethics board. All participants reviewed the consent form in detail and discussed any concerns or questions with the recruiting staff before they provided their consent signatures in the form. Peripheral blood samples were collected from the consented healthy donors at Victoria General Hospital.

2.3.3 Preparation of sputum samples

Sputum samples from three COPD patients and three healthy subjects (non-COPD) were tested in this study. The COPD patients were labeled as patient A, patient B and patient C, and we labeled the sputum samples from specific COPD patients as SP_A, SP_B, and SP_C, respectively. Similarly, we labeled the sputum samples from specific healthy subject D, subject E, and subject F as SH_D, SH_E, and SH_F, respectively. Briefly, each sputum sample was transferred to a 1.5 mL Eppendorf tube and then mixed with 0.1% dithiothreitol (DTT) (Fisher Scientific) at an equal volume. All samples were vortexed, incubated in a 37°C water bath for 15 min, and then centrifuged at 2800 rpm for 10 minutes. The supernatants were transferred to another tube and centrifuged again at 3000 rpm for 5 min to completely remove the cellular components. The final supernatant samples were stored in a -80°C freezer before use.

2.3.4 Preparation of activated human peripheral blood T cells (ahPBTs)

Human peripheral blood samples were obtained from both COPD patients and healthy controls. PBMCs were isolated from the blood samples using the standard gradient centrifugation method. T cells within the PBMCs were selectively activated by anti-CD3/CD28 antibodies for 2 days in culture medium (RPMI-1640 with 1% penicillin-streptomycin and 10% FBS) in a 37°C incubator with 5% CO_2. ahPBTs were clonally expanded for at least 3 days in

the same culture medium with the addition of interleukin-2 (IL-2) at a final concentration of 12.5 ng/mL (R&D Systems) [40]. The purity of activated T cells is more than 91%, which has been confirmed previously by flow cytometry [40,105]. We labeled cells from the four specific COPD patients as CP_A, CP_B, CP_C, and CP_D, respectively. Similarly, we labeled cells from the three specific healthy donors as CH_A, CH_B, and CH_C, respectively.

2.3.5 Preparation of human blood neutrophils

Human blood neutrophils from healthy blood donor were isolated using a magnetic negative selection kit (EasySep Direct Human Neutrophil Isolation Kit, STEMCELL) according to the manufacturer's protocol. The highly purified neutrophils were incubated in medium (RPMI-1640 with 1% penicillin-streptomycin (P/S) and 10% FBS) in a 37°C incubator with 5% CO_2 before cell migration experiment within 8 h of isolation.

2.3.6 Preparation of the microfluidic device

A previously designed triple docking device (i.e., D^3-Chip) (**Figure 2.1**) [101] was employed in this study. The device has two layers of different thickness. The first layer (~ 3 μm high) serves as the cell docking barrier channels for trapping ahPBTs from the cell loading channels, while the second layer (~ 50 μm high) includes the ports and channels for cell loading, and the main gradient generating channels with chemical inlets and outlets. The microfluidic device was fabricated using previously described standard photolithography and soft lithography methods [21,106] in the Nano Systems Fabrication Laboratory and our lab in the Department of Physics and Astronomy at the University of Manitoba. Briefly, the device features were designed in SolidWorks (ver. 2012, Dassault Systems S.A.), and printed at 24,000 dpi resolution (Fineline Imaging) onto a transparency film that served as the photomask. The microfeatures were patterned onto a silicon wafer (Silicon, Inc., ID) by applying ultraviolet light through the photomask on top of the precoated SU-8 photoresist (MicroChem) layer. The patterned wafer was used as the master to replicate polydimethylsiloxane (PDMS) (Sylgard 184, Dow Corning) replicas. The PDMS replica was cut off from the master after baking for 2 h at 80 °C, and the inlets and outlets were punched out of the PDMS. The replica was bonded onto a glass slide using an air plasma cleaner and the device was then coated with collagen (20

μg/mL, BD Biosciences) for 1 h followed by blocking with migration medium (0.4% BSA in RPMI-1640) for another 30 min in the incubator before a cell migration experiment.

2.3.7 Preparation of the chemoattractants

In this study, the Medium & DTT group (migration medium: 0.1% DTT = 1: 1), and phosphate buffer saline (PBS) & DTT group (1× PBS: 0.1% DTT = 1: 1) were used as the two positive controls for basal T cell migration compared with the sputum group. Additionally, the stromal cell-derived factor-1 alpha (SDF-1α) group (a gradient of 100 ng/mL of SDF-1α in migration medium) was used as the positive control for T cell chemotaxis to compare with the SDF-1α-COPD group (a gradient of 100 ng/mL of SDF-1α in COPD sputum).

2.3.8 Setup of the cell migration experiments

ahPBTs were collected from the culture medium and resuspended in migration medium before being seeded into the cell loading channels. Each unit has two chemical inlets, and the migration medium and chemoattractant solution were injected into the two inlets, respectively, to generate the gradient. FITC-Dextran (10 kDa, final concentration of 5 μM, Sigma-Aldrich) was added to the chemoattractant solution to indicate the gradient profile. The device was placed under an inverted microscope (Nikon Ti-U) inside a temperature-controlled chamber (InVivo Scientific) at 37°C. Differential interference contrast (DIC) time-lapse images of cell migration were recorded every 20 s for 30 min (**Figure 2.1**).

2.3.9 Data analysis

Three different experimental groups were analyzed in parallel on each D^3-Chip and each experiment was independently repeated at least two times using separate D^3-Chips. The time-lapse images of ahPBTs were compared and analyzed within groups based on each device. Specifically, cells that migrated more than 20 μm (~ 2 times the cell size) toward the gradient direction within the microscope field were located, and the total displacement of each targeted cell in the gradient direction was measured in each group using NIH ImageJ. Quantitative parameters, including cell migration displacement and cell numbers, were extracted from the cell images (**Figure 2.1**). The data were reported in the tables and also presented using the Box

Chart function available in the OriginPro software (ver. 2017). Two-sample Student's t-test was used for statistical analysis of the data presented in the Box Chart to compare different conditions, and *$p < 0.05$ was indicated statistically significant difference.

Figure 2. 1 Illustration of the microfluidic device (D^3-Chip), microscope system and cell migration image analysis.

(A) Schematic illustration of the D^3-Chip. **(B)** Image of the three microfluidic channels and docked cells; the fluorescent image and profile plot of the FITC-Dextran gradient in the D^3-Chip. **(C)** An image of the microscope system for microfluidic cell migration assay. **(D)** An image of T cells in the D^3-Chip at the end of the assay and the illustration of cell migration displacement analysis.

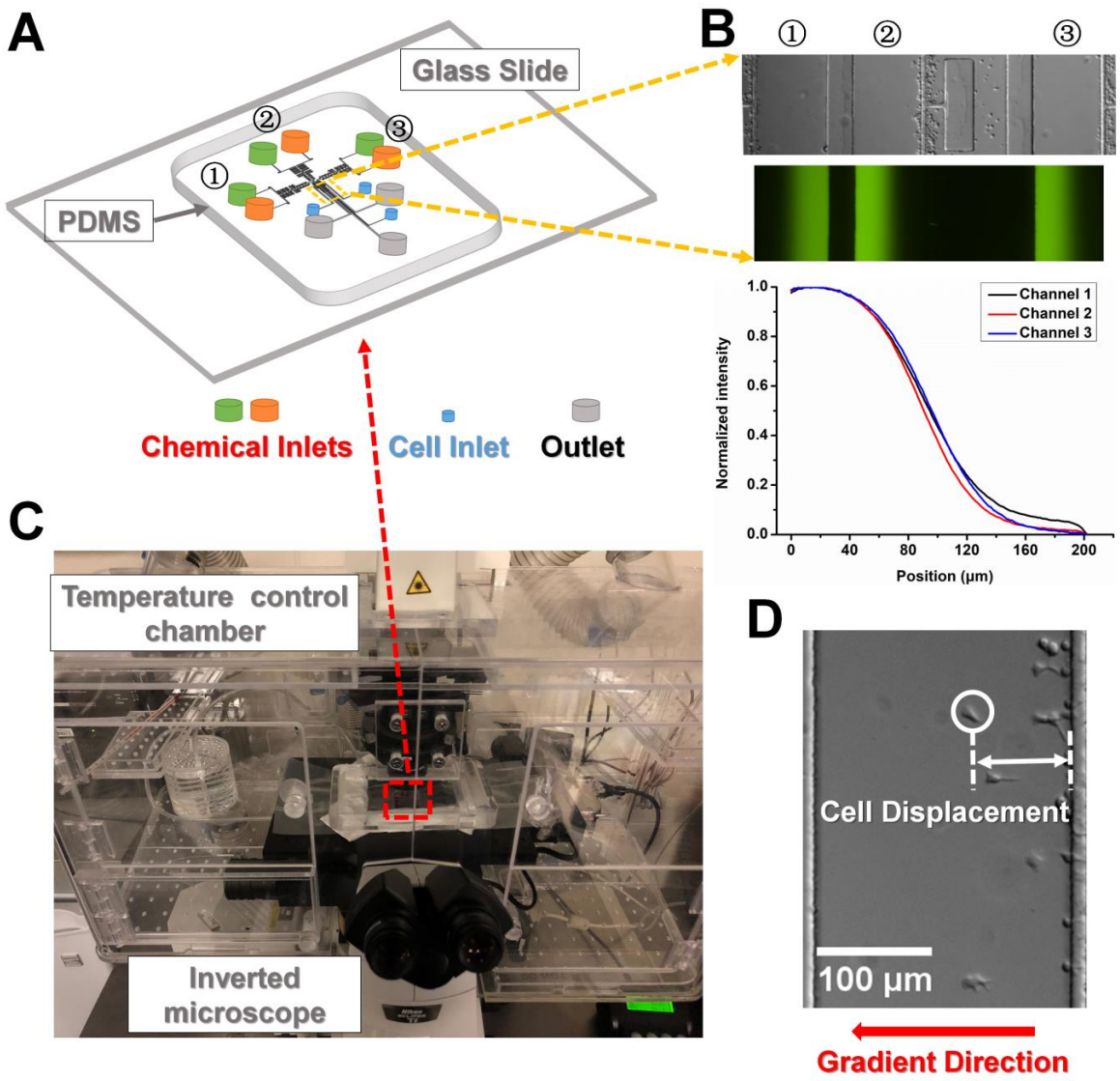

2.4 Results

2.4.1 The inhibitory effect of autogenous COPD sputum on basal T cell migration

Using the D^3-Chip, we first investigated the effect of autogenous sputum on the migration behavior of their corresponding ahPBTs. Our results showed that CP_A, CP_B, and CP_C migrated in the two DTT control gradients, which is consistent with the known basal motility of activated T cells (**Figure 2.2** and **Table 2.1**). By contrast, the migration of CP_A, CP_B, and CP_C was significantly inhibited in the presence of a gradient of their autogenous COPD sputum supernatants, as shown by fewer migrated cells and shorter average cell displacement compared with the two DTT control groups (**Figure 2.2** and **Table 2.1**). The results from the DTT control gradient groups excluded any possible effect of DTT in the sputum preparation on basal T cell migration.

Table 2. 1 Cell displacement and cell numbers for basal migration experiments.

The sputum samples from specific COPD patient A, patient B and patient C were labeled as SP_A, SP_B, and SP_C, respectively. T cells from specific COPD patient A, patient B, patient C, and patient D were labeled as CP_A, CP_B, CP_C, and CP_D, respectively. T cells from specific healthy subject A, subject B, and subject C were labeled as CH_A, CH_B, and CH_C. "N/A" indicates the conditions that not included in the experiments.

Displacement (Mean (SEM), μm), Cell Number		Conditions								
		SP_A	Medium &DTT	PBS &DTT	SP_B	Medium &DTT	PBS &DTT	SP_C	Medium &DTT	PBS &DTT
Cells	CP_A	28 (-), 1	58 (8.13), 20	54 (6.38), 24	N/A			27 (-), 2	44 (5.97), 22	35 (2.72), 17
	CP_B	23 (-), 2	43 (7.50), 14	40 (3.39), 18	24 (-), 2	35 (3.89), 14	55 (5.64), 24	N/A		
	CP_C	N/A			N/A			0	31 (2.98), 12	32 (3.27), 8
	CP_D	N/A			N/A			0	44 (5.21), 14	45 (3.90), 22
	CH_A	N/A			28 (4.72), 3	38 (3.23), 15	34 (1.55), 21	35 (-), 1	39 (3.57), 22	35 (3.71), 12
	CH_B	N/A			25 (2.50), 4	31 (2.14), 28	32 (2.49), 11	23 (0.81), 3	31 (2.26), 21	28 (1.68), 19
	CH_C	N/A			25 (1.66), 6	43 (3.98), 31	31 (2.57), 20	23 (-), 1	30 (1.76), 8	28 (2.97), 7

Figure 2. 2 Inhibitory effect of autogenous COPD sputum on basal T cell migration.

(A) Representative images of T cell migration (CP_B) in the two DTT control groups and the COPD sputum gradient group (SP_B) in the microfluidic device at the end of the 30-min experiment. **(B)** The displacement of CP_A and CP_B in different experimental groups from a representative set of experiments. The box chart shows the total displacement of each cell (migratory distance > 20 μm) in different experimental groups; the bottom and top of the red whisker shows the minimum and the maximum value; the red box shows the migratory cells within the range from 25% to 75% of total cells based on the ranked displacement value; the black bold line indicates the mean displacement; and the red line inside the box indicates the median displacement value. CP_A: cells from COPD patient A; CP_B: cells from COPD patient B; SP_A: sputum sample from COPD patient A; SP_B: sputum sample from COPD patient B.

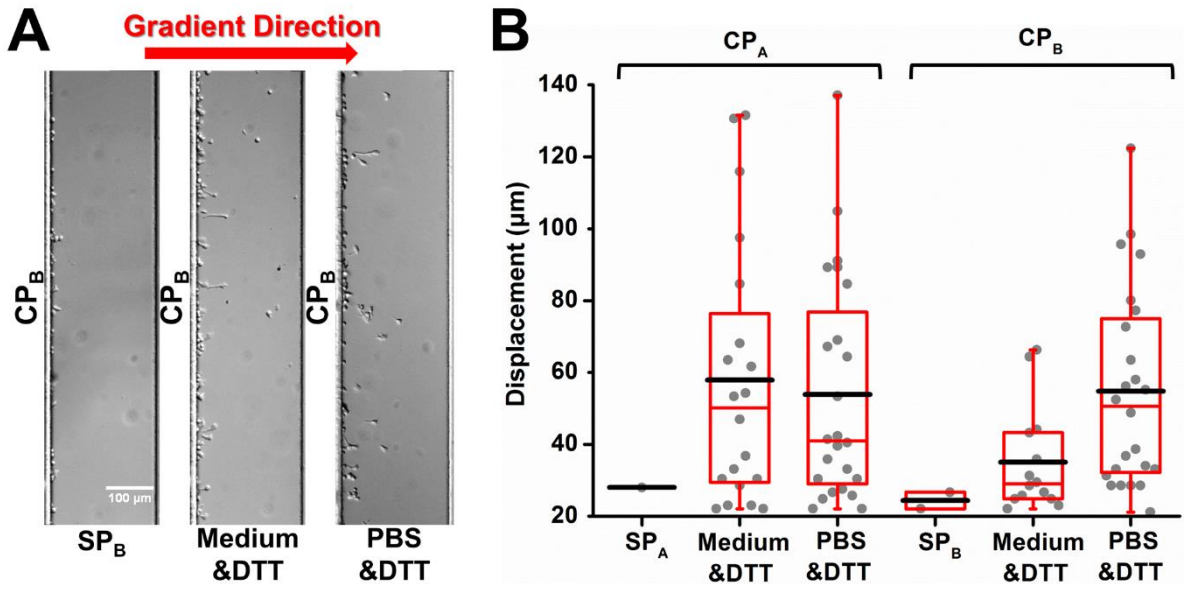

2.4.2 The inhibitory effect of COPD sputum on basal migration of T cells from other COPD patients.

The finding that COPD sputum inhibited basal T cell migration led us to examine if such an inhibitory effect is specific to T cells and sputum from the same COPD patient. Thus, we applied the D^3-Chip to further investigate the effect of COPD sputum on the migration behavior of T cells from other COPD patients. Our results showed that CP_A, CP_B, and CP_D migrated in the two DTT control gradient groups (**Figure 2.3** and **Table 2.1**). Interestingly, the results again showed the migration of CP_A, CP_B, and CP_D was significantly inhibited in the presence of a gradient of sputum supernatants from other COPD patients, as shown by fewer migrated cells and shorter average cell displacement compared with the two DTT control groups (**Figure 2.3** and **Table 2.1**). Collectively, these results revealed that COPD sputum samples have an inhibitory effect on basal migration of T cells from COPD patients.

Figure 2. 3 Inhibitory effect of COPD sputum on basal migration of T cells from other COPD patients.

The displacements of CP_A and CP_B in different experimental groups from a representative set of experiments are shown. The box chart shows the total displacement of each cell (migratory distance > 20 μm) in different experimental groups; the bottom and top of the red whisker shows the minimum and the maximum value; the red box shows the migratory cells within the range from 25% to 75% of total cells based on the ranked displacement value; the black bold line indicates the mean displacement; and the red line inside the box indicates the median displacement value. CP_A: cells from COPD patient A; CP_B: cells from COPD patient B; SP_A: sputum sample from COPD patient A; SP_C: sputum sample from COPD patient C.

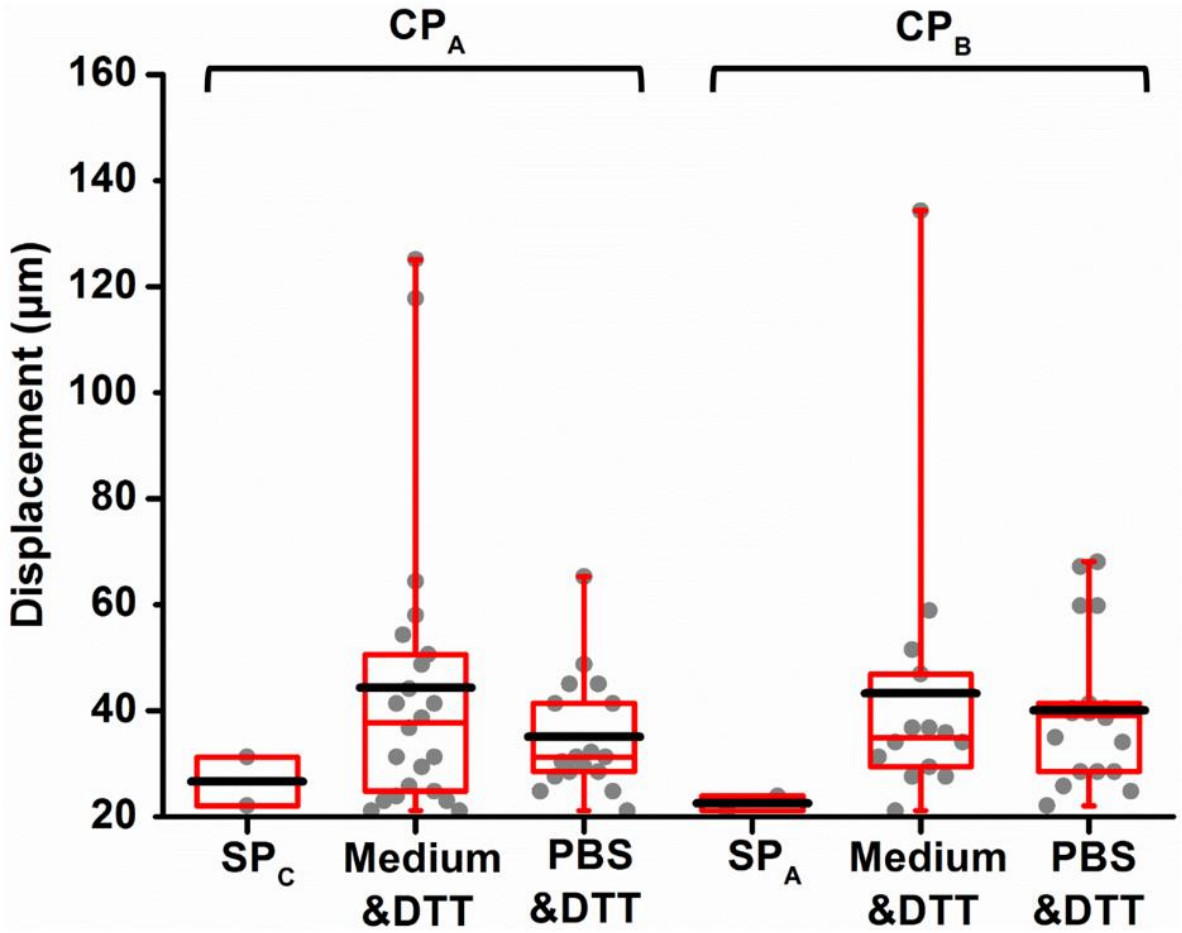

2.4.3 The inhibitory effect of COPD sputum on basal migration of T cells from healthy subjects

Next, we asked if the COPD sputum can also inhibit basal migration of T cells from healthy controls in our microfluidic device. Again, our results showed that CH_A, CH_B, and CH_C migrated in the two DTT control gradient groups (**Figure 2.4** and **Table 2.1**), while the migration of CH_A, CH_B, and CH_C was significantly inhibited in the presence of a gradient of sputum supernatant from COPD patients, as shown by fewer migrated cells and shorter average cell displacement compared with the two DTT control groups (**Figure 2.4** and **Table 2.1**). Thus, the results clearly showed that COPD sputum not only does not attract T cell migration but also has a general inhibitory effect on basal migration of T cells from COPD patients or healthy subjects.

Figure 2. 4 Inhibitory effect of COPD sputum on basal migration of T cells from healthy subjects.

The displacement of CH_A in different experimental groups from two representative sets of experiment is shown. The box chart shows the total displacement of each cell (migratory distance > 20 μm) in different experimental groups; the bottom and top of the red whisker shows the minimum and the maximum value; the red box shows the migratory cells within the range from 25% to 75% of total cells based on the ranked displacement value; the black bold line indicates the mean displacement; and the red line inside the box indicates the median displacement value. CH_A: cells from healthy subject A; SP_B: sputum sample from COPD patient B; SP_C: sputum sample from COPD patient C.

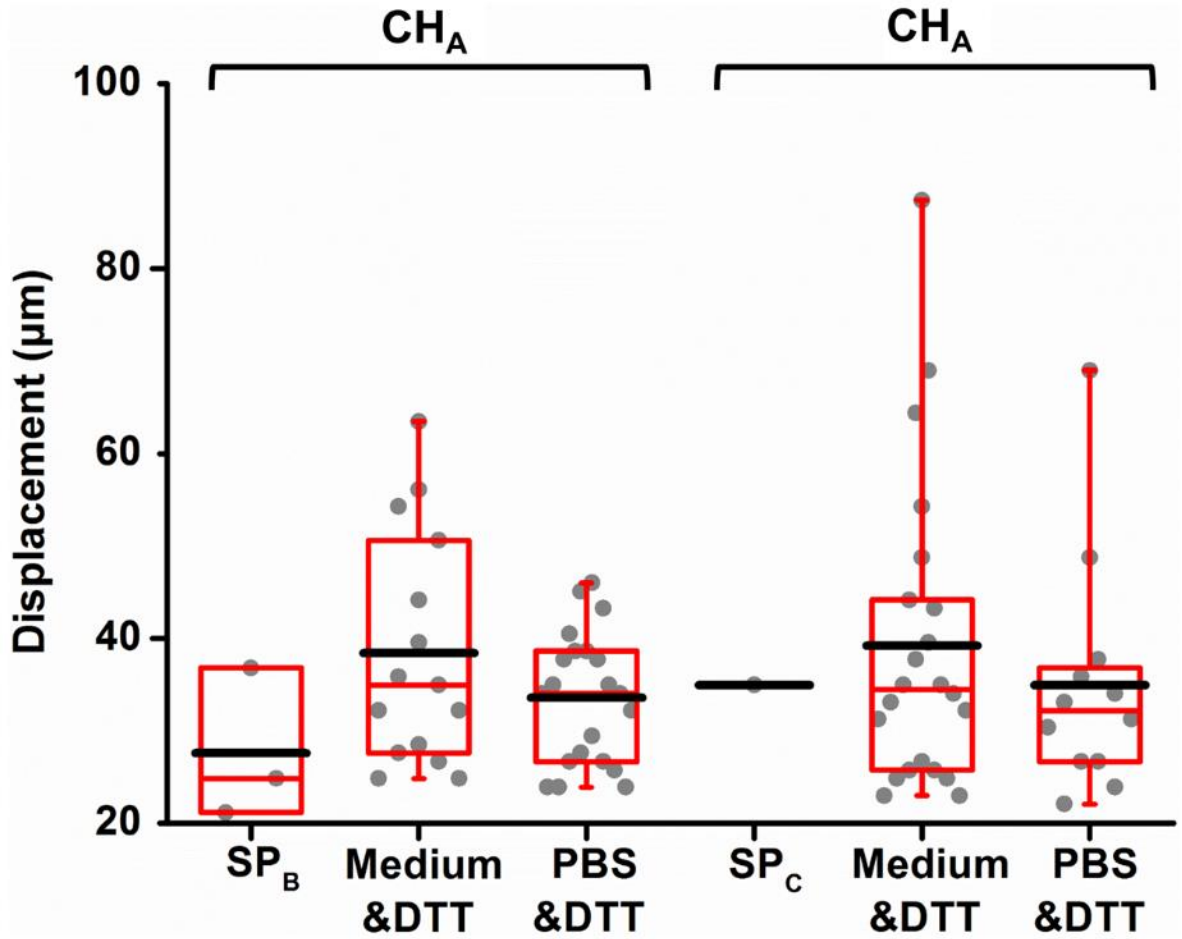

2.4.4 The inhibitory effect of COPD sputum on T cell chemotaxis to SDF-1α

Finally, we wanted to test the effect of COPD sputum on T cell chemotaxis to a known chemoattractant. For this, we examined the migration of T cells in a gradient of SDF-1α (100 ng/mL) with or without a coexisting gradient of COPD sputum supernatant in the same direction. Our results showed that both CP_A and CH_A strongly chemotaxed to the SDF-1α gradient, which is consistent with the literature (**Figure 2.5** and **Table 2.2**). In comparison, the migration of both CP_A and CH_A to the SDF-1α gradient was significantly inhibited in the presence of a coexisting COPD sputum gradient, as shown by fewer migrated cells (in some experiments, no cells migrated at all) and shorter average cell displacement (**Figure 2.5** and **Table 2.2**). Thus, COPD sputum also inhibited T chemotaxis induced by a SDF-1α gradient.

Table 2. 2 Cell displacement and cell numbers for chemotaxis experiments.

SP_C: sputum sample from COPD patient C; CP_A: cells from COPD patient A; CH_A: cells from healthy subject A; SDF-1α: stromal cell-derived factor-1 alpha.

Displacement (Mean (SEM), µm), Cell Number		**Conditions**		
		SP_C	**SDF-1α (100ng/ml)**	**SDF-1α (100ng/ml) in SP_C**
Cells	**CP_A**	**29 (-), 2**	**60 (5.54), 46**	**28 (-), 2**
	CH_A	**0**	**70 (5.48), 59**	**0**

Figure 2. 5 Inhibitory effect of COPD sputum on T cell chemotaxis to SDF-1α.

(A) Representative images of T cell migration (CH_A) in the two SDF-1α gradient groups and the COPD sputum gradient group (SP_C) in the microfluidic device at the end of the 30-min experiment. **(B)** The displacement of CP_A and CH_A in different experimental groups from a representative set of experiments. The box chart shows the total displacement of each cell (migratory distance > 20 μm) in different experimental groups; the bottom and top of the red whisker shows the minimum and the maximum value; the red box shows the migratory cells within the range from 25% to 75% of total cells based on the ranked displacement value; the black bold line indicates the mean displacement; and the red line inside the box indicates the median displacement value. Note that no cells migrated for CH_A in the "SP_C" group and the "SDF-1α in SP_C" group. SP_C: sputum sample from COPD patient C; CP_A: cells from COPD patient A; CH_A: cells from healthy subject A; SDF-1α: stromal cell-derived factor-1 alpha.

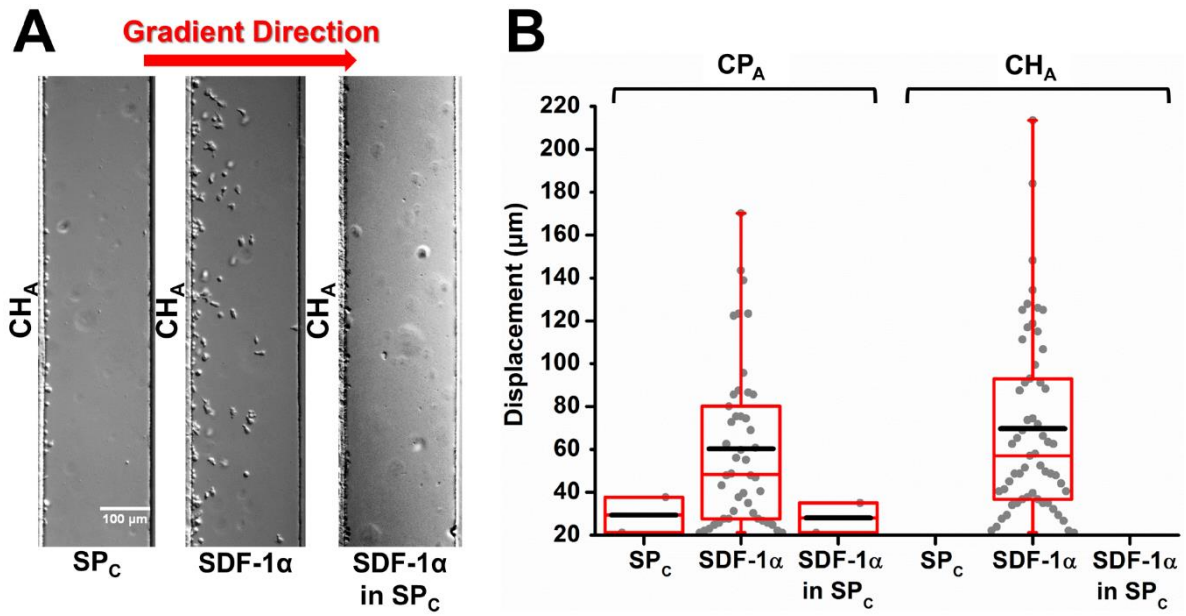

2.5 Discussion

In our study, we for the first time applied a microfluidics-based assay to the quantitative analysis of T cell migration and chemotaxis in COPD. The results showed that T cells from COPD patients and healthy controls migrated in the two DTT control gradient groups (Medium:DTT = 1:1 or PBS:DTT = 1:1), which is consistent with the known basal motility of activated T cells [40,107-109]. However, the migration of T cells from COPD patients and healthy controls was significantly inhibited in the presence of a gradient of sputum supernatant from COPD patients compared to the DTT gradient control groups.

We further tested the migration of T cells from both COPD patients and healthy subjects in Medium & DTT and PBS & DTT controls with increasing DTT concentration (i.e., DTT:Medium or DTT:PBS = 1:1 to have a final DTT concentration of 0.05%; 2:1 to have a final DTT concentation of 0.067%; 1:0 to have a final DTT concentration of 0.1%). Our results showed a significant number of migrated T cell and migration displacement under all conditions (even the 1:0 group without diluting DTT) (**Figure 2.6** and **Table 2.3**). Although in some cases the 1:0 group (i.e., 0.1% DTT without dilution, which represents the extreme scenario that 100% of the sputum supernatant is the 0.1% DTT) has fewer migrated cells and significantly lower migration displacement comparing to the 1:1 group and 2:1 group, the migrated cell number is still much higher than in the sputum supernatant gradient (i.e., very few cells migrated). The reduced migration in the 1:0 control group is also reasonable due to the lower content of physiological buffer. Thus, we believe that the observed inhibition of T cell migration in the sputum supernatant gradient is beyond any effect of the DTT itself. Interestingly, the migrated cell number in the 1:0 control group is relatively lower compared to the corresponding 1:1 group and the 2:1 group for T cells from COPD patients but not healthy subjects.

Table 2. 3 Cell displacement and migrated cell number for different concentrations of DTT in PBS&DTT and Medium&DTT controls for cells from COPD patient (CP_A) and healthy subject (CH_A).

The cell displacement data under different conditions were compared using the two sample Student's t-test, and * indicates $p < 0.05$ comparing to the 1:0 group. CP_A: cells from COPD patient A; CH_A: cells from healthy subject A.

Displacement (Mean (SEM), μm), Cell Number		Conditions					
		PBS&DTT Control (DTT:PBS)			Medium&DTT Control (DTT:Medium)		
		1:1	2:1	1:0	1:1	2:1	1:0
Cells	CP_A	39 (2.23) * 29	48 (5.32) * 24	31 (3.26) 12	63 (6.63) * 28	53 (5.06) * 26	33 (3.93) 13
	CH_A	47 (7.12) * 14	42 (10.12) 12	25 (1.71) 11	51 (8.78) 15	32 (4.05) 12	34 (3.61) 19

Figure 2. 6 Migration of T cells from COPD patient (CP_A) in different DTT concentrations in the PBS&DTT control.

(A) Representative images of T cell migration (CP_A) in the microfluidic device at the end of the 30 minute experiment. The DTT concentration is indicated as the mixing ratio of DTT: PBS for the DTT&PBS inlet: 1:1 for DTT concentration of 0.05%; 2:1 for 0.067%; 1:0 for 0.1%. **(B)** Comparison of cell displacement from the experiment in (A). The box chart shows the total displacement of each cell (only cells with displacement > 20 μm were included for analysis) in different experimental groups; the bottom and top of the red whisker shows the minimum and the maximum value; the red box shows the migratory cells within the range from 25% - 75% of total cells based on the ranked displacement value; the black bold line indicates the mean displacement; the red line inside the box indicates the median displacement value. The data under different conditions were compared using the two sample Student's t-test, and * indicates $p < 0.05$.

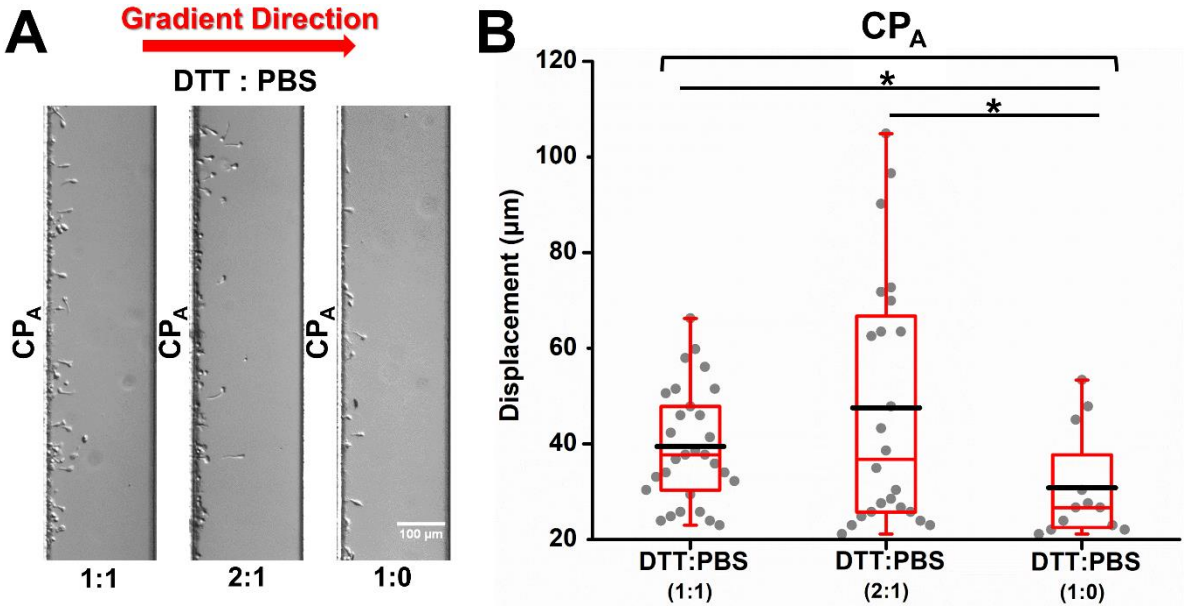

Furthermore, we tested the effect of sputum supernatant from healthy subjects on T cell migration. The results showed a significant number of migrated T cells and migration displacement comparing to the clearly inhibited T cell migration in the COPD sputum supernatant gradient (**Table 2.4**). Compared with the Medium & DTT control group and the PBS & DTT control group, T cell migration in the sputum supernatant gradient from healthy subjects varied quantitatively among different samples. These data further support the inhibitory effect of COPD sputum on T cell migration in microfluidic devices.

Table 2. 4 Cell displacement and migrated cell number in different sputum groups and DTT controls for cells from COPD patient (CP_A) and healthy subject (CH_A).

The sputum samples from specific healthy subject D, subject E, and subject F were labeled as SH_D, SH_E, and SH_F, respectively. The data showed CP_A and CH_A in the sputum supernatant gradient from COPD patient C (SPc), Medium&DTT (1:1) control, PBS&DTT (1:1) control, sputum supernatant gradient from healthy subjects SH_D, SH_E, and SH_F. The cell displacement data under different conditions were compared using the two sample Student's t-test. * indicates $p < 0.05$ comparing to the Medium&DTT group; $^{\#}$ indicates $p < 0.05$ comparing to the PBS&DTT group.

Displacement (Mean (SEM), μm) Cell Number		**Conditions**					
		SP_C	**Medium &DTT**	**PBS &DTT**	**SH_D**	**SH_E**	**SH_F**
Cells	**CP_A**	**27 (-), 2**	**44 (5.97), 22**	**35 (2.72), 17**	**74 (9.05) *# 18**	**30 (2.86) * 19**	**39 (8.94) 11**
	CH_A	**35 (-), 1**	**39 (3.57), 22**	**35 (3.71), 12**	**39 (9.05) 8**	**34 (2.67) 14**	**34 (10.39) 6**

The sputum supernatant from COPD patients also inhibited chemotaxis of T cells from COPD patients and healthy subjects to a 100 ng/mL SDF-1α gradient. As another relevant positive control, we showed that the same sputum supernatant gradient induced migration of neutrophils from healthy subject compared to the two DTT control gradient groups (**Figure 2.7**), which was consistent with the literature and our previous results based on another microfluidic device [6,98,99]. It is worth pointing out that the reason we did not do statistical comparison with some of our cell displacement data is because the number of migrated T cells in all sputum supernatant groups was very low comparing to the much higher number in the control groups (the red numbers in the tables). The opposite is true for the number of migrated neutrophils in DTT controls versus the sputum supernatant gradient. Collectively, our results support one of the scenarios predicted by our alternative hypothesis that COPD sputum inhibits T cell migration and chemotaxis.

Figure 2. 7 Neutrophil migration toward the COPD sputum supernatant gradient.

Three different experimental groups (i.e. SPc: sputum supernatant gradient from COPD patient C; Medium&DTT (1:1) control; PBS&DTT (1:1) control) were performed in parallel on each D^3-Chip following the similar experimental protocol and data analysis method for T cells. Each experiment was independently repeated at least two times using separate D^3-Chips. **(A)** Representative images of neutrophil migration in the COPD sputum supernatant gradient group (SP_C) and the two DTT control groups in the microfluidic device at the end of the 30 minute experiment. **(B)** Comparison of cell displacement from the experiment in (A). The box chart shows the total displacement of each cell (only cells with displacement > 20 μm were included for analysis) in different experimental groups; the bottom and top of the red whisker shows the minimum and the maximum value; the red box shows the migratory cells within the range from 25% - 75% of total cells based on the ranked displacement value; the black bold line indicates the mean displacement; the red line inside the box indicates the median displacement value. Note that no cell migrated in the Medium&DTT and the PBS&DTT control groups, and thus no data were shown in (B). The few cells in the channels in these two groups shown in (A) were either leaked into the channels during cell loading or moved less than 20 μm from the barrier channel. Therefore, these cells were excluded from the analysis.

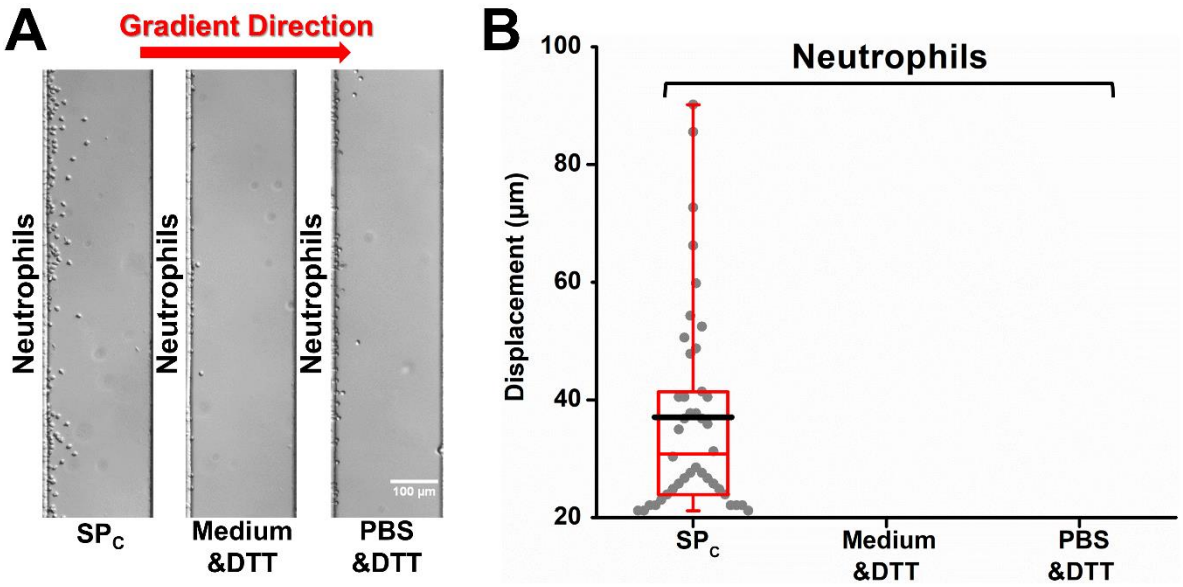

Compared with neutrophils, T cell migration and trafficking in COPD is not well understood. Finkelstein *et al.* first reported the increase in number of T lymphocytes in the lung in COPD patients, which is correlated with lung inflammation [96]. This was the first time that the adaptive immune system was suggested to be involved in the pathogenesis of COPD. Later studies further showed that the numbers of both CD4+ (helper) and CD8+ (cytotoxic) T cells increased in the airway and alveolar walls of COPD patients, with a predominant accumulation of CD8+ T cells, which is significantly correlated with the degree of airflow limitation [110,111]. Consistently, induced sputum samples from COPD patients contained high concentrations of various chemokines and cytokines, to which innate immune cells are capable of responding [112,113]. Thus, in one popular model, CD4+ and CD8+ T cells are recruited from the blood stream to the alveolar walls and airways of COPD patients, which is triggered by innate immune response; then the local accumulation of macrophages and neutrophils, and their continuous secretion of chemoattractants causes the clonal expansion of CD4+ and CD8+ T cells in the airway, which subsequently causes airway limitation in COPD [114]. The infiltration model motivated our working hypothesis in this study to test if COPD sputum can attract T cell migration *in vitro*.

However, our experimental results showed an inhibitory effect of COPD sputum on T cell migration and chemotaxis. In one scenario, we suspected that the observed inhibitory effect may be due to the simplified two-dimensional (2D) cellular microenvironment applied in the microfluidic device for T cell migration and the use of purified T cells for the experiments. The chemotactic migration of T cells to COPD sputum may require other physiologically relevant components of the microenvironment, such as 3D extracellular matrices and contact with endothelium or other leukocytes. Indeed, the previous study showing increased migration of total peripheral blood mononuclear cells from COPD patients to chemokine gradients but not isolated lymphocytes or monocytes suggests that synergy between different immune cell types enables enhanced cell recruitment to the lung in COPD [100]. These possible reasons can be further tested using more advanced microfluidic systems that better configure the microphysiological environment [1]. Relevantly, it will be also interesting to test inactivated T cells, which from our experience are known to have very different migratory responses in 2D

and 3D environments. Furthermore, new designs of microfluidic devices with higher throughput will allow us to reliably compare the effect of COPD sputum on different T cell subsets, such as CD4+ and CD8+ T cells by parallel migration experiments on a single chip.

In another scenario, the observed increase of T cells, particularly CD8+ T cells, in the airway in COPD based on flow cytometry or immunohistochemistry in previous studies does not necessarily assume T cell recruitment from the blood stream by chemotaxis. In fact, other studies reporting contradictory results also exist. In one study, no significant differences of the numbers of CD4+ and CD8+ T cells in either blood or sputum samples were found between COPD patients and healthy controls [115]. Another study showed comparable percentages of CD8+ T cells in the airway among all the study groups, including healthy nonsmokers, asymptomatic smokers, and male COPD patients [116]. Viral infections that commonly occur in COPD patients, such as by adenovirus or rhinovirus, may lead to foreign antigenic stimulus followed by CD8+ T cell response as a secondary antivirus function [117-121]. In this model, the innate immune response triggers the maturation and migration of dendritic cells (DCs) to the paratracheal lymph nodes, wherein T cells, especially CD8+ T cells, are activated and expanded [121,122]. While DCs in COPD patients failed to appropriately guide T cell responses, it resulted in a diffusive distribution of the expanded CD8+ T cells into the lung in a chronic inflammatory progression [121,123,124]. Thus, the increased appearance of T cells, particularly the predominant CD8+ T cells, in the airways in COPD may be due to its *de novo* origin or diffusive distribution rather than chemotaxis-based recruitment from blood in response to airway secreted chemotactic factors. In this context, the observed inhibitory effect of COPD sputum in our study may suggest a stop signal for the infiltrated T cells to accumulate in the lung, which facilitates the pathogenesis of COPD. We further suspect that the possible factors in the COPD sputum responsible for the inhibitory effect on T cell migration and chemotaxis may include various toxins and elastase. Further studies are required to identify these responsible components in the sputum and to better elucidate the underlying mechanisms and its physiological relevance to COPD.

Chapter 3: Applications of microfluidic devices in advancing NK-cell migration studies

This chapter is written based on my publication: "**Xiaoou Ren**, Abdulaziz Alamri, Jolly Hipolito, Francis Lin, and Sam K.P. Kung. *Applications of microfluidic devices in advancing NK-cell migration studies*. ***Methods in Enzymology*** **(IF: 1.862)**, **2020**; 631:357-370.

This study was conducted after completing the study in Chapter 2 based on our collaboration with Dr. Sam Kung's lab (Department of Immunology, University of Manitoba). The study in this chapter aims to extend the application of D^3-Chip from investigating the migration behaviors of human immune cells (e.g., T cells and neutrophils) to a broader range of cell types and cell-cell interactions. To this direction, we used primary murine natural killer (NK) cells and cancer cells with medium and conditioned supernatants in the device to mimic the tumor microenvironment. Our results demonstrated the feasibility of using this approach for investigating directional NK cell migration and NK-cancer cell interactions in real-time. Specifically, the primary NK cells, 4T1 cells, culture medium, and the conditioned supernatants were provided by Dr. Kung's lab; I performed all the experiments and data analysis, and I participated in the writing of first draft and all the revisions until its final publication.

3.1 Overview

Understanding how NK cells interact with tumor cells under specific microenvironment will be informative in development of NK-cell based immunotherapy. Applications of microfluidic devices in *in-vitro* studies of NK-cell migrations offer unique opportunities to examine NK-cell migrations at single-cell under controlled cellular microenvironments. Novel devices can be created and engineered to present precise configuration that mimics cellular microenvironments for cell migration studies. We established previously the first application of a simple Y-shaped device for imaging and analysis of the abilities of the immature and mature DC to regulate murine IL-2 activated NK cell migrations. Here we reported the application of our recent technical development of a novel microfluidic device, which is also called the triple docking device (i.e., D^3-Chip), for the studies of NK-cell migrations in NK-

4T1 breast cancer cell interactions *in vitro*. Key features of this microfluidic device are its pump-free gradient generation, and the three-parallel units design that supports easy setup and parallel comparison of multiple experimental conditions. The cell docking structure enables the prealignment of all NK cells at the same "start" position before their exposures to the test conditions. As a result, quantification of cell displacement toward a chemical gradient can be quantified by enumeration of the number of cells migrated out of the docking structure and their displacements. Such microfluidic devices can be further modified in future to mimic the complex *in-vivo* microenvironments to support more advanced investigations of NK-cell migratory responses *in vitro*.

3.2 Introduction

NK cells are bone marrow derived cells that constitute 10-15% of blood lymphocytes [15]. Unlike T cell, individual NK cell expresses a repertoire of surface receptors that can either be activating or inhibitory upon engagement of their cognate ligands. Functional activation of a NK cell thus depends on the balance of the activation and inhibitory signals it received [15,125]. Activated NK cells can induce direct cytotoxic killing of target cells, and/or production of soluble chemokines and cytokines (such as IFN-γ, TNF, and GM-CSF). These effector functions are critical in inducing innate and adaptive immunity in infections and cancer surveillance [15].

Unlike the NK-cell mediated cellular cytotoxicity and cytokine-production effector activities, migratory properties of NK cells in different experimental conditions are, in general, relatively less explored. NK cells indeed take clues from various microenvironments to regulate their migratory responses to traffic to peripheral tissues or inflamed lymph nodes to exert their immune-surveillance functions [15,126]. They acquire specific chemokine receptors and nonchemokine family proteins to regulate their preferential migrations to lymph nodes, liver, spleen or inflammatory sites [127,128]. In NK-dendritic cell (DC) crosstalk [129], we reported soluble factors produced by the immature or LPS-activated mature DCs would differentially regulate chemotactic abilities of the activated NK cells [130,131]. In tumor microenvironments, high level of CX3CL1 expression by breast cancer cells supported recruitment of tumor-

infiltrating CD8+ T cells, NK and DC cells [132]. Higher level of recruitment of these immune cell types in the tumor was correlated with a good prognosis for disease-free and overall survival. Forced expression of CKb-11 chemokine in breast cancer cell line recruited NK cells to the tumor site and promoted tumor rejections [133]. The underlying mechanism that determines high vs low infiltration of NK cells into tumor tissues, however, remains to be elucidated in details. It is possible that cancer cells produce factor(s) that prevent the infiltration of NK cells into the tumor environment. Studying NK cell migrations in conditions that mimics tumor microenvironments will therefore provide important insights into our understanding of NK cell immunosurveillance of cancer and in the development of NK cell based immunotherapy.

Microfluidic devices offer unique features that support studies of NK-cell migrations *in vitro*. Novel devices can be created and engineered to present precise configuration that mimics cellular microenvironments for cell migration studies [40,42,43]. Live-cell imaging supports examination of these migrating cells at single-cell level under controlled cellular microenvironments [1]. Migratory properties (such as speed, migration displacement, and chemotactic index) at the single cell level can be visualized and quantified. We have previously established the first application of a simple Y-shaped device for imaging and analysis of the abilities of the immature and mature DC to regulate murine IL-2 activated NK cell migrations *in vitro* [131]. Here we reported the application of our recent technical development of a novel microfluidic device (D^3-Chip) in the studies of NK-cell migrations in NK-cancer cell interactions *in vitro*. The D^3-Chip, comprised of three independent microfluidic units (each contains its own set of chemical inlets to generate a stable chemical gradient, a cell docking inlet and structures, and a waste outlet.), is an improved version of the well-established Y-shaped device (**Figure 3.1A**).

Figure 3. 1 Illustration of the D^3-Chip microfluidic system used in the migration study.

(**A**) Schematic illustration of the D^3-Chip. It is comprised of three independent microfluidic units. Each contains its own set of chemical inlets (two inlets to generate a stable chemical gradient), a cell docking inlet and structures, and a waste outlet. (**B**, **left**) Actual image of part of the observation zone to show the alignment of the three parallel and independent microfluidic channels (channel 1, 2, 3) created. Each one has its cell docking site and a test channel of defined chemical gradient for analysis of NK-cell migration. (**B**, **middle**) An image to show the "docking" of NK cells at a cell docking structure, and the fluorescent images of the gradient profile of each test channel. Fluorescent intensity at each position of the test channel was quantified. (**B**, **right**) The profile plots of the gradient in each test channel of the D^3-Chip were consistent, demonstrating the reproducibility of the gradient formation in all three test channels under the D^3-Chip. (**C**) An image of the microscopic system used in the imaging in the microfluidic cell migration assay. (**D**) A representative image obtained under the D^3-Chip to demonstrate the imaging of a migrating NK cell at the end of the assay and an illustration of cell migration displacement analysis.

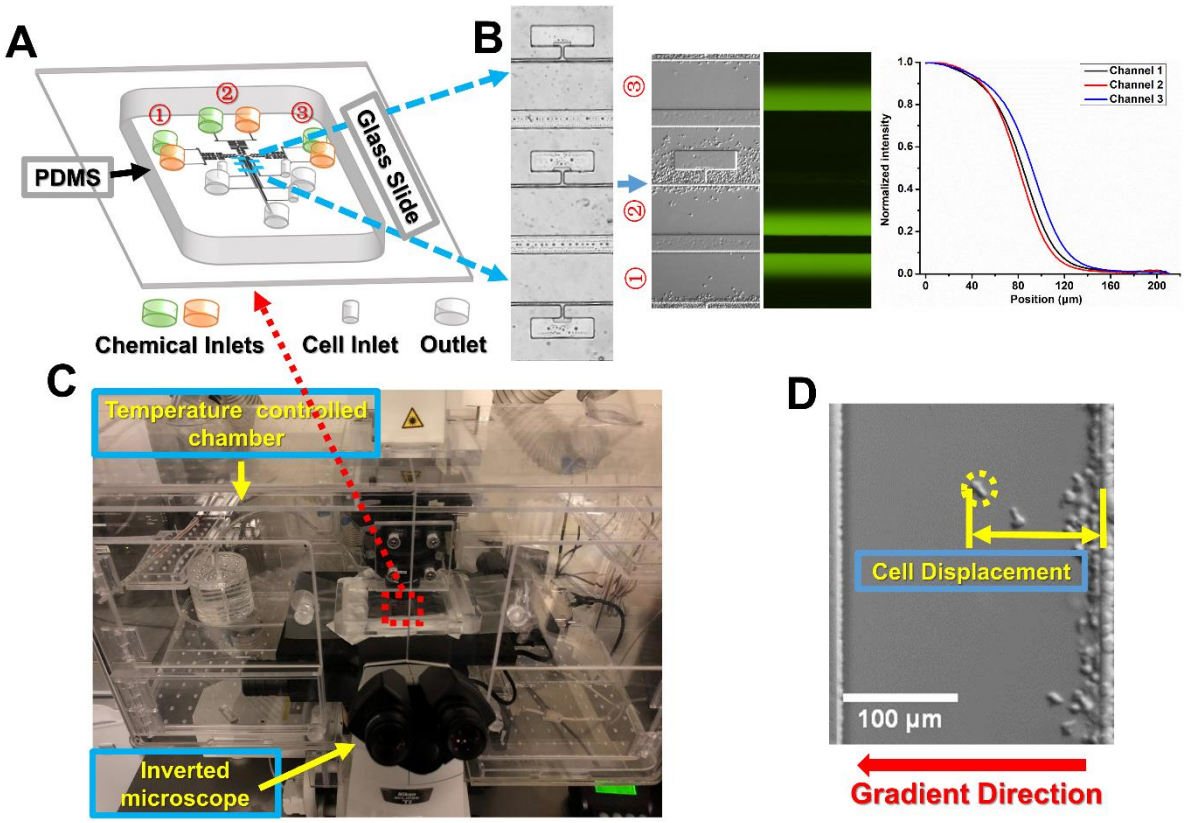

3.3 Materials and methods

3.3.1 Preparation of microfluidic devices

3.3.1.1 Design of microfluidic devices

A previously designed D^3-Chip (**Figure 3.1A**) [101] was applied in this study. This chip was designed based on a previous single-unit device [134] with the improved experimental throughput by coordinating three independent test units to fit into a combined view zone. All the parameters of this device were optimized to allow real-time imaging of all test units without the need of changing the stage. When needed, a programmable motorized microscope stage is used to support imaging at different positions. Each independent unit has its own corresponding chemical inlets (2, for the creation of a chemical gradient), cell inlet and outlet. The device therefore supports parallel analyses of three independent cell migrations experiments under different chemical conditions. The D^3-Chip contains a special cell docking area ensures the initial alignment of cells adjacent to a thin barrier region (**Figure 3.1B**). As the size of the loaded cells is larger than the barrier, the cells are "trapped" in the dock before a chemical gradient of interest is applied. Upon stimulation, the cells polarize and squeeze beneath the thin barrier region (3 μm high; 20 μm wide), and migrate toward the gradient direction in the main gradient channel (50 μm high; 220 μm wide). Unique features of this improved microfluidic device include: First, the cell alignment feature better controls the initial positions of all cells relative to the gradient at the beginning, thus allowing precise measurement of relevant parameters that involved in the cell migration and chemotaxis studies. Second, cell migrations through the barrier region stimulated by the chemical gradient partially mimic the process of transmigrated cells to the inflammatory tissues via blood vessels. Third, cell loading and gradient generation applied with all three independent units are fast and consistent, and the time interval between the setup of each unit is negligible. All the advanced features of D^3-Chip are integrated to ensure reliable results extracted from cell migration experiments.

3.3.1.2 Fabrication of microfluidic devices

The D^3-Chip was achieved by multi-height channels fabricated by two layers using the

previously published standard photolithography and soft lithography methods [58,101,106]. Detailed fabrication process was conducted in the Nano Systems Fabrication Laboratory (NSFL) at the University of Manitoba. The device feature was designed by SolidWorks software (Dassault Systemes S.A.), and printed to a transparency film at a high resolution (i.e., 24,000 dpi, Fineline Imaging) served as the photomask. The microfeature was negatively patterned onto an oxygen plasma pretreated silicon wafer (Silicon, Inc., ID) by employing UV exposure through the photomask on top of the precoated SU-8 photoresist (MicroChem) layer. The wafer with patterned features was used as the mold to reproduce polydimethylsiloxane (PDMS) (Sylgard 184, Dow Corning) replicas. The PDMS replica was cut off after 2 h of baking in an oven at 80 °C, all the inlets and outlets were punched with proper size. The surface of PDMS replica was cleaned by tape and bonded onto a new glass slide by using an air plasma cleaner (Harrick Plasma). The PDMS channels filled with DI water inside a 4 °C fridge can be kept up to a few days before use.

3.3.1.3 Substrate preparation

Rat tail collagen type I (Coring) is used for device coating, to provide a substrate for cell migration. Due to the microscale of the channel, a high concentration of the coating solution is employed to ensure the proper substrate surface density. In our experiments, 20 μg/mL of collagen solution is used for coating the D^3-Chip for 1 h in an incubator at 37 °C. The collagen-coated device is then blocked with completed culture medium for another 30 min in the incubator before cell migration experiment.

3.3.2 Generation of chemoattractant gradients

3.3.2.1 Principle of microfluidic gradient generation

The D^3-Chip generates a chemoattractant gradient by mixing continuous laminar flows of target chemicals in the microchannels [40]. The chemical gradient generation of each test unit is rapid, stable, independent, controlled, and pump-free. Depending on the pressure difference of the volumes between the inlet and outlet solutions, the flows are driven from chemical inlets through upstream serpentine channels and downstream main gradient channels to the corresponding outlets. The upstream serpentine channels balance the flows and decrease

the flow speed, which ensure a stable gradient generated within a few minutes inside the main gradient channels (**Figure 3.1B**). The D^3-Chip is capable of generating single or overlapped gradients, and rapid gradient switching.

3.3.2.2 Measurement of chemoattractant gradients in microfluidic devices

Fluorescent additives are added into the target chemoattractant solutions for visualizing and measuring the profile of chemo-attractant gradient in the microchannel using a standard fluorescence microscope. Here, we used FITC-dextran (10 kDa) based on the similar molecular weight of the most chemokine molecules. Typically, < 2% of the dye to the total volume is added to the test chemoattractant preparation, to minimize its effect on the migratory behaviors of cells during experiment. We showed that gradient generation of all three test units in the D^3-Chip are consistent and the gradient profile is stable for at least 1 h, which was sufficient for NK-cell migration experiments (**Figure 3.1B**).

3.3.3 Preparations of cells

3.3.3.1 Primary NK cells

We isolated primary NK cells from murine splenocytes (either C56BL/6 or BALB/c) using the EasySep mouse NK negative selection kit (StemCell Technologies, Vancouver, BC), according to the manufacturer's protocol. To obtain activated NK cells, we cultured these isolated NK cells at 37 °C and 5% CO2 in mouse medium containing 10% fetal bovine serum (FBS from Hyclone), 1% PSG (Invitrogen), 1.6 mmol/L 2-ME, in the presence of either IL-2 (1000 U/mL) or IL-15 (20 ng/mL) for 4 days. The purity of the activated NK cells was routinely > 90% by flow cytometry [131].

3.3.3.2 Preparation of dendritic cells conditioned medium

Murine bone marrow cells were collected from the femur and tibia, incubated with ACK buffer for 2 min to lyse red blood cells [130]. They were seeded ($0.5\text{-}1 \times 10^6$ in 1 mL per well) in a 24-well plate containing RPMI 1640 (Hyclone) medium supplemented with 1% PSG, 10% FGS, 1.6 mmol/L 2-ME and 20 ng/mL GM-CSF (Peprotech). On day 3, one-third of the culture medium was replaced by fresh GM-CSF containing complete culture medium to remove

nonadherent cells. On day 5, the DC cultures were again replenished with fresh GM-CSF containing complete culture medium to generate immature DC. On day 7, lipopolysaccharide (LPS at 1 μg/μL final concentration) was added to these immature DC cultures for 24 h to obtain LPS-activated mature DC. All the immature and LPS-activated mature DC cells were confirmed by the maturation markers (CD40, CD80, CD86) in flow cytometry [130]. Cell-free conditioned medium from either immature DC or LPS-activated mature DC were collected and used in the generation of the chemical gradients in the studies of NK-cell migrations.

3.3.3.3 Culture of 4T1 breast cancer tumor cells

Mouse 4T1 cell line (ATCC CRL-2539) produces primary and metastatic breast tumors which resemble stage IV human breast cancer, when injected into BALB/c mice [135]. The cells were maintained in complete RPMI1640 Medium supplemented with 10% (final, v/v) fetal bovine serum according to the ATCC culture protocol. Cells are maintained at subconfluence conditions. Adherent cells are detached using 0.25% trypsin, 0.53 mM EDTA solution.

3.3.4 Experimental setup

3.3.4.1 Cell loading

The culture flask contains 4T1 cells was treated with Trypsin-EDTA solution (0.25%, Sigma-Aldrich), and then put inside an incubator (37 °C; 5% CO2) a few minutes for cell detachment. The 4T1 cells were washed and resuspended in the complete RPMI 1640 culture medium before seeding. Ideally, 200,000 cells in 20 μL volume of the complete culture medium were prepared, loaded into the outlets of all three test units, followed by balancing the corresponding chemical inlets with proper volume of the culture medium in order to make enough cells suspended within the main gradient channels. The chip was then incubated inside the incubator for at least 1 h for the attachment of 4T1 cells. Activated NK cells (either IL-2 or IL-15-activated NK cells) were then collected from the multiwell plate and resuspended in the complete RPMI 1640 culture medium before loading. Typically, 100,000 cells in 10 μL volume of the culture medium were injected inside each cell loading inlets.

3.3.4.2 Chemoattractant preparation and injection

In this study, the conditioned medium of the LPS-activated mature dendritic cells (mDCs) was used as the chemoattractant [130,131]. Plain RPMI 1640 culture medium supplemented with 10% fetal bovine serum (FBS from Hyclone), 1% PSG (Invitrogen), 1.6 mmol/L 2-ME, was used as the medium control. In the chemo-attractant group, conditioned medium of mDCs and culture medium were injected into the two chemical inlets, respectively, to generate the gradient. In the medium control group, both chemical inlets were injected with the medium control. FITC-Dextran 10 kDa was added to these gradients to confirm the gradient profiles as we described previously.

3.3.4.3 Environmental control and image system

A live cell image system that consists of an inverted microscope (Nikon Ti-U) and a temperature-control enclosure chamber (InVivo Scientific) is employed for cell migration experiments (**Figure 3.1C**). The microfluidic device is placed on a programmable motorized stage under the microscope for cell migration imaging. A temperature-controlled chamber encloses the entire microscope stage to maintain a temperature at 37 °C during the experiments.

3.3.4.4 Time-lapse optical microscopy

After the desirable temperature at 37 °C was reached and the activated NK cells were loaded, a visualization field was chosen in the main gradient channel with a 10 × objective. Differential interference contrast (DIC) images are recorded in a time-lapse manner (10 s interval, 40 min long) during cell migration experiment. The gradient was checked both before and after the experiment.

3.4 Results and data analysis

3.4.1 Image processing

A single D^3-Chip supported analyses of three independent cell migration studies ran in parallel and independently. The experimental conditions tested under these three migration studies in a single D^3-Chip could be either identical (as intra-assay repeats) or different. For

examples, we could perform a single D^3-Chip to examine NK-cell migrations under control medium, conditioned medium from immature DC culture and conditioned medium from LPS-activated mature DC culture). Under such designs, each experimental condition would be repeated independently at least two more times under separate D^3-Chips. The time-lapse images were extracted from each set of the experiments, then compared and analyzed within different conditions based on the same device (**Figure 3.2A**).

3.4.2 Statistics analysis

Two sample Student's t-test available in the OriginPro software (ver. 2017) was used in the statistical analyses of two data groups.

3.4.3 Characterization of cell displacement

NK cells that migrated > 50 μm (~ 5 times of the cell size) to the gradient direction within the observation zone by the end of each experiment (40 min) were located, and NIH ImageJ was applied for calibrating the total displacement of each targeted cell in the gradient direction. Quantitative parameters including the number and displacement (**Figure 3.1D**) of migrated cells in the images were extracted, which was presented in the Box Chart (**Figure 3.2B**) by using OriginPro software (ver. 2017). Higher migration displacement of activated NK cells toward the gradient of the mDC conditioned medium were observed when compared to the medium control group (**Figure 3.2A and B**).

Figure 3. 2 Representative data to illustrate how measurements of NK-cell migration and cell-cell interaction were extracted from the microfluidic system.

(**A**) IL-15 activated NK cells (yellow) and 4T1 breast cancer cells (red) were loaded in the microfluidic device as described. Migrations of the activated NK cells toward the 4T1 cells were compared using gradient generated from either the conditioned medium from LPS-activated mature DC (supernatant of mDC) or the medium control. Representative images of the 4T1-NK cells interactions in the D^3-Chip under different conditions at 0 and 40 min were shown. The white dashed box indicated the section where 4T1 and NK cells were compared. (**B**) Comparison of the displacement of the IL-15 activated NK cells in either medium control or supernatant of mDC at 40 min. The box chart showed the total displacement of each cell (only cells with displacement > 50 μm were included for analysis) in different experimental groups; the bottom and top of the red whisker showed the minimum and the maximum value; the red box shows the migratory cells within the range from 25% to 75% of total cells based on the ranked displacement value; the black bold line indicated the mean displacement; the red line inside the box indicated the median displacement value. (**C**) The top image showed five IL-2 activated NK cells interacting with one 4T1 cell in a magnified image. The bottom table showed the detailed information about these interactions. (**D**) The left image showed one migrated IL-2 activated NK cell interacting with multiple 4T1 cells (no. 1-7) in a magnified image. The right table showed the detailed information about these interactions. The red bold line indicated the migration route of the NK cell. The arrow indicated the start-point. (**E**) Two images showing the start-point and endpoint of one IL-2 activated NK cell interacting with one 4T1 cell, respectively. The green and yellow dashed lines indicated the 4T1 cell and the activated NK cells, respectively, in (C-E).

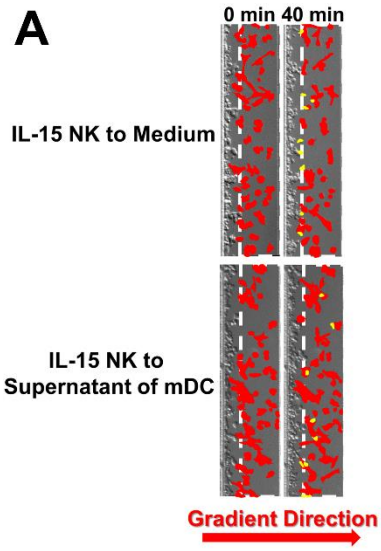

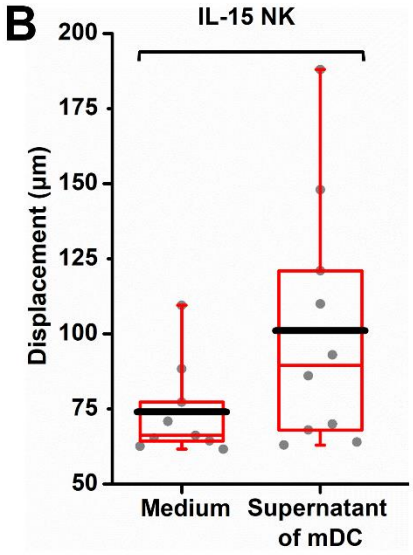

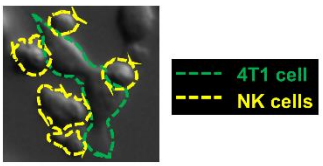

		Contact Time
The 4T1 cell interacted with	5 NK cells	320 sec
	4 NK cells	360 sec
	3 NK cells	1800 sec

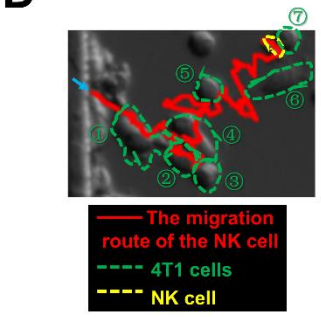

		Begin	Over	Contact Time
The migrated NK cell interacted with	4T1 ①	8 min	8 min 40 sec	40 sec
	4T1 ②	12 min 40 sec	18 min	320 sec
	4T1 ③	16 min 30 sec	16 min 40 sec	10 sec
	4T1 ④	11 min 10 sec	22 min 30 sec	680 sec
	4T1 ⑤	19 min 30 sec	25 min	330 sec
	4T1 ⑥	31 min 10 sec	33 min 10 sec	120 sec
	4T1 ⑦	28 min 30 sec	36 min 10 sec	460 sec

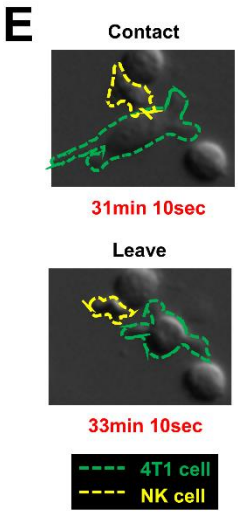

3.4.4 Observation of cell-cell interactions and cell tracking

Detailed information of the interactions between 4T1 and the activated NK cells can be further extracted from the time-lapse images. The migration paths of the activated NK cells were tracked by the cell tracking plug-in in NIH ImageJ. In one scenario, we observed multiple NK cells interacted with one 4T1 cell (**Figure 3.2C**). Some of them had firm interactions with the 4T1 cell, and their contact can last for up to 30 min; others had transient interactions with the 4T1 cell, and "left" the 4T1 cells after a few minutes of cell-cell interactions. In another scenario, one NK cell interacted with multiple 4T1 cells during its migration (**Figure 3.2D**). Some interactions can last for a few minutes while others were only a few seconds. In most circumstances, the shape of 4T1 cells continuously changed during the interaction with NK cells, and in some cases significantly "shrunk" after contacting NK cells (**Figure 3.2E**).

3.5 Discussion

Here we reported the application of the D^3-Chip in the live-cell imaging of directed NK-cell migrations and NK-4T1 tumor cell interactions in the controlled gradient environments *in vitro*. As a proof-of-principle study, we demonstrated that feasibility of studying the number and contact time of NK cells interacting with a cancer cell (**Figure 3.2C**), the tracking of the migration path and contact time of an individual NK cell (**Figure 3.2D**), and the change in cancer cell morphology at the end of the NK-cell interaction (**Figure 3.2E**). This microfluidic based approach will therefore support quantitative analyses and comparative studies of different NK cell preparations under a defined chemical gradient (such as conditioned medium from LPS activated mature DC), or conditions that mimic tumor cell microenvironment. This platform will therefore be useful in further our understanding NK-cell migratory properties and tumor cell interactions under different experimental conditions (such as detailed comparisons of different cytokine-activated NK cells, and/or conditioned medium from cancer cells at different time-points). In addition, we observed that conditioned medium from LPS-activated DC promoted activated NK cell migrations toward 4T1 cancer cells (**Figure 3.2A and B**). The latter may suggest the beneficial effect of activating DC at tumor site to promote NK-cell recruitment and its antitumor activity. In future, such microfluidic device could be further

modified to mimic the better complex *in-vivo* microenvironment [46] to support more advanced investigations of NK-cell migratory responses under physiologically or pathologically relevant conditions.

Chapter 4: Investigations on T cell transmigration in a human skin-on-chip (SoC) model

This chapter is written based on my publication: "**Xiaoou Ren**, Anthony E. Getschman, Samuel Hwang, Brian F. Volkman, Thomas Klonisch, David Levin, Min Zhao, Susy Santos, Song Liu, Jasmine Cheng and Francis Lin. *Investigations on T cell transmigration in a human skin-on-chip (SoC) model*. ***Lab on a Chip*** **(IF: 6.774)**, **2021**. DOI: 10.1039/d0lc01194k.

The study in this chapter was completed in the last stage of my PhD study based our collaboration with the local hospital (i.e., the Victoria General Hospital) and other labs (i.e., Dr. Klonisch' lab at Department of Human Anatomy and Cell Science, University of Manitoba; Dr. Liu's lab at Department of Biosystems Engineering, University of Manitoba; Dr. Volkman's lab at Department of Biochemistry, Medical College of Wisconsin; Dr. Hwang's lab at Department of Dermatology, University of California Davis School of Medicine). Specifically, I performed all the experiments and data analysis, and I wrote the first draft and participated in all the revisions until its final publication.

Developing specific organ-on-chip (OoC) approach that composed of the key features (e.g., physical structure and chemical environment) of target tissues or organs in a microfluidic device for T cell migration study is one of the most important goal during my PhD study. Although the former two chapters (i.e., Chapters 2-3) successfully applied OoC related approaches to investigate the migratory responses of immune cells, their limitations on the model complexity especially the lack of physical structure of certain tissues or organs still exist. To overcome this issue, we tried various strategies and finally developed a skin-on-chip (SoC) model by using multi-cell and ECM co-culture in a micropillar device. This SoC model enables the reconstitution of key features of the human skin (i.e., epithelial, dermal, and endothelial components) and generation of complex chemical fields (i.e., single or co-existing chemical gradients) for investigating the complex involvement of T cell migration during skin inflammation.

4.1 Overview

T cell migration is a crucial element of the immune response and important for maintaining skin homeostasis. Disruption of normal T cell migration contributes to various skin diseases. The migratory response of T cells is dynamically regulated by specific chemotactic signaling during skin inflammation and facilitates T cell homing to different skin layers. In this study, we developed a novel SoC model that replicates key features and responses of human blood T cells during skin inflammation. The physical structure of the SoC device combines epithelial, dermal, and endothelial components originating from human cell lines and extracellular matrix. The SoC model mimics the in-vivo ratio of different skin layers in a normal human skin and enables the creation of dynamic single or co-existing chemical gradients of relevant chemokines to study the dynamic migratory behaviors of T cells. The SoC model provides a novel platform to dissect complex physiological or pathological responses of T cell migration into multiple processes and to investigate the effects of each individual component (e.g., ECM, cell layer, and chemokines) involved in these processes. Our results showed that CCL20-dependent migration of T cells through a HUVEC cell layer or collagen matrix alone was significantly inhibited in the presence of a uniform background of CCL20 locked dimer (CCL20LD). This suggests a potential immunotherapeutic use of CCL20LD as a drug for CCR6-mediated skin diseases and reveals the capability of our system to serve as an effective and robust drug screening device. The ability of T cells to migrate from a CCL20 wild-type (CCL20WT) gradient towards a CXCL12 gradient through a HaCaT cell layer or collagen matrix was significantly reduced in the presence of a uniform S1P background. These results demonstrate the importance of S1P for T cell retention in the inflamed tissues. In our SoC model, the *in-vivo* skin inflammation was replicated by stimulating HaCaT cells with the inflammatory cytokine TNF-α. Collectively, our SoC model recreates a dynamic multi-cellular micro-environment that enables us to track and quantify T cell migration at a single cell level in response to physiological cutaneous inflammatory mediators and potential drugs.

4.2 Introduction

T cell migration is a critical process that plays an essential great role in immune responses

[94]. The migratory behavior of T cells is induced by specific chemokines through multiple chemotactic signaling transduction pathways. The chemotactic T cell responses enable rapid cell movement through a complex physiological environment to effect rapid and direct immune surveillance toward foreign antigenic challenge at inflammatory sites [4,19,21,136-138]. Upon activation, T cell migration from the lymph nodes to inflammatory skin sites via the bloodstream is controlled by multiple interactions between different "homing" receptors and their respective ligands [139]. Detailed studies have demonstrated that T cell migration is involved in the psoriatic pathogenesis, and can modulate the extent of psoriatic inflammatory processes [140,141]. T cell migration is also closely associated with other various skin diseases, including vitiligo, atopic dermatitis, and alopecia areata [142-144]. Collectively, T cell migration is important for maintaining skin homeostasis with high relevance to skin diseases.

Human skin is the largest organ of the human body, provides a vital protective barrier function and consists of the three major layers: outermost epidermis, dermis, and hypodermis (**Figure 4.1A**) [145-147]. The epidermis contains keratinocytes at various stages of differentiation with a regenerative stratum adjacent to the basement membrane, which separates the epidermal from the dermal layer. Dermis and hypodermis consist of fibroblasts that synthesize extracellular matrix (ECM), of which collagen is the most abundant component, to maintain the structural integrity of the tissue and vascular networks [147,148]. Skin inflammatory processes trigger T cells trafficking to regional lymph nodes and this involves down-regulation of the C-C motif chemokine receptor 7 (CCR7)/ C-C motif chemokine ligand 21 and 19 (CCL21/19) axis. In contrast, the C-C motif chemokine receptor 6 (CCR6)/ C-C motif chemokine ligand 20 (CCL20) system is up-regulated in the dermis and epidermis and this facilitates T cell homing to the inflammatory site [8]. In psoriatic skin lesions, CCR6/ CCL20 signaling facilitates inflammatory processes by promoting the migration and accumulation of T cells at psoriasiform sites. This CCR6-mediated T cell migration can be inhibited by an engineered CCL20 locked dimer (CCL20LD) [149]. Other studies reported the C-X-C motif chemokine receptor 4 (CXCR4)/ C-X-C motif chemokine ligand 12 (CXCL12) (i.e., stromal cell-derived factor-1 alpha (SDF-1α)) ligand-receptor system being up-regulated during skin inflammation and contributing to inflammatory angiogenesis [150-152]. In

addition, the up-regulation of the sphingosine-1-phosphate receptor 1 (S1PR1)/ Sphingosine-1-phosphate (S1P) axis in inflamed peripheral tissues, including skin and blood vessels, and the high expression of S1P at the inflammatory sites has been linked to T cell retention at these sites [153]. Hence, the regulation of T cell trafficking in the skin is orchestrated by complex mechanisms controlled by chemical fields that are subject to dynamic changes during inflammation (**Figure 4.1B-C**).

Figure 4. 1 Illustration of the inflamed human skin, T cell transmigration in inflamed human skin, and T cell transmigration in different chemokine fields in the skin-on-chip (SoC) model.

(A) Schematic illustration of basic histological structure of the human skin. **(B)** Illustration of transmigration of blood-derived T cells during skin inflammation. **(C)** Schematic illustration of the effects of different chemokine fields on T cell transmigration in the SoC model.

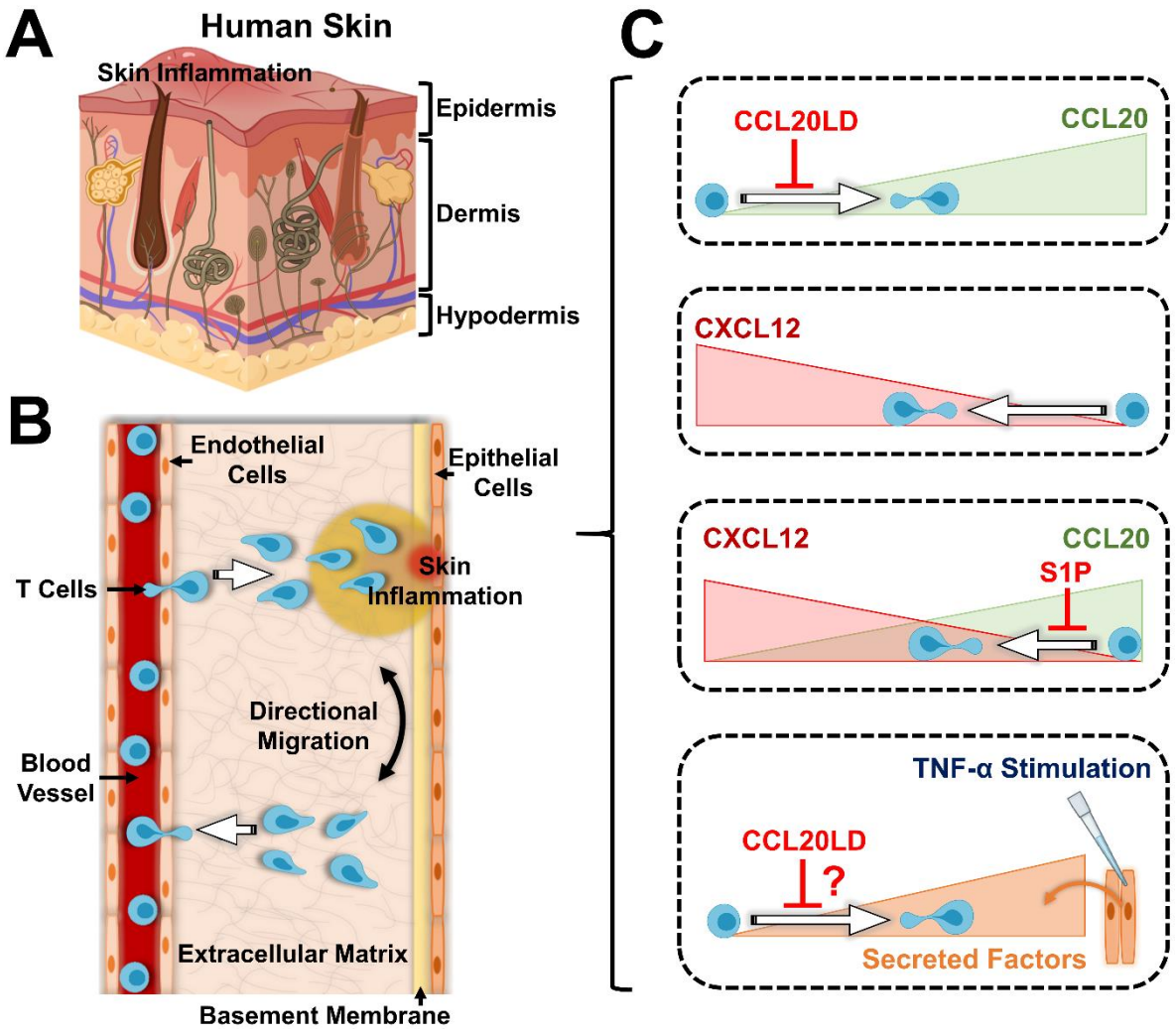

Microfluidic devices provide an advanced platform to mimic physiological conditions for biological and biomedical research and this field of research has been fast growing in recent years [38,39]. This technology is well suited for cell migration studies owing to key advantages of microfluidics, such as miniaturization, precise and flexible chemical gradient generation, low reagent consumption, and high-throughput experimentation [40-43]. Despite these advantages, the majority of microfluidic devices used for cell migration studies suffer from several limitations. These drawbacks include the reconstitution of much-simplified stable chemical fields, ECM, and single cell type based microenvironments, which do not reflect the complex *in-vivo* microenvironment cells encounter during their tissue migration [1]. The OoC microfluidic devices are an attractive new modification which structurally integrate cell co-culture strategies in the microfluidics design to better simulate the key activities and responses of certain tissues or organs [1]. Among them are "liver-on-a-chip", "kidney-on-a-chip", "muscle-on-a-chip", and "lymph node-on-a-chip" [62,154-157]. A recent study demonstrated the feasibility of constructing a mimetic "skin-on-chip" (SoC) model *in vitro*, which was used for drug toxicity testing and disease studies [51]. However, no study has applied a SoC model for T cell migration studies. This motivated us to develop such an approach for investigating cutaneous T cell migration in a reconstituted *in-vivo* microenvironment based on a microfluidic device specifically designed for this purpose.

In this study, we have developed a novel microfluidic SoC model (**Figure 4.2**) that resembles key features of the human skin. For the first time, we used this SoC model to study T cell migratory responses towards the effects of controlled complex chemical gradients simulating cutaneous inflammation. Our microfluidic device (**Figure 4.2A**) enabled performance measurements of four parallel cell migration experiments simultaneously conducted by four identical independent units, each independently controlling gradient generation. This SoC model was compatible with different immune cell types, including activated human peripheral blood T cells (ahPBTs) and human blood neutrophils. Each unit consists of one gel channel, with one gel inlet (1 mm diameter) and one gel well (3 mm diameter) flanked by two side channels with two chemical inlets (1 mm diameter) and two chemical wells (6 mm diameter) (**Figure 4.2B**). The smaller sized gel and chemical inlets provide better

sealing when solutions are loaded. The front portion length of the gel channel (5000 μm) is longer than the major compartment (1140 μm) and the back portion (3000 μm) to reduce the initial flow speed of gel solution. Although the method of patterning gel in the device using micropillars is similar to other studies [52,158-160], the number, layout and dimension of the micropillars was designed and modified in a more compact manner (**Figure 4.2C**).

Figure 4. 2 Illustration of the micropillar device and skin-on-chip (SoC) model.

(A) A representative image of the dimensions of the micropillar device. The top transparent part is PDMS and the bottom part is a glass slide. The numbered areas circled with black dashed lines show the four independent units on a single device. **(B)** The magnified view of one selected unit from Figure A shows the major structures in the real device (top image) and schematic diagram (bottom image). **(C)** Schematic illustration of the selected area from Figure B (dashed line) to show the magnified view of the SoC model from a top- and side-view, respectively.

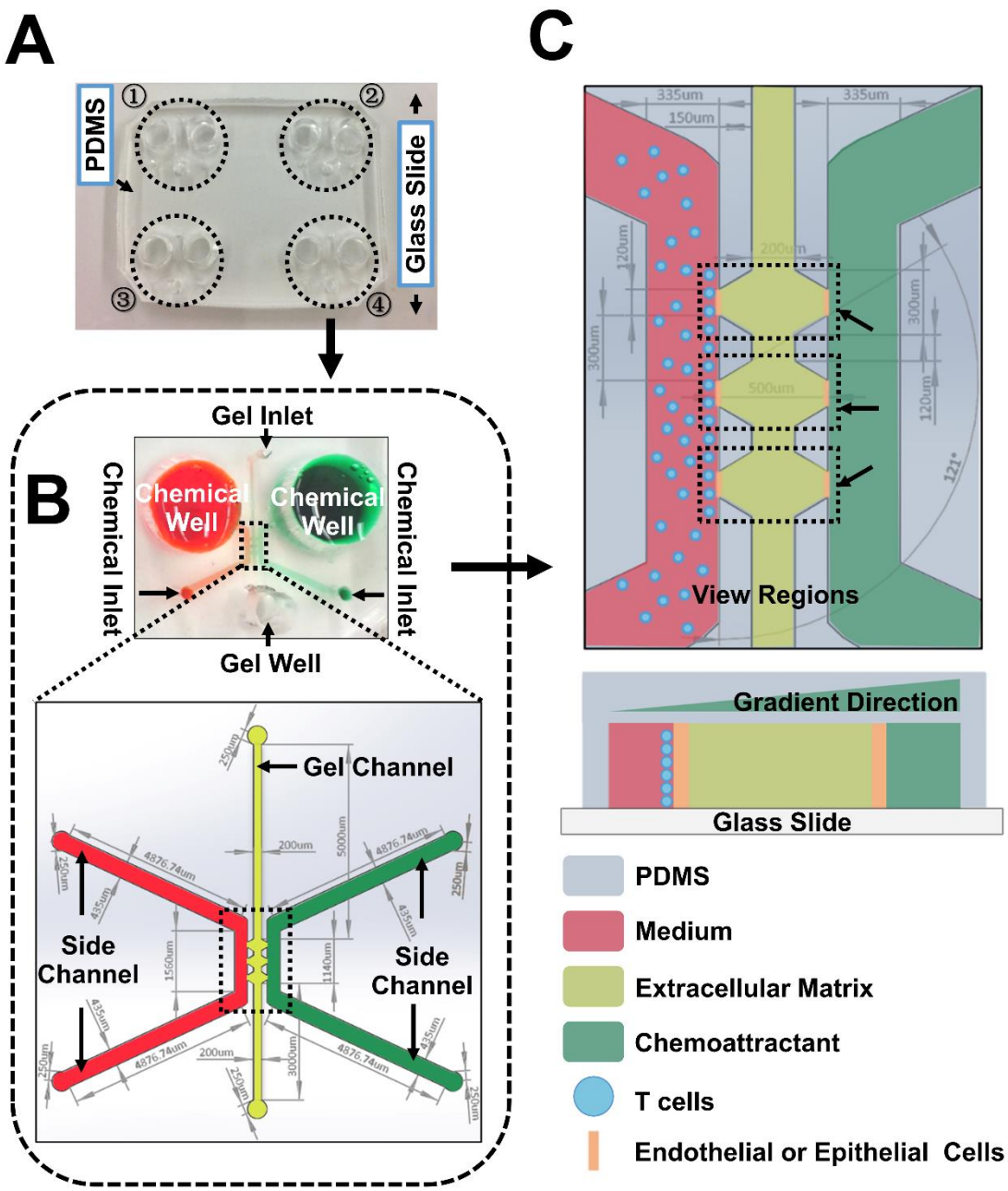

Specifically, the major compartment is divided by four trapezoidal micropillars to provide multiple view regions for the cell migration experiments. The gap (120 μm) between two neighboring micropillars provides enough space to allow sufficient T cells to migrate across the gap simultaneously. The design of micropillars conducted with hydrophobicity restoration of PDMS enabled the selective gel patterning in the major compartment (**Figure 4.3A-B**). Establishment of the HaCaT cell layer, three dimensional (3D) collagen gel with porous fiber structure, and HUVEC cell layer in the device replicated major features of the epithelium, ECM, and endothelium *in vitro* (**Figure 4.3B-D)**. In addition, the ratio of width of the gel compartment (500 μm) to the thickness of a few cell layers of HaCaT (~tens of microns) was designed to reflect the *in-vivo* ratio of dermis to epidermis (approximately 3-60 folds) [161,162]. A single or competing gradient (**Figure 4.3E-F)** of relevant chemokines was generated based on the chemical diffusion from one side channel to the other through the collagen gel to mimic the *in-vivo* chemical fields during skin inflammation. We demonstrated the application of this SoC model for simulating on-chip skin inflammation using tumor necrosis factor-α (TNF-α) stimulation. Furthermore, we used a previously engineered CCL20LD to successfully inhibit CCR6-mediated T cell migration in our SoC model. Our results demonstrate the capability and potential of this SoC model to investigate the role of physiologically relevant chemical fields in mediating cutaneous T cell homing and may serve as a novel drug screening platform to identify compounds targeting skin diseases (e.g., psoriasis).

Figure 4. 3 Illustration of the 3D collagen gel formation, HUVEC/ HaCaT cell patterning, cell displacement analysis, and FITC-Dextran gradient profile plot in the micropillar device.

(A) Representative image showing the 3D collagen gel matrix in the middle gel channel of the device. The black dashed box shows one field of view under the microscope. **(B)** A representative phase-contrast image of the selected field of view region from Figure A shows the ECM filled space upon gelation in the magnified viewing area (scale bar: 100 μm). **(C-D)** Representative DIC and fluorescent images of the selected field of view from Figure A show the 3D gel with HUVEC/ HaCaT cell patterning in the device. The white dashed box shows the 3D collagen gel with adherent HUVEC (left side) and HaCaT cells (right side) in Figure C; the red and blue colored dots indicate the HUVEC and HaCaT cells, respectively, attached to both sides of the 3D collagen gel in Figure D. **(E)** A representative fluorescent image of the selected field of view region from Figure A illustrates cell migration displacement analysis (scale bar: 100 μm). The red colored dots indicate labeled T cells, and the green color in the channel indicates the profile and most concentrated area of the chemical gradient. **(F)** Representative fluorescence intensity plot displaying the chemical gradient at 1 hour (1h) of experimentation in this device.

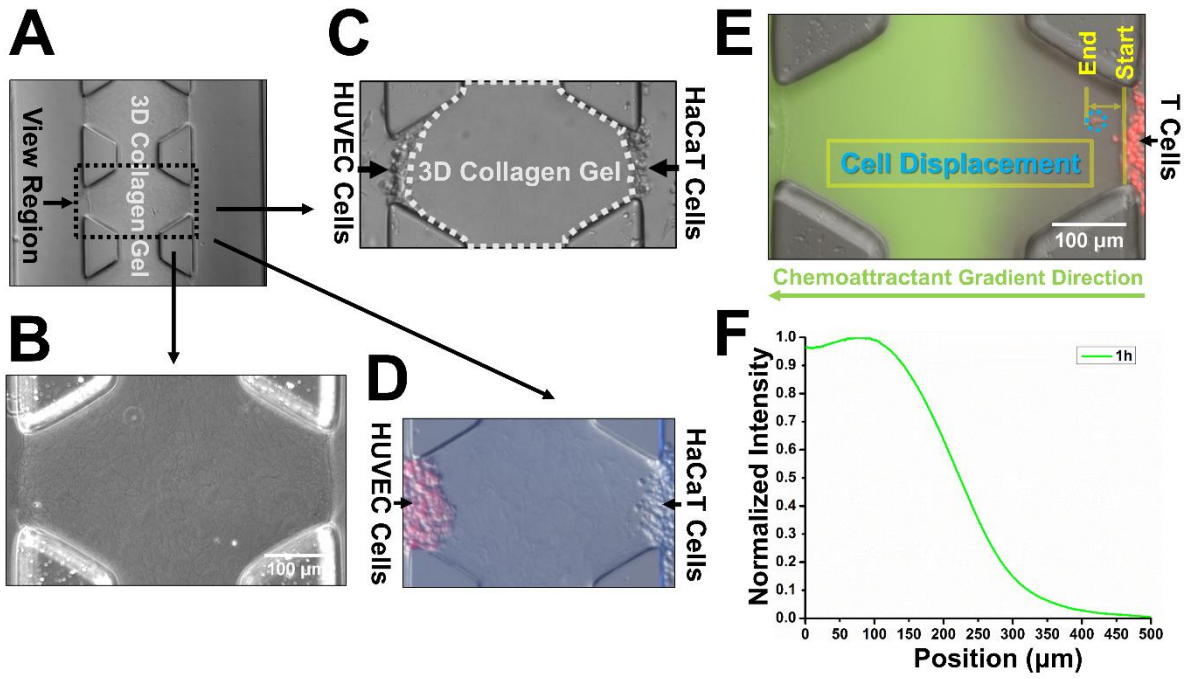

4.3 Materials and methods

4.3.1 Collection of blood samples

An ethics protocol (J2015:022) was approved by the Joint-Faculty Research Ethics Board at the University of Manitoba for collecting blood samples from healthy human donors. All the participants were recruited at the Victoria General Hospital (Winnipeg, Manitoba, Canada) according to the approved procedures. Specifically, each participant reviewed a consent form in detail and discussed any concerns or questions with the recruiting staff prior to consenting. Peripheral blood samples were then collected from these consented healthy donors at the hospital.

4.3.2 Preparation of activated human peripheral blood T cells

Human peripheral blood samples were obtained from healthy donors according to the mentioned procedures. A standard gradient centrifugation method was conducted for isolating peripheral blood mononuclear cells (PBMCs) from the blood samples. T cells within the PBMCs were selectively activated by adding anti-human CD3 (Purified anti-human CD3 Antibody, BioLegend, catalog# 300302) and anti-human CD28 (Purified anti-human CD28 Antibody, BioLegend, catalog# 302901) antibodies at a final concentration of 1 μg/ml for each in complete RPMI-1640 culture medium (RPMI-1640 with 1% penicillin-streptomycin and 10% FBS) for 2 days inside an incubator (37 °C, 5% CO_2). The ahPBTs proliferated in the same culture medium with a supplement of 12.5 ng/ml of interleukin-2 (IL-2) (R&D Systems) for at least 3 days before the start of the cell migration experiments [21,40,163]. The purity of activated T cells is more than 91%, which has been confirmed previously by flow cytometry [40,105].

4.3.3 Preparation of human blood neutrophils

Human blood neutrophils were isolated from the peripheral blood samples of healthy donors using a magnetic negative selection kit (EasySep Direct Human Neutrophil Isolation Kit, STEMCELL). The highly purified neutrophils were cultured in the complete RPMI-1640

culture medium (RPMI-1640 with 1% penicillin-streptomycin and 10% FBS) in an incubator (37°C, 5% CO_2) and used for cell migration experiments within 8 h of isolation. Neutrophils were re-suspended in the same culture medium when loading into the device.

4.3.4 Cell culture

Human immortalized keratinocytes (HaCaT) were provided by Dr. Song Liu through his collaboration with Dr. Aziz Ghahary at the University of British Columbia. Human umbilical vein endothelial cells (HUVEC) were provided by Dr. Min Zhao purchased from ATCC. HaCaT and HUVEC cells were used as substitutes to represent cellular components of the epithelium and blood vessel compartment in the skin, respectively [51]. HaCaT and HUVEC cells were cultured in complete DME/F12 culture medium (DME/F12 with 1% penicillin-streptomycin and 10% FBS) in an incubator (37 °C, 5% CO_2) prior cell migration experiments.

4.3.5 Cell labeling

The CellTracker™ fluorescent probes Orange CMRA Dye (C34551) and Violet BMQC Dye (C10094) (both Molecular Probes, Invitrogen) were used to label cells and to demonstrate the positions of the labelled cells. Cell labeling was conducted according to the manufacturer's protocol. Cells were collected from the culture medium and incubated with pre-warmed (37 °C) CellTracker™ working solution (0.5 μM) in serum-free medium for 45 minutes inside an incubator (37 °C, 5% CO_2). The labelled cells were then extracted from the CellTracker™ working solution and re-suspended in the culture medium before cell migration experiments.

4.3.6 Fabrication of the microfluidic device

The device pattern was designed in SolidWorks® (ver. 2012, Dassault Systems S.A.), and fabricated on a three inch silicon wafer (Silicon, Inc., ID) using standard photolithography methods [163-165] . The fabrication process and dimension measurements were conducted in our lab at the Department of Physics and Astronomy and the Nano Systems Fabrication Laboratory at the University of Manitoba, respectively. Briefly, the designed pattern was printed onto a transparent film at 24,000 dpi resolution (Fineline Imaging, Colorado Springs, CO) and replicated onto a silicon wafer with pre-coated SU-8 negative photoresist (MicroChem

Corporation, Westborough, MA) using selective ultraviolet exposure of the film. The patterned wafer served as the mold to reproduce polydimethylsiloxane (PDMS) (Sylgard 184, Dow Corning, Manufacturer SKU# 2065622) replicas using standard soft-lithography methods [163-165]. Specifically, the PDMS working solution was prepared by mixing PDMS and its curing agent at the ratio of 10: 1 (w/w), followed by pouring the solution into the mold. The PDMS replica was cut off from the mold after 2h of baking at 80 °C in an oven. The gel inlet, gel well, chemical inlets, and chemical wells were punched out of the PDMS replica, followed by bonding the replica onto a glass slide using an air plasma cleaner (Harrick Plasma, Ithaca, NY).

4.3.7 Preparations of ECM and cell layers in the device

The device was baked in the oven overnight to restore the hydrophobicity before gel loading. This process has been commonly applied by others to prevent gel leakage [52,158,160]. As collagen is the most abundant component in the human dermal ECM [147,148], RatCol® Rat Tail Collagen Kit (catalog# 5153, Advanced BioMatrix, San Diego, CA) was used as 3D hydrogels to mimic the *in-vivo* ECM with porous fiber structure [166,167]. Type I rat tail collagen solution (3.8 mg/ml) from the kit was gently mixed with its neutralization solution at the ratio of 9: 1 (v/v) according to the manufacturer's protocol, followed by a second dilution step with phosphate buffer saline (PBS, 1×) at the ratio of 1: 1 (v/v) in a pre-cooled (-20 °C) Eppendorf tube. The diluted mixture was injected into the gel inlet to fully fill the gel channel, and the gel well was filled up. All the procedures including 3D collagen gel preparation and injection were conducted on ice to prevent uncontrolled gelation. The device was then placed in the incubator for 30 minutes of gelation. The porous fiber structure of the 3D collagen gel was visualized in the gel channel, without any leakage occurring to the side channels (**Figure 4.3B**). For surface coating, collagen at 20 μg/mL was gently injected from the chemical inlets to fully fill the chemical channel and the device was incubated for 1h in the incubator. Upon removal of the coating solution, each chemical well was injected with complete DME/F-12 culture medium, and the device was transferred to the incubator for 30 minutes before the medium inside the chemical wells was discarded. HaCaT and HUVEC cell solutions (1×10^5 cells in 100 μL/well) were loaded into the chemical wells drop by drop and

the device was returned to the incubator to allow the attachments of HaCaT and HUVEC cells to both sides of the collagen gel. HaCaT and HUVEC cell layers had formed after 2h of incubation (**Figure 4.3C-D**). The device was kept inside the incubator overnight prior to cell migration experiments. The device was placed inside a humidified chamber (i.e., a pipette tip box with damp tissues on the rack and small volumes of deionized water in the bottom chamber) during all incubation procedures to prevent drying of samples. When testing cell migration with collagen gel alone, the identical procedure was conducted, but with the omission of loading HaCaT and HUVEC cells, and the device was incubated with complete DME/F-12 culture medium in the incubator overnight. On-chip stimulation with TNF-α used the same procedure but the incubation time with HaCaT and HUVEC cells was 2h and the medium was discarded from the chemical wells before treatment.

4.3.8 Preparation of the chemoattractants

Complete DME/F-12 culture medium was used to culture HaCaT and HUVEC cells and served as medium control and diluent. CXCL12 at the concentration of 100 ng/mL [163] was used as positive control in the experiments involving migration of T cells through the HaCaT/ collagen gel layers. CCL20WT was synthesized as previously described [149] and prepared at a concentration of 100 ng/mL as positive control for those experiments that investigated T cell migration through HUVEC/ collagen gel layers. In some experiments, a competing CCL20WT/ CXCL12 gradient with or without a uniform background of 100 ng/mL of S1P was generated to test migration of T cells through the HaCaT/ collagen gel layers in the SoC device. A previously engineered CCL20LD [149] was prepared at concentrations of 100 ng/mL and 1.6 μg/mL and used as an inhibitor to CCR6-mediated T cell migration. For neutrophil migration experiments, two different experimental groups, fMLP (N-formylmethionyl-leucyl-phenylalanine; 100nM) in complete RPMI-1640 culture medium and medium control, were tested in parallel on each device following the same experimental protocol and data analysis method for T cells.

4.3.9 TNF-α induced skin inflammation in the device

The well-known inflammatory mediator TNF-α was prepared at the concentration of 100

ng/mL to simulate skin inflammation *in vitro* in the microfluidic device [51]. TNF-α solution (100 μL) and complete DME/F-12 culture medium (100 μL) were injected in the chemical well at the HaCaT and HUVEC side, respectively, for overnight incubation. The next day, supernatants from the chemical well at the HUVEC side were discarded, whereas the supernatants from the chemical well at the HaCaT side were collected. Any remaining HaCaT cells in the supernatants were removed by centrifugation prior to using these supernatants as chemoattractant solutions for the T cell migration experiments. The chemical wells were incubated with complete DME/F-12 culture medium (100 μL/well) in the incubator before commencing cell migration experiments.

4.3.10 Setup of the cell migration experiments

Prior to the start of cell migration experiments, complete DME/F-12 culture medium remaining in the chemical wells was discarded. The ahPBTs were extracted and re-suspended in complete DME/F-12 culture medium before loading into the device. Fluorescein isothiocyanate (FITC)-dextran (10 kDa, final concentration of 5 μM, Sigma-Aldrich, Catalog# FD10S) was added into all the chemoattractant solutions (e.g., CXCL12, CCL20WT, CCL20LD, and supernatants), except the competing gradient experiments, to characterize the chemical gradient in real time [163,164]. One chemical well was loaded with T cells (1×10^5 cells in 100 μL) first and T cells were allowed to attach to the collagen gel or HaCaT/ HUVEC cell layers for several minutes. This was followed by loading the chemoattractant solution (100 μL) into the other chemical well to generate the chemical gradient. All loading procedures were conducted drop by drop to prevent damage to the collagen gel. The loaded device was placed on a movable stage under an inverted fluorescence microscope (Nikon Ti-U) inside an environmental controlled chamber (InVivo Scientific) at 37 °C during the experiment. Differential interference contrast (DIC) images during cell migration experiments were taken at multiple positions at 0h, 0.5h and 1h, respectively, for each device. When not taking images, the device was incubated inside the humidified chamber in the incubator.

4.3.11 Data analysis

All experimental conditions were independently replicated at least three times. The DIC

images of cell migration were extracted from the NIS Element Viewer (Nikon) and analyzed with ImageJ software (NIH). Cells that transmigrated through the collagen gel and/or HaCaT/ HUVEC cell layers from the boundary towards the most concentrated area of the gradient inside the channel were recorded within the microscopic field of view. The directional cell migration displacement (**Figure 4.3E**) towards the gradient direction was recorded for individual T cells during the experiment. The OriginPro software was used for statistical analysis of the data presented in the Box Chart. Two-sample Student's t-test was conducted to compare different conditions, and *$p < 0.05$, **$p < 0.01$ and ***$p < 0.001$ were indicated statistically significant difference.

4.4 Results

4.4.1 SoC model validation with CXCL12 induced T cell migration

In order to validate the SoC model and mimic CXCL12 induced T cell migration during skin inflammation, we challenged T cells to transmigrate through the HaCaT layer in the presence of a gradient of CXCL12 (100 ng/mL), with medium serving as the control. Labelled T cells were loaded into the channel to demonstrate the integrity of a leakage-free gel. These experiments excluded possible T cell leakage from the collagen gel at the start of experiment (0h). We showed that 18 fold increase in T cells transmigrating through the HaCaT layer towards the CXCL12 gradient with significantly higher mean cell displacement compared to the medium control, which is consistent with the known CXCL12 effect of inducing T cell chemotaxis (**Figure 4.4**). Considering the clear size and morphology difference between T cells and HUVEC & HaCaT cells, migrating T cells in the collagen gel channel can be easily distinguished without labelling. We tested the migration of T cells through the collagen gel alone (without HaCat layer) under the same conditions (i.e., 100 ng/mL of CXCL12 and medium control) to assess whether absence of a HaCaT layer could affect T cell migratory behavior. Irrespective of the HaCat layer, we found that more than 61 fold increase of T cells transmigrating through the 3D collagen gel layer towards the CXCL12 gradient, with significantly higher mean cell displacement compared to the medium control. Hence, we concluded that T cell migration in the presence of the CXCL12 gradient was not impeded by

the HaCaT layer (**Figure 4.4**). In addition to T cells, the device was validated with human blood neutrophils. Our results showed that a gradient of 100 nM (i.e., 43.76 ng/mL) N-formylmethionyl-leucyl-phenylalanine (fMLP) was able to attract neutrophil chemotaxis through collagen gel, while no neutrophils migrated at all in the medium control (**Figure 4.5**). Our finding is consistent with the literature and our previous results with other microfluidic devices [58,101,134].

Figure 4. 4 CXCL12 induced T cell transmigration in the SoC model.

(A) Representative images of T cell transmigration through a HaCaT cell layer or collagen gel layer alone in the presence of a CXCL12 gradient and medium control conditions in the microfluidic device at 0h, 0.5h, and 1h, respectively (scale bar: 100 μm). The red colored dots in the images show the labelled T cells; the green color in the images indicates the profile and most concentrated area of the CXCL12 gradient. **(B)** The displacement analysis of T cells in different experimental groups at 1h from Figure A. The box charts show the total displacement of individual T cells in the corresponding experimental groups in Figure A; the top and bottom of the whisker show the maximum and minimum values; the box includes the migrated T cells within the range from 25% - 75% of total cells based on the ranked displacement value; the black bold line indicates the mean displacement value. The data in different groups were compared using the two sample Student's t-test, significant difference was indicated using *p < 0.05, **p < 0.01, and ***p < 0.001.

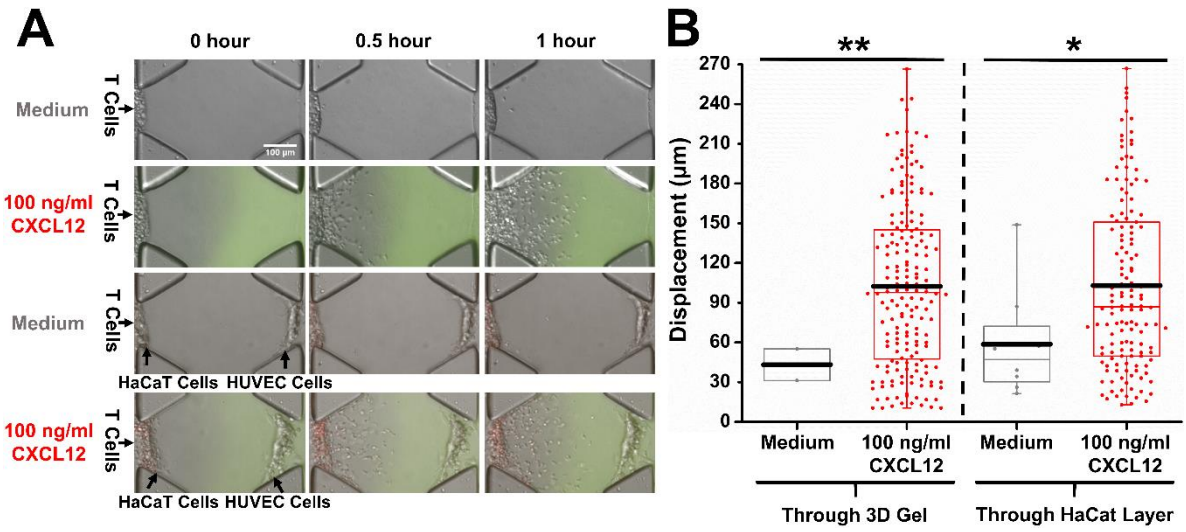

Figure 4. 5 Neutrophil transmigration in the SoC model.

(A) Representative images of neutrophil migration through collagen gel in the medium and fMLP groups in the micropillar device at 0 h and 1 h, respectively (scale bar: 100 μm). The green color in the images indicates the gradient profile and most concentrated area of the fMLP gradient. **(B)** The displacement analysis of neutrophils in the different experimental groups at 1 h from Figure A. The box charts show the total displacement of each human neutrophil in the corresponding experimental groups in Figure A; the interpretation of box chart is the same as previously described. Note that no human neutrophils migrated through collagen gel in the "Medium" group.

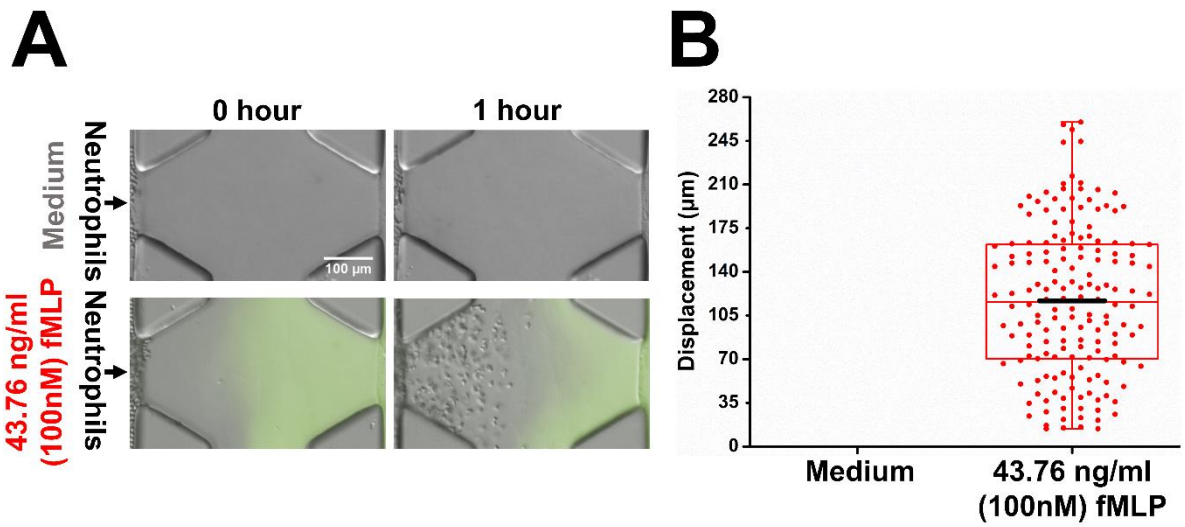

4.4.2 CCL20 induced T cell migration in the SoC model

To mimic the effects of CCL20 induced cutaneous T cell migration during inflammation, we tested the transmigration behavior of human T cells through a HUVEC layer in a gradient of CCL20WT (100 ng/mL) versus medium control. The CCL20WT gradient induced 1.8 fold increase of T cells transmigrating through the HUVEC layer, with higher mean cell displacement compared to the medium control (**Figure 4.6**). We then validated T cell migration in collagen gel alone under the same conditions (i.e., 100 ng/mL of CCL20WT and medium control) and tested whether the absence of a HUVEC layer affects the migratory behavior of the T cells. Our results consistently demonstrated that 33 fold increase in T cells transmigrating through the 3D collagen gel layer towards the CCL20WT gradient with significantly higher mean cell displacement compared to the medium control. In addition, the absence of a HUVEC layer significantly reduced the mean displacement of migrated T cells in the CCL20WT gradient as compared to the presence of a HUVEC layer (**Figure 4.6**).

Figure 4. 6 CCL20 induced T cell transmigration in the SoC model.

(A) Representative images of T cell transmigration through a HUVEC cell layer or collagen gel layer alone in a CCL20WT gradient and medium control in the microfluidic device at 0h, 0.5h, and 1h, respectively (scale bar: 100 μm). The green color in the images indicates the profile and most concentrated area of CCL20WT gradient. Note that the images of T cell migration through the collagen gel layer in medium control (i.e., the first row of three images) is the same set of experiment shown in Figure 4.4A. **(B)** The displacement analysis of T cells in different experimental groups is shown at 1h from Figure A. The box charts show the total displacement of individual T cells in the corresponding experimental groups in Figure A; the interpretation of box chart is the same as previously described. The data in different groups were compared using the two sample Student's t-test, significant difference was indicated using *p < 0.05, **p < 0.01, and ***p < 0.001.

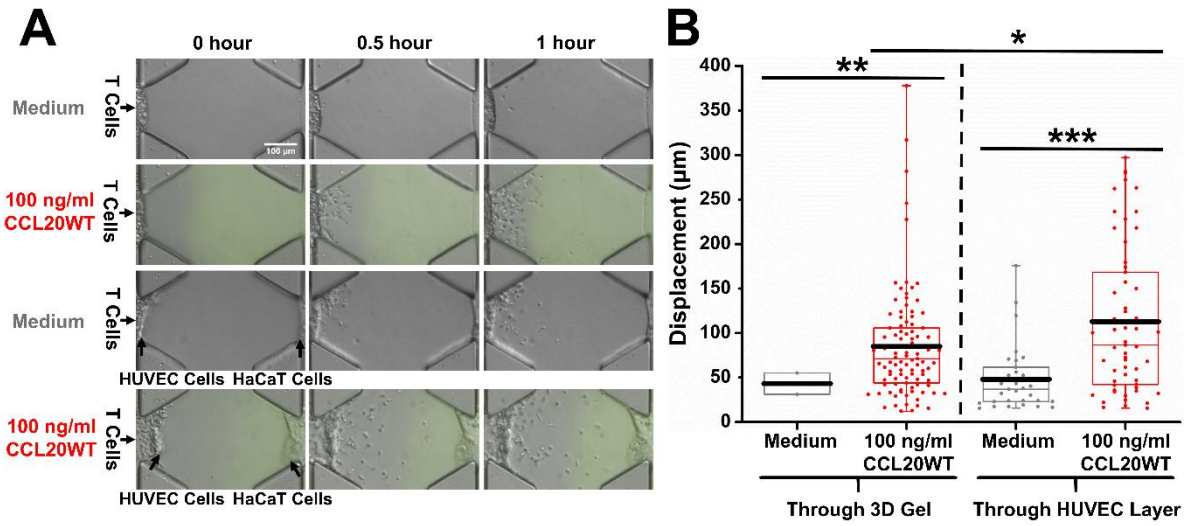

4.4.3 Effects of co-existing chemokine fields on T cell migration in the SoC model

S1P has been reported to be highly expressed in the skin and blood vessels during cutaneous inflammation [153]. Using a previously designed radial microfluidic device [165], we performed a quantitative analysis of T cell migration and chemotaxis in medium control and a gradient of S1P at different concentrations in 2D condition. The results obtained from the radial microfluidic device showed that S1P significantly induced T cell chemotaxis at the concentrations of 100 nM (i.e., 37.95 ng/mL), 200 nM (i.e., 75.90 ng/mL), 300 nM (i.e., 113.85 ng/mL) and 500 nM (i.e., 189.75 ng/mL) compared to medium control, with the highest number of migrated T cells at 200 nM and the highest mean cell displacement at 300 nM (**Figure A.1**). Thus, we used the range from 200 to 300 nM of S1P as a reference and 100 ng/mL of S1P for cell migration experiments in the SoC model. Skin inflammation requires T cells to navigate a complex chemical cutaneous environment. To determine whether our SoC model can replicate such challenging conditions, we decided to devise an experiment to investigate T cell migration in a microenvironment of competing chemokine gradients. Specifically, gradients of CXCL12 (100 ng/mL) and CCL20WT (100 ng/mL) were generated at the HUVEC side and HaCaT side, respectively, with or without a uniform S1P (100 ng/mL) background, to mimic the complex chemical environment during skin inflammation. We quantified the impact of these SoC conditions for T cell migration. Our results demonstrated the importance of S1P for the outcome of these experiments. Fourteen percent less of T cells transmigrated through the HaCaT layer towards the CXCL12 gradient with significantly lower mean cell displacement in the presence of a uniform S1P background as compared to the absence of S1P (**Figure 4.7**). We further investigated T cell migration in the collagen gel alone under the same conditions (i.e., CXCL12 gradient at the HUVEC side and CCL20WT gradient at HaCaT side, with and without uniform S1P background) and tested whether the absence of a HaCaT layer could affect T cell migratory behavior. Again, one quarter of T cells transmigrated through collagen gel layer towards the CXCL12 gradient with significantly lower mean cell displacement in the presence of a uniform S1P background as compared to a lack of S1P background. Moreover, the absence of the HaCaT layer resulted in fewer T cells transmigrating towards the CXCL12 gradient and

significantly lower mean cell displacement in the same competing gradients with or without S1P when compared to the HaCaT layer being present (**Figure 4.7**).

Figure 4. 7 The retention effect of S1P on T cell migration in co-existing chemokine fields in the SoC model.

(A) Representative images of T cell transmigration through a HaCaT cell layer or collagen gel layer alone in different competing gradient groups in the microfluidic device at 0h, 0.5h, and 1h, respectively (scale bar: 100 μm). **(B)** The displacement analysis of T cells in different experimental groups at 1h from Figure A. The box charts show the total displacement of individual T cells in the corresponding experimental groups in Figure A; the interpretation of box chart is the same as previously described. The data in different groups were compared using the two sample Student's t-test, significant difference was indicated using *p < 0.05, **p < 0.01, and ***p < 0.001.

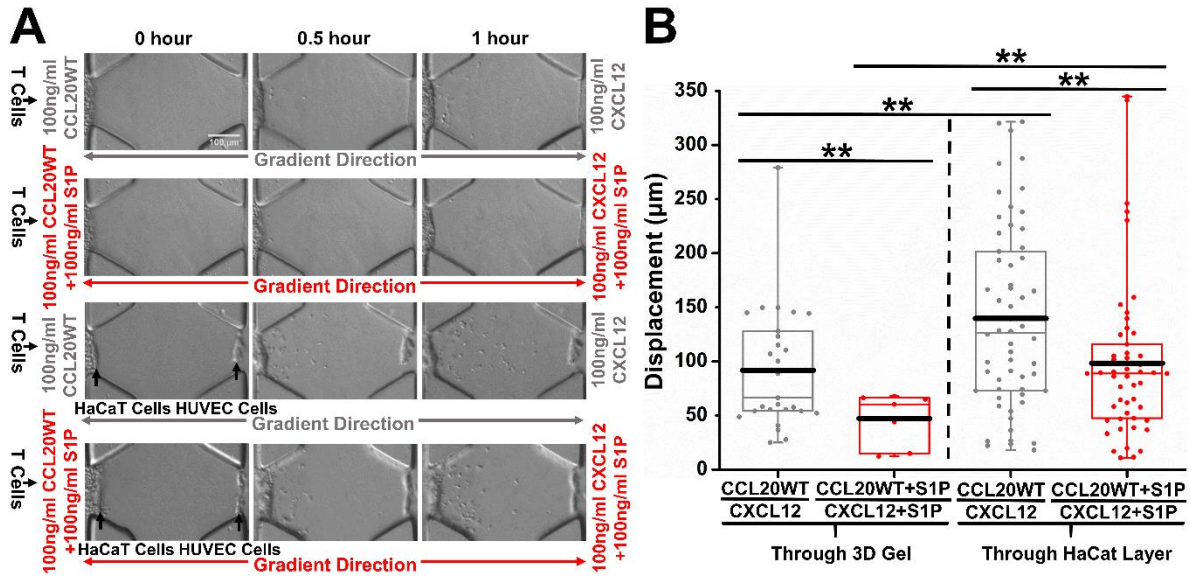

4.4.4 CCL20LD inhibits T cell migration in the SoC model

In cell based assays, CCL20LD is an effective inhibitor of CCR6-mediated cell migration and can prophylactically inhibit T cell-associated skin inflammation in animal models of psoriasis [149]. We wanted to test whether CCL20LD can disrupt CCR6/CCL20 receptor-ligand interaction and negatively affect T cell migration in our SoC model. We first examined T cell transmigration through a HUVEC layer in a gradient of CCL20LD (100 ng/mL) or a gradient of CCL20WT (100 ng/mL) with a coexisting uniform CCL20LD (1.6 μg/mL). Results were compared with those of T cell migration in a gradient of CCL20WT (100 ng/mL) or medium control in the SoC model. Around 2 fold increase of T cells transmigrating through the HUVEC layer in the CCL20WT gradient, with significantly higher mean cell displacement when compared to both CCL20LD and medium control conditions. This CCL20WT induced T cell migration was significantly muted by a coexisting uniform CCL20LD background and resulted in less than half of T cells transmigrating through the HUVEC layer and significantly lower mean cell displacement (**Figure 4.8**). To investigate this further, we studied the CCL20LD inhibitory effect on CCR6-mediated T cell migration in collagen gel alone under the same conditions to test whether the absence of the HUVEC layer can alter the T cell migratory response. Consistently, the CCL20WT gradient attracted 4 fold and 33 fold the number of T cells through the collagen gel layer compared to the CCL20LD gradient and medium control, respectively. This migratory response was completely blocked in the presence of a coexisting uniform CCL20LD. Under the same conditions, the absence of HUVEC layer did not significantly affect T cell migration except for the CCL20WT group, which showed fewer migrated T cells with significantly reduced mean cell displacement when compared to the presence of a HUVEC layer (**Figure 4.8**).

Figure 4. 8 The inhibitory effect of CCL20LD on T cell transmigration in the SoC model.

(A) Representative images of T cell transmigration through a HUVEC cell layer or collagen gel layer alone in different groups in the microfluidic device at 0h, 0.5h, and 1h, respectively (scale bar: 100 μm). The green color in the images indicates the profile and most concentrated area of each gradient. Note that the images of T cell migration in CCL20WT gradient (i.e., the first and fourth rows of the images) are the same sets of experiments shown in Figure 4.6A. **(B)** The displacement analysis of T cells in different experimental groups at 1h from Figure A. Note that the data in the "Medium" and "CCL20WT" groups used for comparison were from the same set of experiments shown in Figure 4.6B. The colored box charts show the total displacement of individual T cells in the corresponding experimental groups in Figure A; the interpretation of box chart is the same as previously described. Note that no T cells transmigrated through the collagen gel layer in the "CCL20WT+Uniform CCL20LD" group. The data in different groups were compared using the two sample Student's t-test, significant difference was indicated using *p < 0.05, **p < 0.01, and ***p < 0.001.

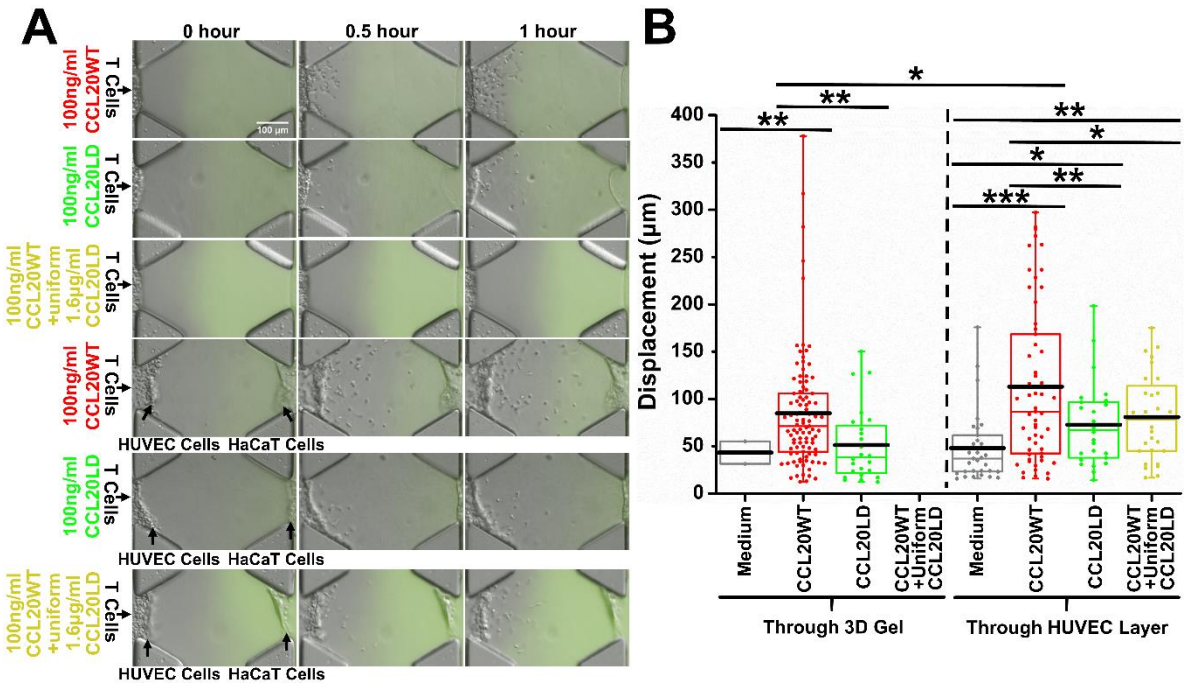

4.4.5 TNF-α induced cutaneous inflammation in the SoC model

We wanted to examine whether TNF-α stimulation can be used to reconstitute skin inflammation *in vitro* in our SoC model. First, TNF-α stimulation was conducted in the SoC model and, upon stimulation, supernatants were collected as described in the method section. T cell transmigration though a HUVEC layer was tested in a gradient of collected supernatants with or without a coexisting gradient of CCL20LD (100 ng/mL) applied in the same direction and all results were compared to the medium control. T cell transmigration through the HUVEC layer towards the gradient of supernatants was significantly enhanced, with one-third more migrated T cells showing significantly higher mean cell displacement compared to medium control (**Figure 4.9**). This positive effect of the supernatants on T cell migration was not significantly reduced in the presence of a coexisting gradient of CCL20LD in the SoC model (**Figure 4.9**).

Figure 4. 9 Supernatants from on-chip TNF-α stimulated HaCaT cells induce T cell transmigration in the SoC model.

(A) Representative images of T cell transmigration through a HUVEC cell layer in the medium control and two supernatants groups in the SoC model at 0h, 0.5h, and 1h, respectively (scale bar: 100 μm). The green color in the images indicates the profile and most concentrated area of the gradient. Note that the images of T cell migration in medium control (i.e., the first row of three images) is the same set of experiments shown in Figure 4.6A. **(B)** The displacement analysis of T cells in different experimental groups at 1h from Figure A. The colored box charts show the total displacement of individual T cells in the corresponding experimental groups in Figure A; the interpretation of box chart is the same as previously described. The data in different groups were compared using the two sample Student's t-test, significant difference was indicated using *p < 0.05, **p < 0.01, and ***p < 0.001.

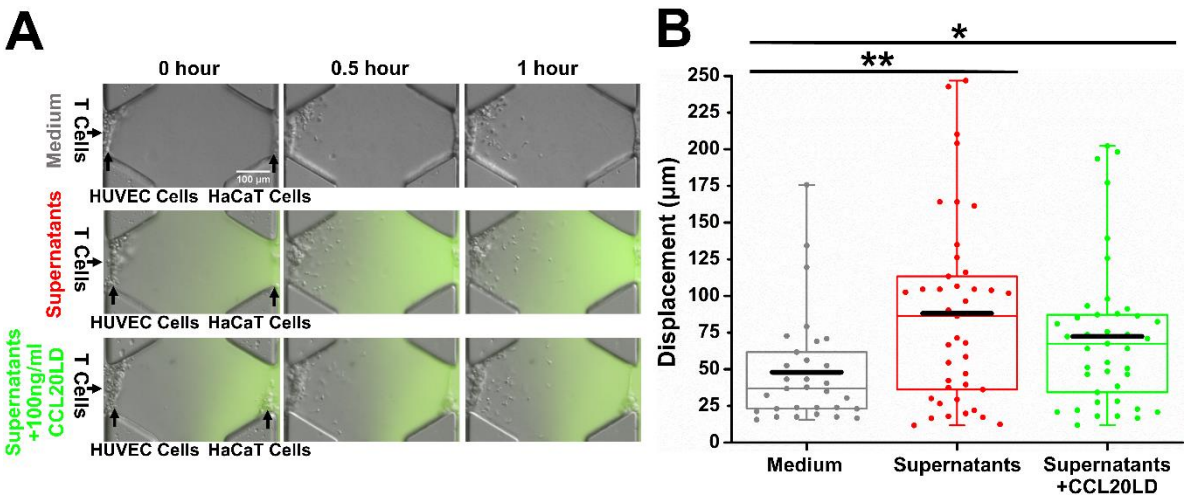

4.5 Discussion

Defined gel patterning in a microfluidic device enables the precise separation of cellular components and the formation of multiple chemical gradients with controllable directional flows. These are critical parameters in designing a sophisticated 3D tissue microenvironment that permits a quantifiable assessment on the migratory behaviors of immune cells. To this end, many studies have been using pillar-like designs in their devices for precise gel patterning [52,158-160]. Huang et al. developed a microfluidic device with post arrays resulting in multiple discrete 3D cell-laden hydrogel patterning for multicellular co-cultures [158]. Del Amo and coworkers developed a microfluidic device that applied micro-columns with surface tension in the channels for selective gel patterning to quantitatively study 3D chemotaxis of dermal human fibroblasts across the interface of collagen gel-based ECM in response to different chemoattractants [159]. To improve the complexity of the 3D system and to address limitations in the lack of cell-cell interactions for cell migration, Han et al. effectively integrated ECM, chemical gradient, and multicellular co-cultures in a microfluidic device for neutrophil transendothelial migration (TEM) [52]. This device mainly consists of one middle endothelial (EC) channel, two chemical side channels, and four smaller “T-shaped” ECM channels. The four ECM channels were designed in symmetry and each of them was flanked by one EC channel and one side channel. By using the similar pillar-like design for the microfluidic device, selective gel patterning was achieved for TEM in precisely configured 3D microenvironments. Similarly, Wu and coworkers developed a microfluidic device for the study of *in vivo*-like neutrophil TEM [160]. This device is composed of one top gel channel, two symmetric “V-shaped” side channels, and one “V-shaped” bottom channel, all internally connected with a central gel chamber. The presence of pillars in the gel chamber applied with surface tension enabled a precise configuration of ECM, EC, and chemical gradient generation for the relevant investigations.

Although the principle of using micropillars for selective gel patterning is not new [52,158-160], our SoC model includes innovative and compact micropillar design as reflected by their number, layout, and dimensions within the device. The major gel compartment of our design is 500 μm wide and contains four trapezoidal micropillars which are separated from

each other by a 120 μm gap. Many studies applied gel compartments in macroscale (e.g., ≥ 800 μm) to decrease the ratio of gap-to-compartment width in an attempt to reduce the risk of gel leakage [52,159]. In addition, the device size is frequently compromised by the length of major compartment that is composed of numerous micropillars in these studies, restricting the use of the device to one experiment performed each time [52,158,159]. By contrast, our device is designed with fewer micropillars and reduced compartment length (1140 μm), provides multiple fields of view for monitoring cell migration, and enables four independent experiments to be conducted simultaneously on a single device to expedite statistically validated experimental throughput. Furthermore, all these mentioned studies did not include the epidermal skin layer but only included ECM and endothelial cells, thus, providing an incomplete reconstruction of the skin *in-vivo* microenvironment [52,158-160]. Contractively, our device enables us to reconstitute key components of the human skin, including epidermis, dermis, and hypodermis in a well-controlled manner. Our SoC model is a promising *in-vitro* platform that not only integrates key features of human skin composed by relevant human cells and ECM but enables the reconstitution of complex chemical fields during skin inflammation generated by a single or co-existing chemical gradients and allows direct image analysis of T cell migration in a close to physiological 3D microenvironment.

Our unique SoC model provided new insight into T cell migratory behavior in a spatial cell-matrix composition that mimics aspects of skin inflammation to investigate the effect of individual cellular component. Validation of relevant chemokines (i.e., CXCL12 and CCL20) in our SoC model confirmed previous studies and replicated CXCL12 induced T cell transmigration from the epidermis to dermis and hypodermis for inflammatory angiogenesis [150-152], and CCL20 mediated T cell transmigration to the inflammatory sites from the hypodermis [139,149]. A single gradient of CXCL12 or CCL20WT significantly promoted T cell transmigration in our SoC model. The presence of a HUVEC cell layer promoted T cell migration, as shown by a significantly higher mean T cell displacement towards the CCL20WT gradient when compared to a setup devoid of HUVEC cell layer. This suggests that cellular interactions are important for T cell migration. The importance of ECM and 3D organization in our SoC model for T cell migration became obvious when comparing data obtained with this

3D device and 2D systems. Using our previously designed microfluidic device (i.e., the D^3-Chip) [163,164], very poor or different migratory responses of T cells in response to CCL20 were observed in 2D condition compared to the 3D conditions (i.e., SoC model). Contrary to the results obtained with the 3D SoC device, our results in the 2D system showed that low numbers of T cells migrated to the gradient of 1 μg/mL CCL20WT with mean cell displacement values comparable to medium control. At identical concentrations (i.e., 1 μg/mL, 10 μg/mL, and 100 μg/mL), CCL20WT and CCL20LD had similar effect on T cell migration, as shown by comparable migrated T cell numbers and mean cell displacement values (**Figure A.2**). Also, CCR6 expression of ahPBTs in the flow cytometry analysis (21.8%) and 2D on-chip staining (i.e., on-chip staining of T cells on top of the collagen substrate after cell migration experiments) was relatively low when compared to the 3D condition (i.e., on-chip staining of T cells within collagen gel after cell migration experiments) (**Figure A.3**). These results demonstrated that the transmigrated T cells in collagen gel were CCR6 positive. The superiority of 3D systems over 2D systems in predicting cell migratory responses has previously been reported and likely result from improved reconstitution of a more physiological tissue microenvironment [1,158].

The SoC model provides a controlled microenvironment in which to simulate complex cytokine gradients that mediate T cell migration during skin inflammation. T cell trafficking from secondary lymphoid tissues via the blood stream to the different skin layers during cutaneous inflammation is a highly dynamic process and engages multiple chemotactic signaling pathways [139,168,169]. For example, down-regulation of the lymph node homing receptor CCR7 and its ligands CCL21/19 coincides with an up-regulation of the CCR6/ CCL20 axis in the dermis and epidermis during cutaneous inflammation. This facilitates the egress of T cells from regional lymph nodes to the blood stream and transmigration of T cells from blood vessels to the inflammatory skin sites as part of the specific immune response [139]. The up-regulation of the CXCXR4/ CXCL12 axis in the hypodermis during skin inflammation results in reversed T cell trafficking to the sites of inflammatory angiogenesis [150-152]. Detailed studies demonstrated the up-regulation of the S1PR1/ S1P system in inflamed peripheral tissues (i.e., skin and blood vessels) and its high expression at inflammatory sites is believed to contribute to local T cell retention [153]. We tested the migratory responses of T cells in a set

of competing gradient experiments. This included T cell migration in a co-existing gradient of CXCL12 and CCL20WT at the HUVEC side and HaCaT side, respectively, with or without a uniform S1P background. The presence of a uniform S1P background significantly muted T cell transmigration through the HaCaT layer towards a CXCL12 gradient, which was consistent with previous reports that identified high expression of S1P as a retention signal for T cells at inflammatory sites [153]. Cell-cell interactions may promote T cell migration since we found a consistent impairment in T cell migration in the absence of HaCaT cell layer in the same competing gradient experiments. These results demonstrated a strength of the SoC model in monitoring and quantifying migration parameters of individual T cells in complex *in-vivo* chemical fields and the potential for the discovery of relevant chemotactic signaling pathways as new therapeutic targets. Significant involvement of additional chemotactic signaling pathways, including CCR4/ CCL17 and CCR10/ CCL27, have been identified in cutaneous inflammation [168,169] and the SoC model is a suitable platform to study their role in cutaneous T cell migration. Another strength of our multicellular SoC model is the ability to collect conditioned flow-through media to reconstitute skin inflammation intrinsically using specific TNF-α stimulation. Supernatants from TNF-α treated HaCaT cells applied to the SoC device revealed a significantly enhanced T cell transmigration through the HUVEC cell layer towards the gradient with significantly higher mean cell displacement compared to medium control conditions. These T cell migratory responses under conditions of complex pro-inflammatory stimuli is consistent with reports of different pro-inflammatory mediators capable of attracting T cells during skin inflammation [51,139,149-153].

The emergence of increasingly sophisticated OoC devices that utilize human cells in 3D matrices has made this strategy a viable alternative to animal experimentation for cell migration and drug screening studies [1,51,170]. The importance of T cell migration for maintaining skin homeostasis and the impact of dysregulated chemotactic signaling pathways on the pathogenesis of various skin diseases has been recognized [140-144,169]. The development of new immunotherapeutics targeting T cell chemotaxis for the treatment of a broad range of skin diseases has been realized [168,169] and requires advanced microfluidic devices capable of adequately simulating specific tissue microenvironmental cues. T cell homing to psoriatic

inflammatory sites coincides with an upregulation of the CCR6/ CCL20 axis in the dermis and epidermis [139,149] and this CCR6-mediated T cell migration can be muted by an engineered CCL20LD inhibitor believed to be a promising immunotherapeutic for the treatment of psoriasis [149]. With our SoC model, we were able to demonstrate that a uniform background of CCL20LD peptide disrupted T cell migration towards the CCL20 gradient. Furthermore, the SoC device also revealed the dominant pro-migratory effect of supernatants from TNF-α stimulated HaCaT cells on T cell migration in the presence of a co-existing gradient of CCL20LD. This finding is consistent with a previous report that demonstrated a marginal impact of CCL20LD on other chemokine receptor signaling [149]. Collectively, the knowledge gained from applications of skin disease-relevant inhibitors, like CCL20LD, in this new SoC microfluidic model identifies this device as a versatile new chemotactic drug screening tool capable of providing mechanistic insight vital for improving the design and therapeutic application of innovative immunotherapeutics.

Chapter 5: Conclusion

5.1 Conclusion of the key results

In this thesis, we reported the development of various microfluidics-based OoC related approaches, which uniquely allowed us to study the migratory responses of different immune cells in the mimicked organ-specific microenvironments and to test new chemotactic drug candidates.

Specifically, we developed a mimicked microenvironment relevant to COPD in the D^3-Chip to assess the effect of COPD sputum on the migration and chemotaxis of T cells from both COPD patients and healthy subjects in Chapter 2. Our results showed that the sputum supernatants from COPD patients not the healthy subjects, have a clear inhibition effect on the basal motility and chemotaxis of T cells from both COPD patients and healthy subjects. While the same sputum supernatants induced the migration of neutrophils from healthy subjects. This surprising finding may suggest a possible stopping mechanism that contributes T cell accumulation in the airway and facilitates the pathogenesis of COPD.

In Chapter 3, we simulated a cancer microenvironment based on the D^3-Chip to study murine NK cell migration and NK-4T1 cell interaction. The results in this proof-of-principle study demonstrated the feasibility of using this approach to quantitatively characterize: 1) the number and contact time of NK cells interacting with a cancer cell; 2) the tracking of the migration path and contact time of an individual NK cell with multiple cancer cells; and 3) the change in cancer cell morphology at the end of the NK-cancer interaction. In addition, the results showed that the supernatants of mDC promoted the migration of activated NK cells toward 4T1 cancer cells, which may suggest the promotion effect of activated DC for NK cell recruitment and its antitumor activity at tumor site.

Finally, we developed a microfluidics-based 3D SoC model to study transendothelial and transepithelial migration of human T lymphocytes in a mimicked skin inflammatory microenvironments and to test new drug candidates in Chapter 4. The results demonstrated: 1) CCL20-dependent T cell transendothelial migration was significantly inhibited by CCL20LD,

suggesting the potential immunotherapeutic use of CCL20LD for treating skin diseases such as psoriasis; 2) transepithelial migration of T cells in response to a CXCL12 gradient mimicking T cell egress from the skin is significantly reduced by a S1P background, revealing the role of S1P for T cell retention in the inflamed skin tissues; and 3) T cell transmigration in response to the supernatant of on-chip stimulated epithelial cells by inflammatory cytokines using the SoC model.

Collectively, we developed several OoC related approaches to mimic the relevant organ-specific microenvironments for quantitatively investigating the migratory responses of different immune cells, especially human blood T cells at a single cell level in response to physiologically relevant mediators and potential chemotactic drugs.

5.2 Novelty of the system

5.2.1 Novelty of the D^3-Chip and its application

The D^3-Chip has been used to perform the studies in Chapter 2 and 3, due to its various novel features. First, this chip is composed of three independent units that share a common microscopic field of view, which allows real-time imaging and parallel analysis of three independent experiments, thus, improves the experimental throughput. Second, the chemical gradient is independently generated in each unit in a pump-free manner. Specifically, the air pressure difference between the chemical inlets and outlet, and unique zigzag channels and compensation zone work together to enable the gradient generation. The gradient is stable and can last for at least a few hours. Third, each unit has a special cell docking area to connect the cell loading channel and main gradient channel. This innovative feature has various advantages, including: 1) the smaller size of barrier region, enabling the trapping of all loaded cells in the docking area at the beginning; 2) the precise control of initial positions of cells relative to the gradient direction, simplifying the later data analysis such as migration displacement measurement; and 3) the polarization and squeezing of cells through the docking region to chemical gradient, simulating the transmigration process of cells to the inflamed tissues via blood vessels.

All the advanced features of D^3-Chip enable the reconstitution of relevant microenvironment and ensure the accurate results readout for immune cell migration experiments. Indeed, we successfully mimicked the cellular microenvironment of airway in COPD using clinical samples (i.e., blood and sputum) from COPD patients based on the D^3-Chip. This approach characterizes the migration and chemotaxis of T cells from both COPD patients and healthy subjects in response to the COPD sputum at a single cell level, which better predicts the *in-vivo* situation of T cell trafficking in the pathogenesis of COPD. We also simulated a tumor microenvironment in the D^3-Chip by multi-cell co-culture of murine NK cells, 4T1 cancer cells, and the mDC supernatants. Using this approach, several migratory responses of NK and cancer cells can be quantitatively investigated, including: 1) the migration displacement of NK cells in response to control medium and mDC supernatant; 2) the migration path and contact time of one NK cell interacting with multiple cancer cells; 3) the number and time of NK cells contact with a cancer cell; and 4) the morphological change of cancer cells at the end of NK-cancer interaction.

5.2.2 Novelty of the micropillar device and its application

The micropillar device has been used to perform the study in Chapter 4 and it has many novel features. First, this device is consist of four identical independent units that allows four parallel experiments conducted simultaneously, which improve the experimental throughput. Second, the compact design of micropillars on the number, layout and dimension in the major compartment, 1) miniaturizing the size of each unit; 2) enabling precise gel patterning; and 3) defining different zones for cellular components and gradient generation. Third, a single or competing chemical gradient can be generated in each unit independently in a pump-free manner. Specifically, the gradient is generated based on the chemical diffusion from one side channel to the other through the porous holes of collagen gel, and the gradient can last for at least eight hours. Most importantly, this device provides a better platform to mimic the relevant microenvironment in 3D for investigating transmigratory behaviors of immune cells.

Indeed, we successfully reconstituted a SoC model of cutaneous microenvironment *in vitro* using the micropillar device. The *in-vivo* ratio of different skin layers in a normal human

skin (i.e., epithelium, dermis, and endothelium) is replicated by co-culture of multi-cellular components originating from human cell lines and ECM in the device. This approach also allows the generation of dynamic single or co-existing gradients of relevant inflammatory mediators. Compared with the D^3-Chip-based approaches, this SoC model solves the limitation of those approaches on the absence of key physical structures in mimicking organ-specific microenvironment. The effective integration of the respective advantages of 2D and 3D systems in this approach enables the investigation on more complicated immune cell migration related studies. Specifically, many important aspects of T cell transmigration in the inflamed skin have been quantitatively investigated, including: 1) the transendothelial and transepithelial migration of T cells in response to dynamic single or co-existing chemical gradients of relevant inflammatory chemokines; 2) the effect of chemotactic drug candidate (i.e., CCL20LD) on the transmigratory responses of T cells and its potential immunotherapeutic use for treating skin diseases; and 3) the on-chip simulation of T cell transmigration in a mimicked *in-vivo* skin inflammatory environment.

5.3 Engineering significance of the study

Given the importance of disease-oriented immune cell migration and the superiority of OoC related approach in configuring the organ-specific microenvironment, we developed various OoC related approaches to study the relevant immune cell migration in three major disease models, including COPD, cancer, and skin inflammation. These studies can be broadly defined to meet one or more of the following directions: developing OoC related approaches to investigate 1) immune cell migration by testing clinical cell or/and tissue samples for diagnostic assessment of organ-specific disease; 2) immune cell migration or/and interaction by configuring complex chemical fields relevant to target organs; and 3) immune cell migration and interaction by reconstituting the physiological structures of specific organs based on multi-cell co-culture.

For example, we mimicked a microenvironment relevant to COPD in the D^3-Chip, and for the first time, our results demonstrated the inhibitory effect of COPD sputum on T cell migration and chemotaxis. The results provided quantitative evidence and new information

about the complex involvement of T cell trafficking in COPD. In Chapter 3, a simulated cancer microenvironment was developed based on the D^3-Chip, and we demonstrated the feasibility of this approach for quantitative investigation on NK cell migration and NK-cancer cell interaction. Primary results in this proof-of-principle study also suggested the promotion effect of mDC supernatant for NK cell recruitment and its antitumor activity at tumor site. To improve the complexity of the system, we finally developed a SoC model with reconstituted cutaneous microenvironment *in vitro* in Chapter 4. This novel approach allowed us, for the first time, to quantitatively analyze human T cell migration in a multicellular 3D environment under controlled single and competing chemical gradient conditions. Our results demonstrated the feasibility and potential of this SoC model as a new medium throughput discovery and screening tool to study the involvement of T cell trafficking in complex chemical fields during cytokine-stimulated skin inflammation.

Collectively, all these studies fill the research gap that very few studies to date have applied organ-specific applications for disease-oriented immune cell migration, and advance our knowledge on the underlying mechanisms of immune cell migration in the relevant disease conditions. Our study provides substantial evidence that OoC related approach is superior to the other cell migration tools, which leads a new conceptual and technological direction for immune cell migration research in the future.

Chapter 6: Future direction

All the studies involved in this thesis are worth to be further investigated in many directions, and I will discuss the possible future directions for each of them in the following sections. It's worth pointing out that the last section of this chapter (i.e., **General limitations of OoC approach to overcome in the future**) is written based on my publication: "**Xiaoou Ren**, David Levin, and Francis Lin. *Cell migration research based on organ-on-chip-related approaches*. ***Micromachines*** **(IF: 2.523)**, **2017**; 8(11):324."

6.1 Future direction for the study in Chapter 2

As previously discussed in Chapter 2, the observed inhibitory effect of COPD sputum on T cell migration and chemotaxis is suspected that caused by the simplified 2D cellular microenvironment applied in the approach and the use of purified T cells for the migration experiments. T cell migration in response to COPD sputum may require the contact with other relevant cellular components (e.g., 3D ECM, endothelium, and other leukocytes) within the microenvironment. Indeed, a study reported the migration of total PBMCs but not isolated lymphocytes or monocytes from COPD patients induced by the chemokine gradients, which suggested the synergic effect between different immune cells that promoted immune cell recruitment to the lung in COPD [100]. To address these possible reasons, more advanced approach that better reconstitutes the physiologically relevant microenvironment is required to perform the further investigations, and our SoC model is a suitable platform in this direction. Relevantly, testing the effect of COPD sputum on non-activated T cells is interesting as our results show very different migratory responses of T cells in 2D and 3D environments. Furthermore, development of high-throughput approach that allows parallel analysis on the migration of different T cell subsets such as CD4+ and CD8+ T cells, in response to COPD sputum on a single chip will also be interesting. On the other hand, identification of the responsible components in the COPD sputum that inhibit T cell migration and chemotaxis is another important direction, which can be performed by Meso Scale Discovery and Luminex Assay as these methods have been used in another study for analyzing COPD sputum supernatant and measuring existing cytokines, chemokines and matrix metalloproteinases

[112]. Further investigation on this direction will better elucidate the underlying mechanisms of the inhibitory effect of COPD sputum on T cell migration and chemotaxis and its physiological relevance to COPD.

6.2 Future direction for the study in Chapter 3

The proof-of-principle study in Chapter 3 provides substantial evidence that demonstrates the suitability of our approach for quantitative investigation on NK cell migration and NK-cancer cell interaction in a mimicked tumor microenvironment. The preliminary results showed that the mDC supernatant (i.e., conditioned medium from LPS activated mDC) promoted the migration of activated NK cells toward 4T1 cancer cells in the system, which suggested the promotion effect of mDC on NK cell recruitment at the tumor side. To better elucidate this finding, parallel analysis on the migration of activated NK cells with different preparations (e.g., IL-2 or IL-15-activated NK cells) in response to various defined chemical gradients such as supernatants from iDC, mDC and cancer cells can be conducted as a direction. In addition to the innate immunity, investigation on the migratory responses of adaptive immune cells such as T cell migration and cancer-T cell interaction in the tumor microenvironment will be interesting. Detailed studies demonstrated that upon cancer-T cell interaction, different immune checkpoints of T cells such as programmed cell death receptor 1 (PD-1) and cytotoxic T-lymphocyte-associated antigen 4 (CTLA-4) can be mediated by cancer cells, leading to decreased T cell proliferation and activation, and increased T cell exhaustion [171-175]. It is a major self-protection mechanism during cancer development. Thus, investigating T cell migration and cancer-T cell interaction by targeting these signal pathways using transgenic cells in a mimicked tumor microenvironment will provide important insights to understand the antitumor mechanisms of T cells and develop relevant immunotherapy for cancer treatment. On the other hand, approach improvement that towards better reconstituting the tumor microenvironment in 3D is another important task and the establishment of SoC model can be a good example for this direction.

6.3 Future direction for the study in Chapter 4

The SoC model developed in this Chapter provides a better controlled 3D

microenvironment, which is an ideal platform for pursuing various cell migration-related studies. For example, literature reported other key chemotactic signaling pathways such as CCR7-CCL21/19, CCR4-CCL17, and CCR10-CCL27 significantly involved in the cutaneous inflammation [139,168,169], and their detailed roles during the process can be further investigated using our SoC model. As a drug screening tool, our SoC model can be applied for other disease-orientated cell migration studies by testing the effect of relevant drug candidates on the migratory responses of target cells. It's also interesting to develop other organ-specific models by using the strategy that applied in the SoC model. For instance, detailed studies reported several applications of OoC approaches such as brain-on-chip (BoC) [68,176] based on the similar strategy, and the HaCaT cells can be replaced by neural cells in our system to develop a mimicked BoC model for specific immune cell migration study. As previously discussed, investigation on cancer-T cell interaction and the relevant antitumor mechanisms on immune checkpoints in a better mimicked tumor microenvironment *in vitro* will be an interesting direction. To this, a tumor-on-chip model can be developed by substituting HaCaT cells with cancer cells in the SoC model based on the similar method. Our model better mimics the *in-vivo* transmigration of T cells in tissues in response to various chemical gradients that characterizes the migration displacement of each individual T cell towards the gradient direction, thus, can be used as a stable sorting tool for collecting cells with high directional motility. Latter gene sequencing for these collected cells can determine the target signaling pathways and advance our knowledge, which will be another interesting direction.

On the other hand, some important limitations of this SoC model need to be addressed in the future to improve the quality of technique. For example, the use of HaCaT/ HUVEC cells and 3D collagen gel to mimic the key features of different cutaneous compartments are much simplified compared to the complex *in-vivo* conditions, which is a common challenge for such an art of technique. The introduction of a collagen gel with porous networks limits gradient formation to a diffusion process, which is another common issue as compared to the flexible gradient generation in 2D systems. Although the selective collagen gel patterning is achieved in the SoC model, it still requires the attachment of different cell types to both sites of the gel and limits strategies of cell co-culture or cell patterning by embedding cells within the collagen

gel in this 3D device. The stiffness of the collagen gel may not ensure identical alignment of different cells at the gel surface and requires further improvements. Even though the initial position of loaded T cells has been manually adjusted during data analysis, this aspect can be made more precise using an automated strategy in the future.

6.4 General limitations of OoC approach to overcome in the future

Current OoC technologies for cell migration research are still in their infancy and thus are facing many common technical challenges. Firstly, precise presentation of guiding signals in space and time is an important building block of the organ microenvironment for cell migration. While 3D multi-cell co-culture microfluidic devices more closely mimic physiological tissue or organ microenvironments, the accompanied reduction in their ability to control and manipulate chemical gradients presents a significant drawback compared with 2D systems. In contrast, the 2D microfluidic approach is well established to study cell migration in precisely defined, simple and complex physiologically-relevant chemical fields. While these systems are fundamentally limited to mimic the real *in-vivo* situations, some cell types evidently show poor or very different migratory behaviors in the 2D systems compared with 3D systems. Therefore, developing OoC models that effectively integrate the respective advantages of 2D and 3D systems in a balanced manner sets one of the immediate future directions. For example, new techniques must be developed to enable advanced partition of 3D viscous gel zones and soluble flow zones within the microfluidic channels that would allow controlled flow transport over the gel environments. In this direction, 3D bio-printing technology offers a promising approach, owing to its unique ability for controlled and rapid reconstruction of different tissue structures. Recent studies have demonstrated the feasibility of integrating 3D printing with biocompatible micro/nanoparticles for biomimetic bone tissue engineering, which demonstrated the potential of 3D bio-printing for broad OoC applications [177-179]. Similarly, improved techniques are required to better pattern and partition multiple cell types in the device. Another approach can be embed microcapsules or micro/nanoparticles into the 3D gel-based microfluidic systems to allow controlled chemical release and gradient generation in space and time.

Secondly, while the widely used PDMS microfluidic devices offer advantages in fast prototyping, low cost, biocompatibility and optical transparency, the interactions between various biomolecules and PDMS can be a significant issue for OoC applications, such as drug testing and ECM configuration. New alternative device fabrication materials are, therefore, being explored. For example, recent studies showed that other elastomers such as polyurethanes offer similar features of PDMS, but higher compatibility with small hydrophobic drugs [180]. Cell migration in microfluidic devices fabricated from these new materials should be tested toward enabling more advanced OoC applications.

Thirdly, increased complexity of OoC approaches limits experimental throughput compared with simple devices. The throughput issue is also reflected by the isolated, single OoC approach for many current studies, which underscores the difficulty of accurately mimicking the complex properties of the interacting multi-organ environments in the body, wherein tightly regulated and highly dynamic cell migration and inter-organ trafficking occurs. Thus, innovative and optimized device designs to improve experimental throughput and advanced multi-organs-on-chip devices are highly desirable for future cell migration research. The work of Qin's group that mimicked the structural, functional and mechanical features of the BBB is an excellent example of such integrated multiple organ-mimicking units with microchannel networks that are required for advanced on-chip cell migration monitoring and analysis [68].

Finally, mimicking disease conditions and testing diseased clinical samples will ultimately enable diagnostic and therapeutic applications of the OoC approaches. On the other hand, disease-oriented studies are facing significant scientific and technological challenges to faithfully recreate the pathological processes on the chip, which presents an important open question for microfluidics and cell migration researchers to address in the future.

References

1. Ren, X.; Levin, D.; Lin, F. Cell migration research based on organ-on-chip-related approaches. *Micromachines* **2017**, *8*, 324.
2. Mitchison, T.J.; Cramer, L.P. Actin-based cell motility and cell locomotion. *Cell* **1996**, *84*, 371-379.
3. Lamalice, L.; Boeuf, F.L.; Huot, J. Endothelial cell migration during angiogenesis. *Circulation Research* **2007**, *100*, 782-794.
4. Dupre, L.; Houmadi, R.; Tang, C.; Rey-Barroso, J. T lymphocyte migration: An action movie starring the actin and associated actors. *Frontiers in immunology* **2015**, *6*, 586.
5. Zollner, T.M.; Asadullah, K. Selectin and selectin ligand binding: A bittersweet attraction. *The Journal of clinical investigation* **2003**, *112*, 980-983.
6. Wu, J.; Hillier, C.; Komenda, P.; Lobato de Faria, R.; Levin, D.; Zhang, M.; Lin, F. A microfluidic platform for evaluating neutrophil chemotaxis induced by sputum from COPD patients. *PloS one* **2015**, *10*, e0126523.
7. Diamond, M.S.; Springer, T.A. The dynamic regulation of integrin adhesiveness. *Current Biology* **1994**, *4*, 506-517.
8. Johnston, B.; Butcher, E.C. Chemokines in rapid leukocyte adhesion triggering and migration. *Seminars in Immunology* **2002**, *14*, 83-92.
9. Fabbri, M.; Bianchi, E.; Fumagalli, L.; Pardi, R. Regulation of lymphocyte traffic by adhesion molecules. *Inflammation Research* **1999**, *48*, 239-246.
10. Fu, H.; Ward, E.J.; Marelli-Berg, F.M. Mechanisms of T cell organotropism. *Cellular and Molecular Life Sciences* **2016**, *73*, 3009-3033.
11. Kumar, V.; Sharma, A. Neutrophils: Cinderella of innate immune system. *International Immunopharmacology* **2010**, *10*, 1325-1334.
12. Borregaard, N. Neutrophils, from marrow to microbes. *Immunity* **2010**, *33*, 657-670.
13. Banchereau, J.; Briere, F.; Caux, C.; Davoust, J.; Lebecque, S.; Liu, Y.-J.; Pulendran, B.; Palucka, K. Immunobiology of dendritic cells. *Annual review of immunology* **2000**, *18*, 767-811.
14. Ricart, B.G.; John, B.; Lee, D.; Hunter, C.A.; Hammer, D.A. Dendritic cells distinguish

individual chemokine signals through CCR7 and CXCR4. *The Journal of Immunology* **2010**, *186*, 53.

15. Campbell, K.S.; Hasegawa, J. Natural killer cell biology: An update and future directions. *The Journal of allergy and clinical immunology* **2013**, *132*, 536-544.
16. Walzer, T.; Vivier, E. G-protein-coupled receptors in control of natural killer cell migration. *Trends in Immunology* **2011**, *32*, 486-492.
17. Chen, X.; Jensen, P.E. The role of B lymphocytes as antigen-presenting cells. *Archivum Immunologiae et Therapiae Experimentalis* **2008**, *56*, 77.
18. Kondo, M. Lymphoid and myeloid lineage commitment in multipotent hematopoietic progenitors. *Immunological reviews* **2010**, *238*, 37-46.
19. Hardtke, S.; Ohl, L.; Förster, R. Balanced expression of CXCR5 and CCR7 on follicular T helper cells determines their transient positioning to lymph node follicles and is essential for efficient B-cell help. *Blood* **2005**, *106*, 1924.
20. Schwarz, B.A.; Bhandoola, A. Trafficking from the bone marrow to the thymus: A prerequisite for thymopoiesis. *Immunological reviews* **2006**, *209*, 47-57.
21. Nandagopal, S.; Wu, D.; Lin, F. Combinatorial guidance by CCR7 ligands for T lymphocytes migration in co-existing chemokine fields. *PloS one* **2011**, *6*, e18183.
22. Worbs, T.; Förster, R. T cell migration dynamics within lymph nodes during steady state: An overview of extracellular and intracellular factors influencing the basal intranodal T cell motility. In *Visualizing immunity*, Dustin, M.; McGavern, D., Eds. Springer Berlin Heidelberg: Berlin, Heidelberg, 2009; pp 71-105.
23. Luster, A.D.; Alon, R.; von Andrian, U.H. Immune cell migration in inflammation: Present and future therapeutic targets. *Nature immunology* **2005**, *6*, 1182.
24. Monaco, C.; Andreakos, E.; Kiriakidis, S.; Feldmann, M.; Paleolog, E. T-cell-mediated signalling in immune, inflammatory and angiogenic processes: The cascade of events leading to inflammatory diseases. *Current Drug Targets-Inflammation & Allergy* **2004**, *3*, 35-42.
25. Rabe, K.F.; Hurd, S.; Anzueto, A.; Barnes, P.J.; Buist, S.A.; Calverley, P.; Fukuchi, Y.; Jenkins, C.; Rodriguez-Roisin, R.; Van Weel, C. Global strategy for the diagnosis, management, and prevention of chronic obstructive pulmonary disease: Gold executive

summary. *American journal of respiratory and critical care medicine* **2007**, *176*, 532-555.

26. Fahy, J.V.; Dickey, B.F. Airway mucus function and dysfunction. *New England Journal of Medicine* **2010**, *363*, 2233-2247.
27. Lai, P.S.; Fresco, J.M.; Pinilla, M.A.; Macias, A.A.; Brown, R.D.; Englert, J.A.; Hofmann, O.; Lederer, J.A.; Hide, W.; Christiani, D.C. Chronic endotoxin exposure produces airflow obstruction and lung dendritic cell expansion. *American journal of respiratory cell and molecular biology* **2012**, *47*, 209-217.
28. Wong, J.; Magun, B.E.; Wood, L.J. Lung inflammation caused by inhaled toxicants: A review. *International journal of chronic obstructive pulmonary disease* **2016**, *11*, 1391.
29. Schleimer, R.P. Innate immune responses and chronic obstructive pulmonary disease: "Terminator" or "terminator 2"? *Proceedings of the American Thoracic Society* **2005**, *2*, 342-346.
30. Teresa, D.T. Inflammatory cells and chronic obstructive pulmonary disease. *Current Drug Targets - Inflammation & Allergy* **2005**, *4*, 607-618.
31. Quint, J.K.; Wedzicha, J.A. The neutrophil in chronic obstructive pulmonary disease. *Journal of Allergy and Clinical Immunology* **2007**, *119*, 1065-1071.
32. Barnes, P.J.; Shapiro, S.D.; Pauwels, R.A. Chronic obstructive pulmonary disease: Molecular and cellularmechanisms. *European Respiratory Journal* **2003**, *22*, 672.
33. Yum, K.; Hong, S.G.; Healy, K.E.; Lee, L.P. Physiologically relevant organs on chips. *Biotechnology journal* **2014**, *9*, 16-27.
34. van den Broek, L.J.; Bergers, L.I.J.C.; Reijnders, C.M.A.; Gibbs, S. Progress and future prospectives in skin-on-chip development with emphasis on the use of different cell types and technical challenges. *Stem Cell Reviews and Reports* **2017**, 1-12.
35. Seok, J.; Warren, H.S.; Cuenca, A.G.; Mindrinos, M.N.; Baker, H.V.; Xu, W.; Richards, D.R.; McDonald-Smith, G.P.; Gao, H.; Hennessy, L., *et al.* Genomic responses in mouse models poorly mimic human inflammatory diseases. *Proceedings of the National Academy of Sciences of the United States of America* **2013**, *110*, 3507-3512.
36. Mak, I.W.Y.; Evaniew, N.; Ghert, M. Lost in translation: Animal models and clinical trials in cancer treatment. *American Journal of Translational Research* **2014**, *6*, 114-118.

37. Boyden, S. The chemotactic effect of mixtures of antibody and antigen on polymorphonuclear leucocytes. *Journal of Experimental Medicine* **1962**, *115*, 453-466.
38. van der Meer, A.D.; Poot, A.A.; Duits, M.H.G.; Feijen, J.; Vermes, I. Microfluidic technology in vascular research. *Journal of Biomedicine and Biotechnology* **2009**, *2009*, 823148.
39. Velve-Casquillas, G.; Le Berre, M.; Piel, M.; Tran, P.T. Microfluidic tools for cell biological research. *Nano today* **2010**, *5*, 28-47.
40. Lin, F.; Butcher, E.C. T cell chemotaxis in a simple microfluidic device. *Lab on a Chip* **2006**, *6*, 1462-1469.
41. Lin, F. Chapter 15. A microfluidics-based method for analyzing leukocyte migration to chemoattractant gradients. In *Methods in enzymology*, Academic Press: 2009; Vol. Volume 461, pp 333-347.
42. Li, J.; Lin, F. Microfluidic devices for studying chemotaxis and electrotaxis. *Trends in Cell Biology* **2011**, *21*, 489-497.
43. Wu, J.; Wu, X.; Lin, F. Recent developments in microfluidics-based chemotaxis studies. *Lab on a Chip* **2013**, *13*, 2484-2499.
44. Sackmann, E.K.-H.; Berthier, E.; Schwantes, E.A.; Fichtinger, P.S.; Evans, M.D.; Dziadzio, L.L.; Huttenlocher, A.; Mathur, S.K.; Beebe, D.J. Characterizing asthma from a drop of blood using neutrophil chemotaxis. *Proceedings of the National Academy of Sciences of the United States of America* **2014**, *111*, 5813-5818.
45. Bhatia, S.N.; Ingber, D.E. Microfluidic organs-on-chips. *Nature biotechnology* **2014**, *32*, 760-772.
46. Zheng, F.; Fu, F.; Cheng, Y.; Wang, C.; Zhao, Y.; Gu, Z. Organ-on-a-chip systems: Microengineering to biomimic living systems. *Small* **2016**, *12*, 2253-2282.
47. Khademhosseini, A. *Micro and nanoengineering of the cell microenvironment: Technologies and applications*. Artech House: 2008.
48. Lee, P.J.; Hung, P.J.; Lee, L.P. An artificial liver sinusoid with a microfluidic endothelial-like barrier for primary hepatocyte culture. *Biotechnology and Bioengineering* **2007**, *97*, 1340-1346.
49. Vernetti, L.A.; Senutovitch, N.; Boltz, R.; DeBiasio, R.; Ying Shun, T.; Gough, A.; Taylor,

D.L. A human liver microphysiology platform for investigating physiology, drug safety, and disease models. *Experimental biology and medicine* **2016**, *241*, 101-114.

50. Jang, K.-J.; Mehr, A.P.; Hamilton, G.A.; McPartlin, L.A.; Chung, S.; Suh, K.-Y.; Ingber, D.E. Human kidney proximal tubule-on-a-chip for drug transport and nephrotoxicity assessment. *Integrative Biology* **2013**, *5*, 1119-1129.
51. Wufuer, M.; Lee, G.; Hur, W.; Jeon, B.; Kim, B.J.; Choi, T.H.; Lee, S. Skin-on-a-chip model simulating inflammation, edema and drug-based treatment. *Sci Rep* **2016**, *6*, 37471.
52. Han, S.; Yan, J.-J.; Shin, Y.; Jeon, J.J.; Won, J.; Eun Jeong, H.; Kamm, R.D.; Kim, Y.-J.; Chung, S. A versatile assay for monitoring in vivo-like transendothelial migration of neutrophils. *Lab on a Chip* **2012**, *12*, 3861-3865.
53. Zervantonakis, I.K.; Hughes-Alford, S.K.; Charest, J.L.; Condeelis, J.S.; Gertler, F.B.; Kamm, R.D. Three-dimensional microfluidic model for tumor cell intravasation and endothelial barrier function. *Proceedings of the National Academy of Sciences* **2012**, *109*, 13515-13520.
54. Christakou, A.E.; Ohlin, M.; Onfelt, B.; Wiklund, M. Ultrasonic three-dimensional on-chip cell culture for dynamic studies of tumor immune surveillance by natural killer cells. *Lab on a Chip* **2015**, *15*, 3222-3231.
55. Gioiella, F.; Urciuolo, F.; Imparato, G.; Brancato, V.; Netti, P.A. An engineered breast cancer model on a chip to replicate ECM-activation in vitro during tumor progression. *Advanced healthcare materials* **2016**, *5*, 3074-3084.
56. Lei, Y.; Li, J.; Wang, N.; Yang, X.; Hamada, Y.; Li, Q.; Zheng, W.; Jiang, X. An on-chip model for investigating the interaction between neurons and cancer cells. *Integrative Biology* **2016**, *8*, 359-367.
57. Huh, D.; Matthews, B.D.; Mammoto, A.; Montoya-Zavala, M.; Hsin, H.Y.; Ingber, D.E. Reconstituting organ-level lung functions on a chip. *Science* **2010**, *328*, 1662.
58. Yang, K.; Wu, J.; Zhu, L.; Liu, Y.; Zhang, M.; Lin, F. An all-on-chip method for rapid neutrophil chemotaxis analysis directly from a drop of blood. *Journal of visualized experiments : JoVE* **2017**, *124*, 55615.
59. Zhang, Q.; Liu, T.; Qin, J. A microfluidic-based device for study of transendothelial invasion of tumor aggregates in realtime. *Lab on a chip* **2012**, *12*, 2837-2842.

60. Chen, M.B.; Whisler, J.A.; Fröse, J.; Yu, C.; Shin, Y.; Kamm, R.D. On-chip human microvasculature assay for visualization and quantitation of tumor cell extravasation dynamics. *Nature protocols* **2017**, *12*, 865.

61. Tourovskaia, A.; Fauver, M.; Kramer, G.; Simonson, S.; Neumann, T. Brief communication: Tissue-engineered microenvironment systems for modeling human vasculature. *Experimental biology and medicine* **2014**, *239*, 1264-1271.

62. Moura Rosa, P.; Gopalakrishnan, N.; Ibrahim, H.; Haug, M.; Halaas, O. The intercell dynamics of T cells and dendritic cells in a lymph node-on-a-chip flow device. *Lab on a Chip* **2016**, *16*, 3728-3740.

63. Mitra, B.; Jindal, R.; Lee, S.; Dong, D.X.; Li, L.; Sharma, N.; Maguire, T.; Schloss, R.; Yarmush, M.L. Microdevice integrating innate and adaptive immune responses associated with antigen presentation by dendritic cells. *RSC Advances* **2013**, *3*, 16002-16010.

64. Haessler, U.; Pisano, M.; Wu, M.; Swartz, M.A. Dendritic cell chemotaxis in 3D under defined chemokine gradients reveals differential response to ligands CCL21 and CCL19. *Proceedings of the National Academy of Sciences of the United States of America* **2011**, *108*, 5614-5619.

65. Kilic, O.; Pamies, D.; Lavell, E.; Schiapparelli, P.; Feng, Y.; Hartung, T.; Bal-Price, A.; Hogberg, H.T.; Quinones-Hinojosa, A.; Guerrero-Cazares, H., *et al.* Brain-on-a-chip model enables analysis of human neuronal differentiation and chemotaxis. *Lab on a Chip* **2016**, *16*, 4152-4162.

66. Nery, F.C.; da Hora, C.C.; Yaqub, U.; Zhang, X.; McCarthy, D.M.; Bhide, P.G.; Irimia, D.; Breakefield, X.O. New methods for investigation of neuronal migration in embryonic brain explants. *Journal of neuroscience methods* **2015**, *0*, 80-84.

67. Keenan, T.M.; Grinager, J.R.; Procak, A.A.; Svendsen, C.N. In vitro localization of human neural stem cell neurogenesis by engineered FGF-2 gradients. *Integrative Biology* **2012**, *4*, 1522-1531.

68. Xu, H.; Li, Z.; Yu, Y.; Sizdahkhani, S.; Ho, W.S.; Yin, F.; Wang, L.; Zhu, G.; Zhang, M.; Jiang, L., *et al.* A dynamic in vivo-like organotypic blood-brain barrier model to probe metastatic brain tumors. *Scientific Reports* **2016**, *6*, 36670.

69. Nguyen, D.X.; Bos, P.D.; Massagué, J. Metastasis: From dissemination to organ-specific colonization. *Nature reviews. Cancer* **2009**, *9*, 274.

70. Steeg, P.S. Tumor metastasis: Mechanistic insights and clinical challenges. *Nature medicine* **2006**, *12*, 895.

71. Friedl, P.; Alexander, S. Cancer invasion and the microenvironment: Plasticity and reciprocity. *Cell* **2011**, *147*, 992-1009.

72. Calvo, F.; Sahai, E. Cell communication networks in cancer invasion. *Current opinion in cell biology* **2011**, *23*, 621-629.

73. Roussos, E.T.; Condeelis, J.S.; Patsialou, A. Chemotaxis in cancer. *Nature reviews. Cancer* **2011**, *11*, 573-587.

74. Gupta, G.P.; Massagué, J. Cancer metastasis: Building a framework. *Cell* **2006**, *127*, 679-695.

75. Pavesi, A.; Tan, A.T.; Koh, S.; Chia, A.; Colombo, M.; Antonecchia, E.; Miccolis, C.; Ceccarello, E.; Adriani, G.; Raimondi, M.T., *et al.* A 3D microfluidic model for preclinical evaluation of TCR-engineered T cells against solid tumors. *JCI Insight* **2017**, *2*, e89762.

76. Bapat, A.A.; Hostetter, G.; Von Hoff, D.D.; Han, H. Perineural invasion and associated pain in pancreatic cancer. *Nat Rev Cancer* **2011**, *11*, 695-707.

77. Kolaczkowska, E.; Kubes, P. Neutrophil recruitment and function in health and inflammation. *Nature reviews. Immunology* **2013**, *13*, 159.

78. Fahy, J.V. Eosinophilic and neutrophilic inflammation in asthma: Insights from clinical studies. *Proceedings of the American Thoracic Society* **2009**, *6*, 256-259.

79. Amulic, B.; Cazalet, C.; Hayes, G.L.; Metzler, K.D.; Zychlinsky, A. Neutrophil function: From mechanisms to disease. *Annual review of immunology* **2012**, *30*, 459-489.

80. Turato, G.; Zuin, R.; Saetta, M. Pathogenesis and pathology of COPD. *Respiration* **2001**, *68*, 117-128.

81. Yamamoto, C.; Yoneda, T.; Yoshikawa, M.; Fu, A.; Tokayama, T.; Tsukaguchi, K.; Narita, N. Airway inflammation in COPD assessed by sputum levels of lnterleukin-8. *Chest* **1997**, *112*, 505-510.

82. Middleton, J.; Patterson, A.M.; Gardner, L.; Schmutz, C.; Ashton, B.A. Leukocyte

extravasation: Chemokine transport and presentation by the endothelium. *Blood* **2002**, *100*, 3853-3860.

83. Woodfin, A.; Voisin, M.-B.; Imhof, B.A.; Dejana, E.; Engelhardt, B.; Nourshargh, S. Endothelial cell activation leads to neutrophil transmigration as supported by the sequential roles of ICAM-2, JAM-a, and PECAM-1. *Blood* **2009**, *113*, 6246-6257.
84. Miles, F.L.; Pruitt, F.L.; van Golen, K.L.; Cooper, C.R. Stepping out of the flow: Capillary extravasation in cancer metastasis. *Clinical & experimental metastasis* **2008**, *25*, 305-324.
85. Randolph, G.J.; Angeli, V.; Swartz, M.A. Dendritic-cell trafficking to lymph nodes through lymphatic vessels. *Nature reviews. Immunology* **2005**, *5*, 617.
86. Banchereau, J.; Steinman, R.M. Dendritic cells and the control of immunity. *Nature* **1998**, *392*, 245.
87. Lanzavecchia, A.; Sallusto, F. Dynamics of T lymphocyte responses: Intermediates, effectors, and memory cells. *Science* **2000**, *290*, 92-97.
88. Quaratino, S.; Duddy, L.P.; Londei, M. Fully competent dendritic cells as inducers of T cell anergy in autoimmunity. *Proceedings of the National Academy of Sciences* **2000**, *97*, 10911-10916.
89. Sallusto, F.; Palermo, B.; Lenig, D.; Miettinen, M.; Matikainen, S.; Julkunen, I.; Forster, R.; Burgstahler, R.; Lipp, M.; Lanzavecchia, A. Distinct patterns and kinetics of chemokine production regulate dendritic cell function. *European journal of immunology* **1999**, *29*, 1617-1625.
90. Kim, C.H.; Broxmeyer, H.E. Chemokines: Signal lamps for trafficking of T and B cells for development and effector function. *Journal of leukocyte biology* **1999**, *65*, 6-15.
91. Wang, Y.; Li, G.; Stanco, A.; Long, J.E.; Crawford, D.; Potter, G.B.; Pleasure, S.J.; Behrens, T.; Rubenstein, J.L. CXCR4 and CXCR7 have distinct functions in regulating interneuron migration. *Neuron* **2011**, *69*, 61-76.
92. Stumm, R.K.; Rummel, J.; Junker, V.; Culmsee, C.; Pfeiffer, M.; Krieglstein, J.; Höllt, V.; Schulz, S. A dual role for the SDF-1/CXCR4 chemokine receptor system in adult brain: Isoform-selective regulation of SDF-1 expression modulates CXCR4-dependent neuronal plasticity and cerebral leukocyte recruitment after focal ischemia. *Journal of*

Neuroscience **2002**, *22*, 5865-5878.

93. Zagzag, D.; Esencay, M.; Mendez, O.; Yee, H.; Smirnova, I.; Huang, Y.; Chiriboga, L.; Lukyanov, E.; Liu, M.; Newcomb, E.W. Hypoxia-and vascular endothelial growth factor-induced stromal cell-derived factor-1α/CXCR4 expression in glioblastomas: One plausible explanation of scherer's structures. *The American journal of pathology* **2008**, *173*, 545-560.
94. Medina, K.L. Chapter 4 - overview of the immune system. In *Handbook of clinical neurology*, Sean, J.P.; Angela, V., Eds. Elsevier: 2016; Vol. Volume 133, pp 61-76.
95. Wu, Q.; Liu, J.; Wang, X.; Feng, L.; Wu, J.; Zhu, X.; Wen, W.; Gong, X. Organ-on-a-chip: Recent breakthroughs and future prospects. *BioMedical Engineering OnLine* **2020**, *19*, 9.
96. Finkelstein, R.; Fraser, R.S.; Ghezzo, H.; Cosio, M.G. Alveolar inflammation and its relation to emphysema in smokers. *American journal of respiratory and critical care medicine* **1995**, *152*, 1666-1672.
97. Grumelli, S.; Corry, D.B.; Song, L.-Z.; Song, L.; Green, L.; Huh, J.; Hacken, J.; Espada, R.; Bag, R.; Lewis, D.E. An immune basis for lung parenchymal destruction in chronic obstructive pulmonary disease and emphysema. *PLoS medicine* **2004**, *1*, e8.
98. Richman-Eisenstat, J.; Jorens, P.G.; Hebert, C.; Ueki, I.; Nadel, J. Interleukin-8: An important chemoattractant in sputum of patients with chronic inflammatory airway diseases. *American Journal of Physiology-Lung Cellular and Molecular Physiology* **1993**, *264*, L413-L418.
99. Beeh, K.M.; Kornmann, O.; Buhl, R.; Culpitt, S.V.; Giembycz, M.A.; Barnes, P.J. Neutrophil chemotactic activity of sputum from patients with COPD: Role of interleukin 8 and leukotriene B4. *Chest* **2003**, *123*, 1240-1247.
100. Costa, C.; Traves, S.L.; Tudhope, S.J.; Fenwick, P.S.; Belchamber, K.B.R.; Russell, R.E.K.; Barnes, P.J.; Donnelly, L.E. Enhanced monocyte migration to CXCR3 and CCR5 chemokines in COPD. *European Respiratory Journal* **2016**, *47*, 1093.
101. Yang, K.; Peretz-Soroka, H.; Wu, J.; Zhu, L.; Cui, X.; Zhang, M.; Rigatto, C.; Liu, Y.; Lin, F. Fibroblast growth factor 23 weakens chemotaxis of human blood neutrophils in microfluidic devices. *Scientific Reports* **2017**, *7*, 3100.

102. Sethi, S.; Murphy, T.F. Infection in the pathogenesis and course of chronic obstructive pulmonary disease. *New England Journal of Medicine* **2008**, *359*, 2355-2365.
103. Wu, D.; Joyee, A.G.; Nandagopal, S.; Lopez, M.; Ma, X.; Berry, J.; Lin, F. Effects of clostridium difficile toxin A and B on human T lymphocyte migration. *Toxins* **2013**, *5*, 926-938.
104. Rao, R.M.; Betz, T.V.; Lamont, D.J.; Kim, M.B.; Shaw, S.K.; Froio, R.M.; Baleux, F.; Arenzana-Seisdedos, F.; Alon, R.; Luscinskas, F.W. Elastase release by transmigrating neutrophils deactivates endothelial-bound SDF-1α and attenuates subsequent T lymphocyte transendothelial migration. *The Journal of Experimental Medicine* **2004**, *200*, 713-724.
105. Li, J.; Nandagopal, S.; Wu, D.; Romanuik, S.F.; Paul, K.; Thomson, D.J.; Lin, F. Activated T lymphocytes migrate toward the cathode of DC electric fields in microfluidic devices. *Lab on a Chip* **2011**, *11*, 1298-1304.
106. Yamada, A.; Renault, R.; Chikina, A.; Venzac, B.; Pereiro, I.; Coscoy, S.; Verhulsel, M.; Parrini, M.C.; Villard, C.; Viovy, J.-L., *et al.* Transient microfluidic compartmentalization using actionable microfilaments for biochemical assays, cell culture and organs-on-chip. *Lab on a Chip* **2016**, *16*, 4691-4701.
107. Li, J.; Zhu, L.; Zhang, M.; Lin, F. Microfluidic device for studying cell migration in single or co-existing chemical gradients and electric fields. *Biomicrofluidics* **2012**, *6*, 024121.
108. Jaigirdar, S.A.; Benson, R.A.; Elmesmari, A.; Kurowska-Stolarska, M.S.; McInnes, I.B.; Garside, P.; MacLeod, M.K.L. Sphingosine-1-phosphate promotes the persistence of activated CD4 T cells in inflamed sites. *Frontiers in immunology* **2017**, *8*, 1627.
109. Macfarlane, F.R.; Lorenzi, T.; Chaplain, M.A. Modelling the immune response to cancer: An individual-based approach accounting for the difference in movement between inactive and activated t cells. *Bulletin of mathematical biology* **2018**, *80*, 1539-1562.
110. Saetta, M.; Baraldo, S.; Corbino, L.; Turato, G.; Braccioni, F.; Rea, F.; Cavallesco, G.; Tropeano, G.; Mapp, C.E.; Maestrelli, P. CD8+ ve cells in the lungs of smokers with chronic obstructive pulmonary disease. *American journal of respiratory and critical care medicine* **1999**, *160*, 711-717.
111. O'Shaughnessy, T.C.; Ansari, T.W.; Barnes, N.C.; Jeffery, P.K. Inflammation in bronchial

biopsies of subjects with chronic bronchitis: Inverse relationship of CD8+ T lymphocytes with fev1. *American journal of respiratory and critical care medicine* **1997**, *155*, 852-857.

112. Bafadhel, M.; McCormick, M.; Saha, S.; McKenna, S.; Shelley, M.; Hargadon, B.; Mistry, V.; Reid, C.; Parker, D.; Dodson, P. Profiling of sputum inflammatory mediators in asthma and chronic obstructive pulmonary disease. *Respiration* **2012**, *83*, 36-44.
113. Paplińska-Goryca, M.; Nejman-Gryz, P.; Górska, K.; Białek-Gosk, K.; Hermanowicz-Salamon, J.; Krenke, R. Expression of inflammatory mediators in induced sputum: Comparative study in asthma and COPD. *Advances in experimental medicine and biology* **2018**, *1040*, 101-112.
114. Barnes, P.J.; Cosio, M.G. Characterization of T lymphocytes in chronic obstructive pulmonary disease. *PLoS medicine* **2004**, *1*, e20.
115. Leckie, M.; Jenkins, G.; Khan, J.; Smith, S.; Walker, C.; Barnes, P.; Hansel, T. Sputum T lymphocytes in asthma, COPD and healthy subjects have the phenotype of activated intraepithelial T cells (CD69+ CD103+). *Thorax* **2003**, *58*, 23-29.
116. Mathai, R.T.K.; Bhat, S. Peripheral blood T-cell populations in COPD, asymptomatic smokers and healthy non-smokers in indian subpopulation-a pilot study. *Journal of clinical and diagnostic research: JCDR* **2013**, *7*, 1109.
117. Saetta, M.; Turato, G.; Maestrelli, P.; Mapp, C.E.; Fabbri, L. Cellular and structural bases of chronic obstructive pulmonary disease. *American Journal of Respiratory and Critical Care Medicine* **2001**, *163*, 1304-1309.
118. Retamales, I.; Elliott, W.M.; Meshi, B.; Coxson, H.; Pare, P.; Sciurba, F.; Rogers, R.; Hayashi, S.; Hogg, J. Amplification of inflammation in emphysema and its association with latent adenoviral infection. *American Journal of Respiratory and Critical Care Medicine* **2001**, *164*, 469-473.
119. Seemungal, T.A.; Harper-Owen, R.; Bhowmik, A.; Jeffries, D.J.; Wedzicha, J.A. Detection of rhinovirus in induced sputum at exacerbation of chronic obstructive pulmonary disease. *European Respiratory Journal* **2000**, *16*, 677.
120. Freeman, C.M.; Curtis, J.L.; Chensue, S.W. CC chemokine receptor 5 and CXC chemokine receptor 6 expression by lung CD8+ cells correlates with chronic obstructive

pulmonary disease severity. *The American Journal of Pathology* **2007**, *171*, 767-776.

121. Sales, D.S.; Ito, J.T.; Zanchetta, I.A.; Annoni, R.; Aun, M.V.; Ferraz, L.F.S.; Cervilha, D.A.; Negri, E.; Mauad, T.; Martins, M.A. Regulatory T-cell distribution within lung compartments in COPD. *COPD: Journal of Chronic Obstructive Pulmonary Disease* **2017**, *14*, 533-542.
122. Lee, B.; Ko, E.; Lee, J.; Jo, Y.; Hwang, H.; Goh, T.S.; Joo, M.; Hong, C. Soluble common gamma chain exacerbates COPD progress through the regulation of inflammatory T cell response in mice. *International journal of chronic obstructive pulmonary disease* **2017**, *12*, 817.
123. Tsoumakidou, M.; Demedts, I.K.; Brusselle, G.G.; Jeffery, P.K. Dendritic cells in chronic obstructive pulmonary disease: New players in an old game. *American journal of respiratory and critical care medicine* **2008**, *177*, 1180-1186.
124. Saetta, M.; Baraldo, S.; Turato, G.; Beghe, B.; Casoni, G.; Bellettato, C.; Rea, F.; Zuin, R.; Fabbri, L.; Papi, A. Increased proportion of CD8+ T-lymphocytes in the paratracheal lymph nodes of smokers with mild COPD. *Sarcoidosis, vasculitis, and diffuse lung diseases: official journal of WASOG* **2003**, *20*, 28-32.
125. Mahmood, S.; Kanwar, N.; Tran, J.; Zhang, M.-L.; Kung, S.K.P. SHP-1 phosphatase is a critical regulator in preventing natural killer cell self-killing. *PloS one* **2012**, *7*, e44244.
126. Cella, M.; Miller, H.; Song, C. Beyond NK cells: The expanding universe of innate lymphoid cells. *Frontiers in immunology* **2014**, *5*, 282-282.
127. Bernardini, G.; Sciumè, G.; Santoni, A. Differential chemotactic receptor requirements for NK cell subset trafficking into bone marrow. *Frontiers in immunology* **2013**, *4*, 12.
128. Pachynski, R.K.; Zabel, B.A.; Kohrt, H.E.; Tejeda, N.M.; Monnier, J.; Swanson, C.D.; Holzer, A.K.; Gentles, A.J.; Sperinde, G.V.; Edalati, A., *et al*. The chemoattractant chemerin suppresses melanoma by recruiting natural killer cell antitumor defenses. *The Journal of experimental medicine* **2012**, *209*, 1427-1435.
129. Ferlazzo, G.; Morandi, B. Cross-talks between natural killer cells and distinct subsets of dendritic cells. *Frontiers in immunology* **2014**, *5*, 159-159.
130. Alamri, A.; Rahman, R.; Zhang, M.; Alamri, A.; Gounni, A.S.; Kung, S.K.P. Semaphorin-3E produced by immature dendritic cells regulates activated natural killer

cells migration. *Frontiers in immunology* **2018**, *9*, 1005-1005.

131. Mahmood, S.; Nandagopal, S.; Sow, I.; Lin, F.; Kung, S.K.P. Microfluidic-based, live-cell analysis allows assessment of NK-cell migration in response to crosstalk with dendritic cells. *European Journal of Immunology* **2014**, *44*, 2737-2748.
132. Park, M.H.; Lee, J.S.; Yoon, J.H. High expression of CX3CL1 by tumor cells correlates with a good prognosis and increased tumor-infiltrating CD8+ T cells, natural killer cells, and dendritic cells in breast carcinoma. *Journal of Surgical Oncology* **2012**, *106*, 386-392.
133. Braun, S.E.; Chen, K.; Foster, R.G.; Kim, C.H.; Hromas, R.; Kaplan, M.H.; Broxmeyer, H.E.; Cornetta, K. The CC chemokine CKβ-11/MIP-3β/ELC/Exodus 3 mediates tumor rejection of murine breast cancer cells through NK cells. *The Journal of Immunology* **2000**, *164*, 4025.
134. Wu, J.; Hillier, C.; Komenda, P.; de Faria, R.L.; Santos, S.; Levin, D.; Zhang, M.; Lin, F. An all-on-chip method for testing neutrophil chemotaxis induced by fMLP and COPD patient's sputum. *Technology* **2016**, *4*, 104-109.
135. Pulaski, B.A.; Ostrand-Rosenberg, S. Mouse 4T1 breast tumor model. *Current Protocols in Immunology* **2000**, *39*, 20.22.21-20.22.16.
136. Reif, K.; Ekland, E.H.; Ohl, L.; Nakano, H.; Lipp, M.; Forster, R.; Cyster, J.G. Balanced responsiveness to chemoattractants from adjacent zones determines B-cell position. *Nature* **2002**, *416*, 94-99.
137. Otero, C.; Groettrup, M.; Legler, D.F. Opposite fate of endocytosed CCR7 and its ligands: Recycling versus degradation. *The Journal of Immunology* **2006**, *177*, 2314-2323.
138. Forster, R.; Davalos-Misslitz, A.C.; Rot, A. CCR7 and its ligands: Balancing immunity and tolerance. *Nature reviews. Immunology* **2008**, *8*, 362-371.
139. Brinkman, C.; Peske, J.; Engelhard, V. Peripheral tissue homing receptor control of naïve, effector, and memory CD8 T cell localization in lymphoid and non-lymphoid tissues. *Frontiers in immunology* **2013**, *4*, 241.
140. Vičić, M.; Peternel, S.; Simonić, E.; Sotošek-Tokmadžić, V.; Massari, D.; Brajac, I.; Kaštelan, M.; Prpić-Massari, L. Cytotoxic T lymphocytes as a potential brake of keratinocyte proliferation in psoriasis. *Medical Hypotheses* **2015**, *87*, 66-68.

141. Shams, K.; Wilson, G.J.; Singh, M.; van den Bogaard, E.H.; Le Brocq, M.L.; Holmes, S.; Schalkwijk, J.; Burden, A.D.; McKimmie, C.S.; Graham, G.J. Spread of psoriasiform inflammation to remote tissues is restricted by the atypical chemokine receptor ACKR2. *The Journal of Investigative Dermatology* **2017**, *137*, 85-94.

142. Jang, M.; Kim, H.; Kim, Y.; Choi, J.; Jeon, J.; Hwang, Y.; Kang, J.S.; Lee, W.J. The crucial role of IL-22 and its receptor in thymus and activation regulated chemokine production and T-cell migration by house dust mite extract. *Experimental dermatology* **2016**, *25*, 598-603.

143. Dai, Z.; Xing, L.; Cerise, J.; Wang, E.H.C.; Jabbari, A.; de Jong, A.; Petukhova, L.; Christiano, A.M.; Clynes, R. CXCR3 blockade inhibits T cell migration into the skin and prevents development of alopecia areata. *The Journal of Immunology* **2016**, *197*, 1089-1099.

144. Li, S.; Zhu, G.; Yang, Y.; Jian, Z.; Guo, S.; Dai, W.; Shi, Q.; Ge, R.; Ma, J.; Liu, L., *et al.* Oxidative stress drives $CD8^+$ T-cell skin trafficking in patients with vitiligo through CXCL16 upregulation by activating the unfolded protein response in keratinocytes. *Journal of Allergy and Clinical Immunology* **2017**, *140*, 177-189.

145. Ventrelli, L.; Marsilio Strambini, L.; Barillaro, G. Microneedles for transdermal biosensing: Current picture and future direction. *Advanced Healthcare Materials* **2015**, *4*, 2606-2640.

146. Nicol, N.H. Anatomy and physiology of the skin. *Dermatology nursing* **2005**, *17*, 62.

147. Kolarsick, P.A.J.; Kolarsick, M.A.; Goodwin, C. Anatomy and physiology of the skin. *Journal of the Dermatology Nurses' Association* **2011**, *3*, 203-213.

148. Reijnders, C.M.A.; van Lier, A.; Roffel, S.; Kramer, D.; Scheper, R.J.; Gibbs, S. Development of a full-thickness human skin equivalent in vitro model derived from tert-immortalized keratinocytes and fibroblasts. *Tissue engineering. Part A* **2015**, *21*, 2448-2459.

149. Getschman, A.E.; Imai, Y.; Larsen, O.; Peterson, F.C.; Wu, X.; Rosenkilde, M.M.; Hwang, S.T.; Volkman, B.F. Protein engineering of the chemokine CCL20 prevents psoriasiform dermatitis in an IL-23-dependent murine model. *Proc Natl Acad Sci U S A* **2017**, *114*, 12460-12465.

150. del Rey, M.J.; Izquierdo, E.; Caja, S.; Usategui, A.; Santiago, B.; Galindo, M.; Pablos, J.L. Human inflammatory synovial fibroblasts induce enhanced myeloid cell recruitment and angiogenesis through a hypoxia-inducible transcription factor 1α/vascular endothelial growth factor-mediated pathway in immunodeficient mice. *Arthritis & Rheumatism* **2009**, *60*, 2926-2934.
151. Fedyk, E.R.; Jones, D.; Critchley, H.O.D.; Phipps, R.P.; Blieden, T.M.; Springer, T.A. Expression of stromal-derived factor-1 is decreased by IL-1 and TNF and in dermal wound healing. *The Journal of Immunology* **2001**, *166*, 5749.
152. Zgraggen, S.; Huggenberger, R.; Kerl, K.; Detmar, M. An important role of the SDF-1/CXCR4 axis in chronic skin inflammation. *PloS one* **2014**, *9*, e93665.
153. Aoki, M.; Aoki, H.; Ramanathan, R.; Hait, N.C.; Takabe, K. Sphingosine-1-phosphate signaling in immune cells and inflammation: Roles and therapeutic potential. *Mediators of Inflammation* **2016**, *2016*, 8606878.
154. Chang, S.Y.; Weber, E.J.; Ness, K.P.V.; Eaton, D.L.; Kelly, E.J. Liver and kidney on chips: Microphysiological models to understand transporter function. *Clinical Pharmacology & Therapeutics* **2016**, *100*, 464-478.
155. Ware, B.R.; Khetani, S.R. Engineered liver platforms for different phases of drug development. *Trends in Biotechnology* **2016**, *35*, 172-183.
156. Nieskens, T.T.G.; Wilmer, M.J. Kidney-on-a-chip technology for renal proximal tubule tissue reconstruction. *European Journal of Pharmacology* **2016**, *790*, 46-56.
157. Visone, R.; Gilardi, M.; Marsano, A.; Rasponi, M.; Bersini, S.; Moretti, M. Cardiac meets skeletal: What's new in microfluidic models for muscle tissue engineering. *Molecules* **2016**, *21*, 1128.
158. Huang, C.P.; Lu, J.; Seon, H.; Lee, A.P.; Flanagan, L.A.; Kim, H.-Y.; Putnam, A.J.; Jeon, N.L. Engineering microscale cellular niches for three-dimensional multicellular co-cultures. *Lab on a chip* **2009**, *9*, 1740-1748.
159. Del Amo, C.; Borau, C.; Movilla, N.; Asin, J.; Garcia-Aznar, J.M. Quantifying 3D chemotaxis in microfluidic-based chips with step gradients of collagen hydrogel concentrations. *Integrative Biology* **2017**, *9*, 339-349.
160. Wu, X.; Newbold, M.A.; Haynes, C.L. Recapitulation of in vivo-like neutrophil

transendothelial migration using a microfluidic platform. *Analyst* **2015**, *140*, 5055-5064.

161. Chopra, K.; Calva, D.; Sosin, M.; Tadisina, K.K.; Banda, A.; De La Cruz, C.; Chaudhry, M.R.; Legesse, T.; Drachenberg, C.B.; Manson, P.N., *et al.* A comprehensive examination of topographic thickness of skin in the human face. *Aesthetic surgery journal* **2015**, *35*, 1007-1013.
162. Usami, S.; Okazaki, M.; Nitta, T.; Uemura, N.; Homma, T.; Akita, K. Histological investigation of common insensate flaps obtained from the hand and forearm regions for use in fingertip reconstruction. *Journal of plastic surgery and hand surgery* **2017**, *51*, 182-186.
163. Ren, X.; Wu, J.; Levin, D.; Santos, S.; de Faria, R.L.; Zhang, M.; Lin, F. Sputum from chronic obstructive pulmonary disease patients inhibits T cell migration in a microfluidic device. *Annals of the New York Academy of Sciences* **2019**, *1445*, 52-61.
164. Ren, X.; Alamri, A.; Hipolito, J.; Lin, F.; Kung, S.K.P. Applications of microfluidic devices in advancing NK-cell migration studies. In *Methods in enzymology*, Academic Press: 2019; Vol. 631, pp 357-370.
165. Wu, J.; Kumar-Kanojia, A.; Hombach-Klonisch, S.; Klonisch, T.; Lin, F. A radial microfluidic platform for higher throughput chemotaxis studies with individual gradient control. *Lab on a Chip* **2018**, *18*, 3855-3864.
166. Blum, K.M.; Novak, T.; Watkins, L.; Neu, C.P.; Wallace, J.M.; Bart, Z.R.; Voytik-Harbin, S.L. Acellular and cellular high-density, collagen-fibril constructs with suprafibrillar organization. *Biomaterials science* **2016**, *4*, 711-723.
167. Keating, M.; Kurup, A.; Alvarez-Elizondo, M.; Levine, A.J.; Botvinick, E. Spatial distributions of pericellular stiffness in natural extracellular matrices are dependent on cell-mediated proteolysis and contractility. *Acta Biomaterialia* **2017**, *57*, 304-312.
168. Griffith, J.W.; Luster, A.D. Targeting cells in motion: Migrating toward improved therapies. *European Journal of Immunology* **2013**, *43*, 1430-1435.
169. Lafouresse, F.; Groom, J.R. A task force against local inflammation and cancer: Lymphocyte trafficking to and within the skin. *Frontiers in immunology* **2018**, *9*, 2454.
170. Mondadori, C.; Crippa, M.; Moretti, M.; Candrian, C.; Lopa, S.; Arrigoni, C. Advanced microfluidic models of cancer and immune cell extravasation: A systematic review of the

literature. *Frontiers in Bioengineering and Biotechnology* **2020**, *8*, 907.

171. Karmakar, S.; Reilly, K.M. The role of the immune system in neurofibromatosis type 1-associated nervous system tumors. *CNS oncology* **2017**, *6*, 45-60.
172. Wang, S.; Liechty, B.; Patel, S.; Weber, J.S.; Hollmann, T.J.; Snuderl, M.; Karajannis, M.A. Programmed death ligand 1 expression and tumor infiltrating lymphocytes in neurofibromatosis type 1 and 2 associated tumors. *Journal of Neuro-Oncology* **2018**, *138*, 183-190.
173. Wang, X.; Huang, S.; Zhang, Y.; Zhu, L.; Wu, X. The application and mechanism of PD pathway blockade for cancer therapy. *Postgraduate Medical Journal* **2018**, *94*, 53.
174. Pardoll, D.M. The blockade of immune checkpoints in cancer immunotherapy. *Nature Reviews Cancer* **2012**, *12*, 252.
175. Zou, W.; Wolchok, J.D.; Chen, L. PD-L1 (B7-H1) and PD-1 pathway blockade for cancer therapy: Mechanisms, response biomarkers, and combinations. *Science Translational Medicine* **2016**, *8*, 328rv324.
176. Bang, S.; Jeong, S.; Choi, N.; Kim, H.N. Brain-on-a-chip: A history of development and future perspective. *Biomicrofluidics* **2019**, *13*, 051301.
177. Neufurth, M.; Wang, X.; Wang, S.; Steffen, R.; Ackermann, M.; Haep, N.D.; Schröder, H.C.; Müller, W.E.G. 3D printing of hybrid biomaterials for bone tissue engineering: Calcium-polyphosphate microparticles encapsulated by polycaprolactone. *Acta Biomaterialia* **2017**, *64*, 377-388.
178. Hixon, K.R.; Melvin, A.M.; Lin, A.Y.; Hall, A.F.; Sell, S.A. Cryogel scaffolds from patient-specific 3D-printed molds for personalized tissue-engineered bone regeneration in pediatric cleft-craniofacial defects. *Journal of Biomaterials Applications* **2017**, *32*, 598-611.
179. Gregor, A.; Filová, E.; Novák, M.; Kronek, J.; Chlup, H.; Buzgo, M.; Blahnová, V.; Lukášová, V.; Bartoš, M.; Nečas, A. Designing of PLA scaffolds for bone tissue replacement fabricated by ordinary commercial 3D printer. *Journal of Biological Engineering* **2017**, *11*, 31.
180. Domansky, K.; Leslie, D.C.; McKinney, J.; Fraser, J.P.; Sliz, J.D.; Hamkins-Indik, T.; Hamilton, G.A.; Bahinski, A.; Ingber, D.E. Clear castable polyurethane elastomer for

fabrication of microfluidic devices. *Lab on a Chip* **2013**, *13*, 3956-3964.

Appendix

Figure A. 1. Human T cell migration to S1P gradients in the 2D radial microfluidic device.

The activated human peripheral blood T cells (ahPBTs) were prepared as described in the manuscript, and T cells were re-suspended in RPMI-1640 medium (serum/antibiotics-free) when loading into a previously published radial microfluidic device [165]. Seven different experimental groups (i.e., Medium: RPMI-1640 medium and S1P: Sphingosine-1-phosphate (S1P) prepared in the same medium at final concentrations of 100 nM, 200 nM, 300 nM, 500 nM, 750 nM, 1000 nM) were performed in parallel on the same radial microfluidic device, and each experiment was independently replicated at least three times using separate devices. **(A)** Representative images of T cell migration in the medium and the different S1P groups in the radial microfluidic device at 0 h and 0.5 h, respectively (scale bar: 100 μm). The black arrow besides the images indicates the gradient direction of S1P in all the groups except for the medium control. The red circles in the images label all the migrated human T cells in the different groups. **(B)** The displacement analysis of T cells in the different experimental groups at 0.5h from Figure A. The colored box chart shows the total displacement of each cell in the corresponding experimental groups in Figure A. The interpretation of box chart is the same as previously described. The data in different groups were compared using the two sample Student's t-test available in OriginPro, significant difference compared to the "Medium" group was indicated using $*p < 0.05$, $**p < 0.01$, and $***p < 0.001$.

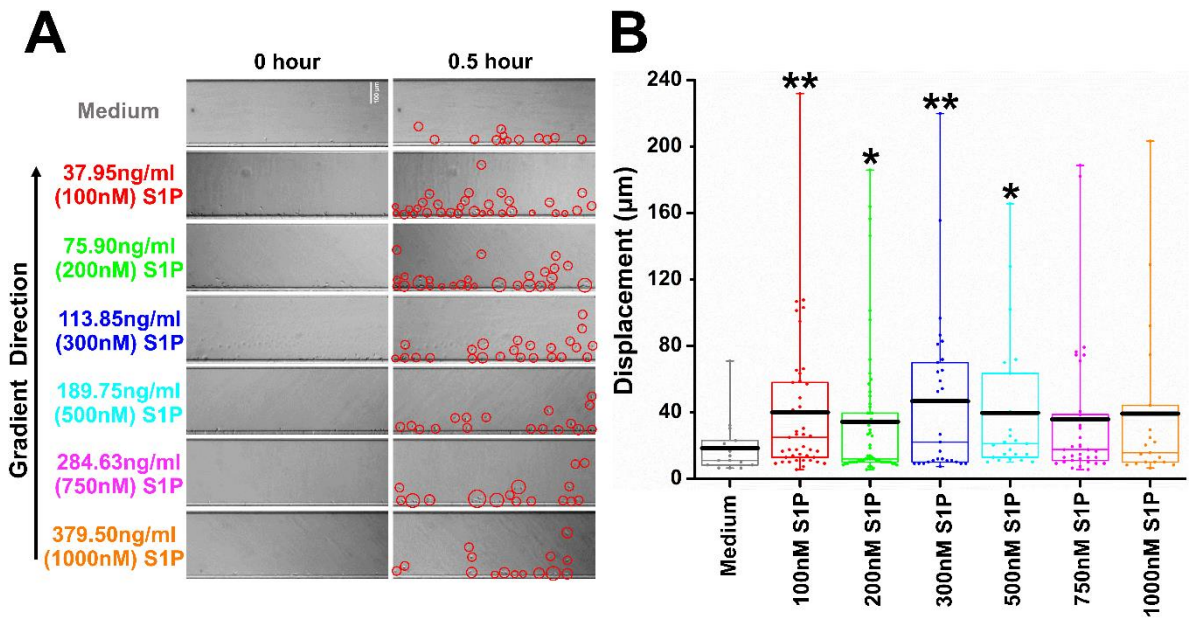
A
0 hour
0.5 hour
Medium
37.95ng/ml (100nM) S1P
75.90ng/ml (200nM) S1P
113.85ng/ml (300nM) S1P
189.75ng/ml (500nM) S1P
284.63ng/ml (750nM) S1P
379.50ng/ml (1000nM) S1P
Gradient Direction
B
Displacement (μm)
240
200
160
120
80
40
0
**
*
**
*
Medium
100nM S1P
200nM S1P
300nM S1P
500nM S1P
750nM S1P
1000nM S1P

Figure A. 2. T cell migration to CXCL12, CCL20WT and CCL20LD gradients in the D^3-Chip.

The ahPBTs were prepared as described in the manuscript, and T cells were re-suspended in complete RPMI-1640 medium (RPMI-1640 with 1% penicillin-streptomycin and 10% FBS) when loading into a previously designed D^3-Chip [163,164]. Eight different experimental groups were tested and compared: RPMI-1640 medium (serum/antibiotics-free); C-X-C motif chemokine ligand 12 (CXCL12) in the same medium at 100 ng/mL; C-C motif ligand 20 wild-type (CCL20WT) in the same medium at 1 μg/mL, 10 μg/mL, and 100 μg/mL; CCL20 locked dimer (CCL20LD) prepared in the same medium at 1 μg/mL, 10 μg/mL, and 100 μg/mL. Each experiment was independently replicated at least three times using separate devices. **(A)** Representative images of T cell migration in the different groups in the D^3-Chip at 0 h, 0.5 h and 1 h, respectively (scale bar: 100 μm). The black arrow besides the images indicates the gradient direction in all the groups, with the exception of the medium control. **(B)** The displacement analysis of T cells in the different experimental groups at 1h from Figure A is shown. The colored box chart shows the total displacement of each cell in the corresponding experimental groups in Figure A. The interpretation of box chart is the same as previously described. The data in different groups were compared using the two sample Student's t-test available in OriginPro. Significant difference compared to the "Medium" group was indicated using $^{*}p < 0.05$, $^{**}p < 0.01$, and $^{***}p < 0.001$; Significant difference compared to the "100 ng/mL CXCL12" group was indicated using $^{\#}p < 0.05$, $^{\#\#}p < 0.01$, $^{\#\#\#}p < 0.001$; Significant difference compared to the "1 μg/mL CCL20WT" group was indicated using $^{\wedge}p < 0.05$, $^{\wedge\wedge}p < 0.01$, $^{\wedge\wedge\wedge}p < 0.001$; Significant difference compared to the "1 μg/mL CCL20LD" group was indicated using $^{\&}p < 0.05$, $^{\&\&}p < 0.01$, $^{\&\&\&}p < 0.001$.

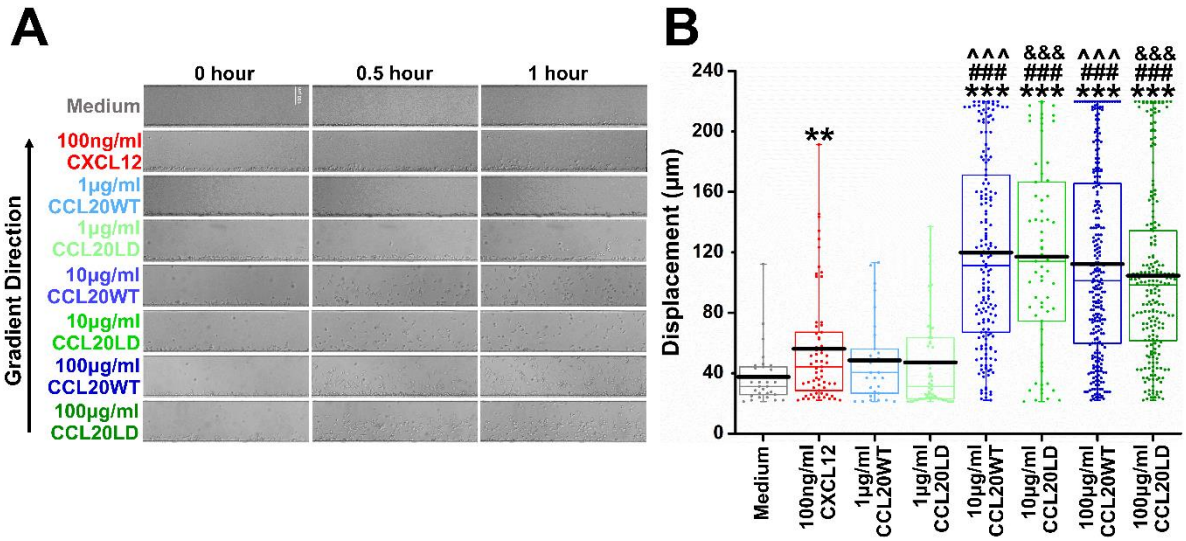
A
0 hour
0.5 hour
1 hour
Medium
100ng/ml CXCL12
1μg/ml CCL20WT
1μg/ml CCL20LD
10μg/ml CCL20WT
10μg/ml CCL20LD
100μg/ml CCL20WT
100μg/ml CCL20LD
Gradient Direction
B
Displacement (μm)
240
200
160
120
80
40
0
**
^^^
###
***
&&&
###
***
^^^
###
***
&&&
###
***
Medium
100ng/ml CXCL12
1μg/ml CCL20WT
1μg/ml CCL20LD
10μg/ml CCL20WT
10μg/ml CCL20LD
100μg/ml CCL20WT
100μg/ml CCL20LD

Figure A. 3. The CCR6 expression of ahPBTs by flow cytometry and on-chip staining in the D^3-Chip and the SoC model.

For flow cytometry analysis, ahPBTs were collected and incubated with FITC anti-human CD196 (CCR6) antibody (BioLegend, Catalog# G034E3) at the final concentration of 2 µg/ml in PBS (1×) for 30 minutes at room temperature, then rinsed with PBS (1×) two times. Cells with or without antibody incubation were re-suspended in PBS and divided into different tubes for analysis in a flow cytometer (BD FACSCalibur, ON, Canada). For on-chip staining, chemical solutions were removed from the chip after cell migration experiments and rinsed once with PBS. Cells were fixed in 4% of paraformaldehyde (PFA) for 20 minutes at room temperature followed by another rinse with PBS. The D^3-Chip was incubated with the CCR6 antibody at the final concentration of 2 µg/ml in PBS for 30 minutes in an incubator (37 °C; 5% CO_2), while the micropillar device was incubated with the CCR6 antibody at the final concentration of 10 µg/ml in PBS for 1 hour in an incubator (37 °C; 5% CO_2). The devices were then rinsed once with PBS after incubation before taking images with the fluorescence microscope (Nikon Ti-U). **(A)** Representative data of CCR6 expression of ahPBTs in the flow cytometry analysis extracted from FlowJo software (FlowJo LLC., Ashland, Oregon, USA). **(B)** Representative images to show the CCR6 expression of ahPBTs at the end of 1h migration experiment in the D^3-Chip. **(C)** Representative images to show the CCR6 expression of ahPBTs at the end of 2h migration experiment in the micropillar device. DIC image: Differential interference contrast image; FITC image: Fluorescein isothiocyanate image; Scare bar: 100 µm.